Computational Fluid Dynamics (CFD) modelling of rollover and application to Liquefied Natural Gas storage

Antoine Hubert

A thesis presented for the degree of

Doctor of Philosophy

Faculty of Science, Engineering and Computing

Kingston University

June 1, 2019

A Jihane et à mes parents,

Declaration

I hereby declare that except where specific reference is made to the work of others, the contents of this dissertation are original and have not been submitted in whole or in part for consideration for any other degree or qualification in this, or any other university. This dissertation is my own work and contains nothing which is the outcome of work done in collaboration with others, except as specified in the text and Acknowledgements. This dissertation contains fewer than 40,000 words including appendices, bibliography, footnotes, tables and equations and has fewer than 150 figures

Antoine Hubert

Acknowledgements

First, I would like to thank Dr. Siaka Dembele, Prof Jennifer Wen and Dr. Petr Denissenko for giving me the chance to take part in the SafeLNG project as well as for their guidance all along my PhD.

I am also very thankful to the European Commission for funding the thesis through the Marie Skłodowska-Curie Actions. The program gave me the opportunity to work on such an interesting project while learning new things every day.

Then, I am extremely grateful to Kostas, Marco, Reza and Javier for the assistance including during these long evenings on the campus as well as for making the PhD room such a pleasant environment.

Besides, I would like to express my gratitude to Edouard, Mateusz and Alexis for their dedicated time, helpful discussions and advice.

Before finishing, I would like to thank my friends and family, especially my parents, Isabelle and Loïc, for their continuous support as well as Typhaine and Nicolas for their great help during this PhD.

Last but not least, a special thanks goes to Jihane for her unconditional support and her precious advice through all these years.

Abstract

The interest to study and predict Liquefied Natural Gas (LNG) rollovers dates back to the 60^s following La Spezia incident, which highlighted the need to take extra care when storing LNG with different densities together. However, LNG rollovers - which are complex physical phenomena during which a stratified LNG is suddenly and rapidly mixed while releasing large amounts of vapour - can be hazardous. In order to limit any resulting overpressure and subsequent releases of vapour into the atmosphere, rollovers have to be better understood.

Currently, 0D lumped-parameter models are used in the LNG industry, but by restricting rollovers as the consequence of the average density equalisation of two adjacent layers, it leaves little room to tank design and filling procedure improvements.

The novelty of this work is the development of an LNG rollover predictive code, rolloverFoam, based on Computational Fluid Dynamics and capable of providing spatial representations — in 2D and 3D — of the phenomenon while predicting rollover occurences reliably. RolloverFoam, which is based on the Navier-Stokes equations, integrates the effects of buoyancy via the Boussinesq approximation. Besides, unlike previous studies, the effects of turbulence are also accounted for in the code, and among the existing RANS methods, $k - \epsilon$ models incorporating the influence of buoyancy were used.

Given the lack of data publicly available for LNG rollovers, rolloverFoam was at first applied to simulate small-scale experiments with mixtures of Freon. Later, it was applied to a medium-scale LNG rollover experiment and the well-

known La Spezia incident. The numerical results, obtained both for Freon and LNG, have shown very encouraging agreements with experimental data while providing some insights into the physics underpinning the phenomenon thanks to 2D and 3D spatial representations. Besides, an advantage of rolloverFoam is its adaptability to more complex geometries compared to traditional lumped-parameter models currently used in the LNG industry. Hence, the method was finally applied to simulate a stationary medium-scale FLNG Moss type tank.

Keywords : LNG, Rollover, CFD, Double-diffusion, Buoyancy, Safety

Contents

List of Figures

List of Tables

Nomenclature

The following list describes the symbols, chemical formulas and acronyms that will be later used within the body of this thesis. In "Other symbols", a is either a given scalar, a vector or a tensor and is only used to illustrate the symbols.

Roman symbols

$[A]$	matrix with the coefficients obtained after discretising a transport scalar equation
$\boldsymbol{a}$	general vector
a_N	coefficients affected to the control volume after discretisation
a_P	coefficients affected to the neighbouring cells after discretisation
C	mass concentration [kg·m^{-3}]
C_{m_0}, C_m	constants in Hashemi Wesson relation [-]
Co	Courant number [-]
c_p	specific heat capacity [J·kg^{-1}·K^{-1}]
$c_{3\epsilon}$	term in the $k-\epsilon$ model
c_μ	constant in the $k-\epsilon$ model
c_θ, c_ϕ	constants used for the Generalized Gradient Diffusion Hypothesis

D	source term in the Launder-Sharma $k-\epsilon$ model
D	diameter [m]
D	solutal diffusivity [$m^2 \cdot s^{-1}$]
D_{ab}	solutal diffusivity of a given solute a in given solute b [$m^2 \cdot s^{-1}$]
d	distance between the cell centre and the surface f [m]
$\boldsymbol{dS}$	face area vector associated to ds [m^2]
ds	surface element [m^2]
E	wall roughness parameter
E	source term in the Launder-Sharma $k-\epsilon$ model
F	velocity flux
f_2, f_μ	damping function in the Launder-Sharma $k-\epsilon$ model
Gr^*	modified Grashof number, $Gr^* = \frac{g\beta_T q L^4}{\nu^2}$ [-]
$\boldsymbol{g}$	gravity vector [$m \cdot s^{-2}$]
g	magnitude of the gravity vector [$m \cdot s^{-2}$]
H	liquid height [m]
$H(U)$	element involved during the discretisation of the momentum equation
h	layer height [m] or heat transfer coefficient [$W \cdot m^{-2} \cdot K^{-1}$]
$\boldsymbol{j}$	diffusion flux [$kg \cdot m^{-2} \cdot s^{-1}$]
K_S	effective turbulent transfer coefficient for salt [$m \cdot s^{-1}$]
k_S	molecular diffusivity of salt [$m \cdot s^{-1}$]

K_T	effective turbulent transfer coefficient for temperature [$\mathrm{m{\cdot}s^{-1}}$]
k_T	molecular diffusivity of heat [$\mathrm{W{\cdot}m^{-1}{\cdot}K^{-1}}$]
$\boldsymbol{k}$	vector in the non-orthogonality treatment
k	turbulent kinetic energy [$\mathrm{m^2{\cdot}s^{-2}}$]
k_1, k_2	correction factors used in the revised Klosek-McKinley method [kmol]
L	latent heat [$\mathrm{J{\cdot}kg^{-1}}$] or characteristic length scale [m]
M	molecular weight [$\mathrm{g{\cdot}mol^{-1}}$]
m	mass [kg]
$\dot{m}$	evaporation rate [$\mathrm{kg{\cdot}m^{-2}{\cdot}s^{-1}}$]
$\boldsymbol{n}$	normal vector to a given surface
n	total number of layers or total number of species
Nu	Nusselt number $Nu = \frac{hL}{\lambda}$ [-]
P_b	source term accounting for the effects of buoyancy on the turbulence
P_b	heating power transmitted to the liquid through the bottom wall [$\mathrm{W{\cdot}m^{-2}}$]
P_k	source term accounting for the generation of turbulent kinetic energy due to mean velocity gradient
P_s	heating power transmitted to the liquid through the side wall [$\mathrm{W{\cdot}m^{-2}}$]
Pr	Prandtl number, $Pr = \frac{\nu}{\alpha}$ [-]

Pr_t	turbulent Prandtl number [-]
p	pressure [kg·m^{-1}·s^{-2}]
p_m	modified pressure [m^2·s^{-2}]
q	heat flux [W·m^{-2}]
q^H	heat transfer coefficient [kg·s^{-3}·K^{-1} or W·m^{-2}·K^{-1}]
q^M	mass transfer coefficient [kg·m^{-2}·s^{-1}]
q_b	heat flux from the bottom wall heating the liquid [W·m^{-2}]
q_{bl}	heat flux from the bottom wall heating the liquid [W·m^{-2}]
q_s	heat flux from the side wall heating the liquid [W·m^{-2}]
q_{sl}	heat flux from the side wall heating the liquid [W·m^{-2}]
q_{sv}	heat flux from the side wall heating the vapour [W·m^{-2}]
q_{tv}	heat flux from the top wall heating the vapour [W·m^{-2}]
q_{vl}	heat flux from the vapour heating the liquid [W·m^{-2}]
$[R]$	source vector after discretising a transport scalar equation
R	stability parameter $R = \frac{\beta_C \Delta C}{\beta_T \Delta T}$[-] or radius [m]
R_P	source term after discretisation
r	radial coordinate [m]
Ra	Rayleigh number, $Ra = \frac{g\beta_T \Delta T L^3}{\nu\alpha}$ [-]
Ra^*	modified Rayleigh number, $Ra^* = \frac{g\beta_T q L^4}{\nu\alpha\lambda}$ [-]
Ra_C	solutal Rayleigh number, $Ra_C = \frac{g\beta_C \Delta C}{D\nu}$ [-]
Re	Reynolds number, $Re = \frac{UL}{\nu}$

Re_t	turbulent Reynolds number, $Re_t = \frac{k^2}{\nu\epsilon}$
$\boldsymbol{S_M}$	momentum source term [kg·m^{-1}·s^{-1}]
S_P	linear part of the source term S_ψ
S_U	non-linear part of the source term S_ψ
S_i	energy source term [kg·m^{-1}·s^{-3}]
S_f	face area vector [m^2]
S_ψ	source term
Sc	Schmidt number $Sc = \frac{\nu}{D}$ [-]
Sc_t	turbulent Schmidt number [-]
T	temperature [K]
$c_{1\epsilon}$	constant in the $k-\epsilon$ model $c_{1\epsilon} = 1.44$
t	time [s]
$\boldsymbol{U}$	mean velocity vector following Reynolds decomposition [m·s^{-1}]
U	velocity component orthogonal to the gravity vector [m·s^{-1}]
$\boldsymbol{u}$	velocity vector [m·s^{-1}]
$\boldsymbol{u'}$	fluctuating velocity vector following Reynolds decomposition [m·s^{-1}]
u_τ	friction velocity [m·s^{-1}]
u^+	dimensionless velocity such as $u^+ = \frac{u}{u_\tau}$ [-]
V	volume [m^3]

V	velocity component in the same direction as the gravity vector [m·s^{-1}]
V_a	molar volume of the solute a at normal boiling point [cm^3·g^{-1}·mol^{-1}]
$c_{2\epsilon}$	constant in the $k-\epsilon$ model $c_{2\epsilon} = 1.92$
V_P	volume of the control volume [m^3]
W	width [m]
x	molar fraction [-]
y	distance to the wall [m]
y^+	dimensionless distance to the wall [-]
z	altitude [m]

Greek symbols

α	thermal diffusivity [m^2·s^{-1}]
β_T	thermal expansion coefficient [K^{-1}]
β_C	solutal expansion coefficient [m^3·kg^{-1}]
Γ	effective diffusion coefficient of the general scale ψ [m^2·s^{-1}]
$\boldsymbol{\Delta}$	vector in the non-orthogonality treatment
ΔT	temperature difference [K]
Δt	time step [s]
Δx	molar fraction difference [-]
$\Delta x, \Delta y, \Delta z$	grid spacing in the $\boldsymbol{x}$,$\boldsymbol{y}$,$\boldsymbol{z}$ directions [m]
$\Delta\rho$	density difference [kg·m^{-3}]

δ_f	ratio of the distance face-cell centre and the distance cell centre-neighbouring cell centre [-]
δ_{ij}	Kronecker symbol equal to 1 if i=j otherwise 0
ϵ	turbulent dissipation rate [$m^2 \cdot s^{-3}$]
η	aspect ratio, $\eta = \frac{R}{H}$ for a cylinder or $\eta = \frac{W}{H}$ for a rectangular prism [-]
κ	Von Karman constant
λ	thermal conductivity [$W \cdot m^{-1} \cdot K^{-1}$]
μ	dynamic viscosity [$kg \cdot m^{-1} \cdot s^{-1}$]
ν	kinematic viscosity [$m^2 \cdot s^-1$]
ν_t	turbulent kinetic viscosity [$m^2 \cdot s^{-1}$]
ρ	density [$kg \cdot m^{-3}$]
ρ_k	ratio of the density and the reference density, $\rho_k = \frac{\rho}{\rho_0}$
σ_k	constant in the $k - \epsilon$ model $\sigma_k = 1.00$
σ_ϵ	constant in the $k - \epsilon$ model $\sigma_\epsilon = 1.30$
σ_μ	constant in the $k - \epsilon$ model $\sigma_\mu = 0.09$
$\sigma_{\rho k}$	constant in the buoyant $k - \epsilon$ model
$\bar{\bar{\boldsymbol{\tau}}}$	deviatoric stress tensor [$kg \cdot s^{-2} \cdot m^{-1}$]
$\bar{\bar{\boldsymbol{\tau}}}^{\boldsymbol{t}}$	stress tensor accounting for the effect of turbulence [$kg \cdot s^{-2} \cdot m^{-1}$]
τ_{wall}	wall shear stress [$kg \cdot s^{-2} \cdot m^{-1}$]
Φ	mean scalar quantity following Reynolds decomposition

ϕ	general scalar
ϕ_b	association parameter in Wilke and Chang relation
ϕ'	fluctuating scalar quantity following Reynolds decomposition
χ	dissipation function accounting for the effect of the viscous forces
ψ	general scalar
$[\psi]$	ψ scalar field written as a vector
ω	mass fraction

Subscripts

0	reference
B	bottom wall
bot	bottom layer
$bulk$	bulk
eff	effective
ev	evaporative
f	face interpolated
i	i^{th} layer
i	i^{th} coordinate
l	lower layer
m	modified
N	cell centre of the neighbouring cell or group constituted of all neighbouring cell centres of the control volume

P	cell centre of the control volume
$R11$	Freon 11
$R113$	Freon 113
S	side wall
sat	saturation
$surface$	free surface
t	turbulent
t	top layer
u	upper layer
$wall$	wall
x,y,z	respectively, component in the $\boldsymbol{x}$, $\boldsymbol{y}$, $\boldsymbol{z}$ directions

Supercripts

$'$	fluctuating quantity following Reynolds decomposition
0	previous time step
*,**,***	correspond to the predictor-corrector level
n	new time step

Other symbols

$\bar{a}$	mean quantity following Reynolds decomposition
$\tilde{a}$	dimensionless quantity
$\|\|\boldsymbol{a}\|\|$	vector magnitude
$\nabla.$	divergence of a vector or tensor

∇	gradient of a scalar, vector or tensor
Δ	laplacian of a scalar, vector or tensor

Chemical formulas

CH_4	Methane
C_2H_6	Ethane
C_3H_8	Propane
C_4H_{10}	Butane
C_5H_{12}	Pentane
H_2O	Water
N_2	Nitrogen

Acronyms/Abbreviations

BOR	boil-off rate
bi-CG	biconjugate gradient method
CD	Central Differencing
CG	conjugate gradient method
CPU	Computational Power Unit
DNS	Direct Numerical Simulation
FSRU	Floating Storage Regasification Units
GGDH	Generalized Gradient Diffusion Hypothesis
GIIGNL	International Group of Liquefied Natural Gas Importers
HSM	Heestand-Shipman-Meader model

LES	Large Eddy Simulation
LTD	level, temperature and density
LU	lower-upper factorisation
LUD	Linear Upwind Differencing
PISO	Pressure-Implicit with Splitting of Operators
RANS	Reynolds Averaged Navier-Stokes
SGDH	Standard Gradient Diffusion Hypothesis
SIGTTO	Society of International Gas Tanker and Terminal Operators
SIMPLE	Semi-Implicit Method for Pressure Linked Equations
UD	Upwind Differencing
VOF	Volume of Fluid
CFD	Computational Fluid Dynamics
FLNG	Floating Liquefied Natural Gas
LNG	Liquefied Natural Gas
NG	Natural Gas

Chapter 1

Introduction

1.1 Background

Although Natural Gas was already used in China in the 5^{th} centuries B.C. to separate salt from sea water, it is only in 1785 that Britain paved the way to gas commercialisation for house and street lightning with Natural Gas obtained from coal. Later, the industrial revolution and scientific progress have contributed to its widespread use.

Nowadays, world energy demand is booming. It should even increase by 30% by 2040 according to the International Energy Agency [1]. As for Natural Gas which, at the moment, represents 21% of global primary energy demand, it is expected to play a major role in the transition to cleaner energy while reaching around 24% by 2040 [1]. With this growing demand in Natural Gas, it is a whole industry which has to adapt itself by developing its current storage and transport facilities in order to satisfy its expectations.

A promising alternative to using gas pipelines, especially for international trades and storage purposes, is to liquefy Natural Gas to below -162°C and at the atmospheric pressure. The resulting Liquefied Natural Gas (LNG) can then be stored in a volume 600 times smaller which is particularly advantadgeous for its storage in LNG receiving terminals and its transportation all around the world

via Floating LNG (FLNG) carriers. The LNG industry is constantly expanding as a result of the global demand in LNG which is expected to increase by 45% by 2040 [2]. This rising global demand in LNG fosters the multiplication of production sites. As a result, this latter contributes to the diversification of LNG since the composition and properties of this multicomponent mixture vary from a production site to another. However, as far as LNG storage is concerned, it has been observed that after combining different sources or compositions of LNG in the same tank, stratification may be obtained and result in a hazardous scenario called "rollover".

During rollover, the strata are sudddenly mixed while releasing large amounts of LNG vapour which need to be vented out to prevent from any overpressure inside the tank that could jeopardise its structure and result in a catastrophic scenario. However, the release of vapours into the atmosphere is not without consequences. Indeed, LNG vapours are dangerous since they can explode in the presence of an ignition source but they are also harmful to the environment because they are composed of greenhouse gases, especially methane. Finally, these large releases are also a loss of income for the companies involved in the storing and transporting processes.

After combining several sources [3, 4, 5], it turns out that more than 70 rollovers have occurred over the last 60 years. Fortunately, only minor material damages were observed following the incidents. It remains that rollovers have to be carefully tackled given that its consequences can be damaging for the staff, the environment and the facilities.

1.2 Motivations

Rollovers and particularly La Spezia incident in 1971 [6] have arisen the interest of researchers. Several experimentalists have conducted small-scale rollover experiments using different types of mixture [7, 8]. However, despite their inter-

ests, these experiments could not, in particular, reproduce the effect of the large scales involved in a typical LNG tank which are usually more than 20 meters high. Also, some researchers have developed some numerical codes based on lumped-parameter models to simulate and predict the occurrence of rollovers [9, 10, 11]. Nonetheless, despite their acceptable accuracy, they do not take into account the fluid dynamics and cannot provide visualisation of the spatial behaviour of the fluid during the phenomenon. As a result, among the scientific community, it is still not clear which physical mechanisms are driving LNG rollovers. This lack of understanding is probably one of the reasons why rollovers are still occurring even after more than 50 years of research and why they still stimulate the curiosity of researchers.

Nonetheless, apart from the technical report written by the International Group of Liquefied Natural Gas Importers [12], only few studies dealing with rollovers have been published within the last ten years. Several factors detailed hereafter can explain these low figures. However, they do not reflect any lack of interest in rollovers from the LNG industry. On the contrary and as described in the following section, given the recent rise of Floating Storage Regasification Units (FSRU) as well as the growing trend of taking advantage of the stratification to reduce the evaporation rate during storage, the interest in LNG rollovers is increasing.

First, a difficulty which arises with LNG rollovers and which may be a reason of the low number of publications within the last ten years is the lack of a publicly available database reporting the past rollovers, and providind monitored data from the incidents. Among the 70 rollover incidents which have occurred, only La Spezia and Partington incidents are published in the literature with significant amount of technical data. A considerably more detailed database is needed to ensure the necessary grounds for future studies.

The low number of publications can also be explained by the fact that industrialists have adapted over the years the LNG facilities in order to deal with

potential risks of rollovers and are usually able to tackle the issue safely. To this aim, tanks have been equipped with sophisticated monitoring and mixing devices enabling operators to observe as well as to take measures to prevent or mitigate the consequences of rollovers. Although the physical mechanisms driving the rollovers are not clearly understood, the LNG industry knows from its experience how to deal with them efficiently. In addition, the predictive rollover models currently used within the LNG industry and which are based on lumped-parameter models, are extensions of the earlier models developed between 1960 and 1990 and few improvements have been made since then, hence the low number of recent publications.

In addition, as far as Computational Fluid Dynamics (CFD) simulations are concerned, their demanding computational needs as well as the simulation time used to be deterring especially for this type of application. However, the recent and drastic improvements in computational facilities put CFD simulations of LNG rollovers back on the agenda.

Moreover, the recent and rapid expansion of FSRU — which are floating LNG facilities — as well as the growing trend to intentionally use LNG stratification during storage have both been involved in making rollover a topical issue. Indeed, while the first FSRU dates back to 2007 and LNG rollovers are usually safely handled within onshore LNG facilities, more than 20 rollovers have been observed onboard FSRU [5] partly due to the lack of monitoring devices enabling operators to anticipate the incidents. Besides, taking advantage of the stratification to reduce the evaporation rate (and consequently the cost induced by the reliquefaction) while loading is becoming a more common practice [12, 13]. This practice if not handled carefully, can lead to rollovers.

As a result, the growing interest for rollovers motivates the research conducted within the frame of this thesis.

1.3 Aims and objectives

Several CFD codes have been implemented by previous researchers [14, 15, 16, 17] providing significant insights into the physics involved during the rollover phenomenon as well as into the numerical method. However, several aspects in these models were simplified, preventing them from providing predictive results and comparing their results quantitatively to experimental data. Indeed, these models were taking into account binary mixtures such as mixtures of Freon 11/Freon 113, salt water, ethanol and water and LNG was also reduced to a two component mixture. Besides, these models, which were developed in the 90s, were applied to simplified 2D or axisymmetric models given the limit in computational facilities. Turbulence was also neglected in these simulations although it was known to influence the flow significantly [14, 16].

Taking advantage of the development of computational facilities over the last few decades, the novelty of this PhD thesis is to implement a code based on CFD, rolloverFoam, capable of predicting reliably LNG rollover occurrence and the resulting boil-off rate. The 2D and 3D results will be validated with small-scale and medium-scale experimental data. Unlike previous models, the code, developed within the frame of this thesis, takes into account the effects of turbulence and considers LNG as a multicomponent mixture. Besides, this approach which, unlike traditional lumped-parameter models, simulates the spatial behaviour of the fluid, will provide some new insights into the mechanisms driving the rollover phenomenon.

However, the main difficulty is the lack of data in the available literature regarding real-scale LNG rollover incident. The two incidents which occurred in La Spezia in 1971 [6] and Partington in 1993 [18] were reported and published in the literature but need to be more detailed to be exploitable for CFD simulations. For the sake of simplicity, several researchers have conducted small-scale rollover experiments [8] which are well documented in the literature. These results will

be of interest for validation purposes.

The following objectives have been assigned to the research:

1. Develop a CFD code capable of modelling and predicting the rollover occurrence in binary mixtures
2. Validate the code with small-scale experiments from the literature conducted with mixtures of Freon 11 and Freon 113
3. Apply and validate the code with medium-scale and large-scale LNG rollover scenarios
4. Provide some new insights into the rollover phenomenon.

1.4 Structure

In Chapter 2, the rollover phenomenon is explained as well as its potential consequences and the methods employed in the industry to prevent its occurrences and damaging effects. Besides, this chapter also aims at giving the readers an overview of the experimental and numerical research that has been conducted in this field. The equations and numerical models, on which is based the solver rolloverFoam developed within the frame of this thesis, are then introduced in Chapter 3. Afterwards, Chapter 4 deals with the numerical method adopted in the code to solve the equations presented in the previous chapter. In Chapter 5, the code is at first used to model two cases from the literature [14]. Then, the code is applied to simulate several small-scale rollover experiments with Freon conducted by Nakano et al. [8]. Finally, the code is improved to model LNG and is applied to model a medium-scale rollover experiment, La Spezia incident and a fictive FLNG rollover incident. The thesis ends with a conclusion summarising the method and the results while giving some recommendations for future works.

Chapter 2

Literature review

2.1 Liquefied Natural Gas

Liquefied Natural Gas (LNG) is a cryogenic liquid made from Natural Gas which is cooled down and liquefied below -162°C at atmospheric pressure. The main interests of using LNG are for storage and transportation purposes since a volume of Natural Gas can be contained at a constant pressure in a volume 600 times smaller after liquefaction. LNG technology facilitates transportation of gas especially between remote countries which are not well connected with gas pipelines.

As far as safety is concerned, LNG is neither toxic nor corrosive and it does not cause skin burns. However, its vapour is flammable and can cause fire or

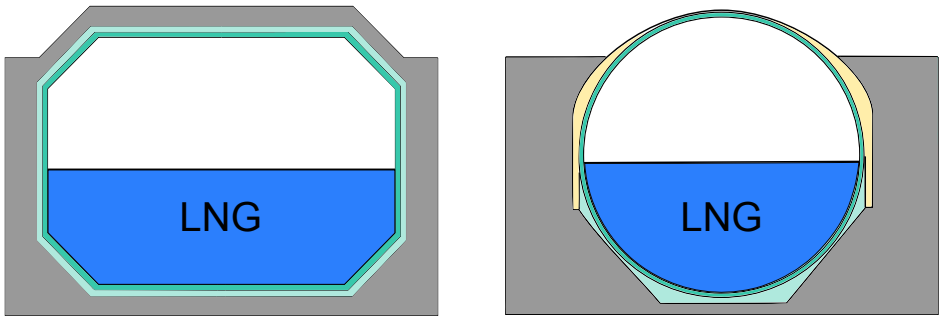

Figure 2.1: Cross sections of two different types of tanks onboard FLNG carriers

Source	LNG molar composition (%)						Density
	Nitrogen	***Methane***	***Ethane***	***Propane***	***Others***	***Total***	(kg/m^3)
Australia	0.04	87.33	8.33	3.33	0.97	100	467.35
Algeria	0.63	91.40	7.45	0.57	0.05	100	446.65
Libya	0.59	82.57	12.62	3.56	0.65	100	478.72
Qatar	0.27	90.91	6.43	1.66	0.74	100	453.46
USA	0.17	99.71	0.09	0.03	0.01	100	421.39

Table 2.1: LNG composition depending on its origin (extract from [20])

explosion in the presence of an ignition source.

LNG is usually stored in onshore receiving terminals in large cylindrical tanks able to contain up to 200,000 m^3 of liquid. Over nearly a decade, the trend has been towards the development of offshore receiving terminals, the Floating Storage Regasification Units (FSRU) which are floating vessels [5]. As an example, 6 of the 19 terminals currently under project are offshore ones [19]. In these floating vessels, LNG is stored in either Moss type carriers or membrane type carriers (Figure 2.1) which have different tank geometries than the cylindrical reservoirs used in onshore LNG terminals.

Besides, LNG is a liquefied hydrocarbon gas mixture and is mainly composed of methane, which represents around 90 % of its molar composition, as well as ethane, propane, nitrogen and some traces of heavier hydrocarbons. The recent multiplication of production sites has contributed to a diversification of LNG compositions and of LNG densities, given that it strongly depends on the composition of the liquid. As illustrated in Table 2.1 [20], LNG differs in composition and its corresponding density from one production site to another. As an example, LNG from USA is 10% less dense than australian LNG.

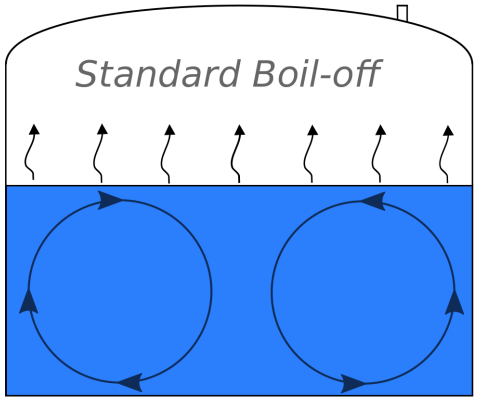

Figure 2.2: Convection cells in a uniform LNG [22]

2.2 Weathering and natural convection in homogeneous LNG

Despite their heavy insulations, some heat losses (≈ 10 W·m^{-2}) occur at the walls of LNG storage tanks. This heat coming in the tank is several orders of magnitude lower than the minimum heat flux causing the liquid to boil (≈ 10 kW·m^{-2}) [21]. As a result, there is no boiling in standard storage conditions but only surface evaporation. The term "boil-off rate" commonly used in the LNG industry hence corresponds in reality to the evaporation rate since there is no boiling inside the tank in normal conditions of use.

When LNG is placed in a tank, because of the heat losses at the walls, it is heated at the bottom and on the sides. Consequently, the liquid near the walls becomes lighter than the surrounding liquid and rises due to buoyancy. In a homogeneous LNG, once the liquid reaches the free surface, its most volatile components (CH_4 and N_2) evaporate and the remaining part is cooled down and sinks. This whole motion promotes the formation of convection currents in the tank as illustrated in Figure 2.2.

As a conclusion, LNG composition is altered with time because of the preferential boil-off of its most volatile components and so is its density. This phenomenon is called "weathering" or "ageing" and needs to be carefully monitored

to prevent LNG stratification.

2.3 Rollovers

2.3.1 The risks linked to rollovers

Rollover can be problematic from safety, environmental and financial perspectives. Its main hazard is due to the sudden evaporation accompanying the rapid mixing of a stratified LNG.

Firstly, this sudden evaporation may cause an overpressure inside the tank which could be potentially harmful to its structure. Then, to limit the overpressure, boil-off gases are vented out. However, not only are LNG vapours greenhouse gases, but they are also potentially explosive. Besides, when released into the atmosphere and before being warmed up by the ambient atmosphere, LNG vapour is denser than air and would tend, especially in a humid air, to reach the ground and accumulate, which increases the risks of meeting an ignition source. Lastly, releasing LNG vapours in the atmosphere is also a loss of income for the companies involved.

2.3.2 A threatening stratification

An essential condition to any rollover occurrence is the presence of an initially stable stratified LNG inside the tank. In such a configuration, a stratum of a less dense LNG lays above a stratum of a denser one. Two types of stratification are known and explained hereafter — the fill-induced stratification and the auto-stratification.

2.3.2.1 Fill-induced stratification

The fill-induced stratification is obtained after loading a liquid in a storage tank containing another liquid but with a different density. It may occur:

- after loading an LNG in a tank containing an LNG from a different production site,

- after loading an LNG in a tank containing an LNG from the same production site or with similar densities but whose composition and density had changed due to "weathering".

The risks of stratification are increased when the injected LNG, called "cargo", is loaded from the botton of the tank and below an initially present LNG, the "heel", but which is less dense. Similarly, injecting a heel at the top of a denser cargo, is also likely to lead to a stratified liquid. However, fill-induced stratification is not limited to these two cases.

2.3.2.2 Auto-stratification

An auto-stratification can occur in a storage tank containing an LNG when the liquid concentration in nitrogen is relatively high. Because of buoyancy, the liquid rises in the vicinity of the walls. When it reaches the surface, it flashes, the nitrogen evaporates suddenly given that its boiling temperature of 77 K is considerably lower than the liquid temperature which is around 113 K. Thus, the fluid at the surface becomes less dense, and, due to gravity it remains at the top of the liquid. As a result, a layer starts forming at the top of the liquid and grows as the flashing continues.

However, the stratification may break during the process if the top layer is not deep enough and the density difference between the layers large enough to prevent the penetration of the flow from the lower layer. Under such conditions, the layers are naturally mixed [23].

This type of stratification is rare compared to the fill-induced stratification and represents only a few cases. Considerable care is given to maintain the content of nitrogen to a lower value than 1% in order to neglect its effect and to prevent the liquid from auto-stratifying.

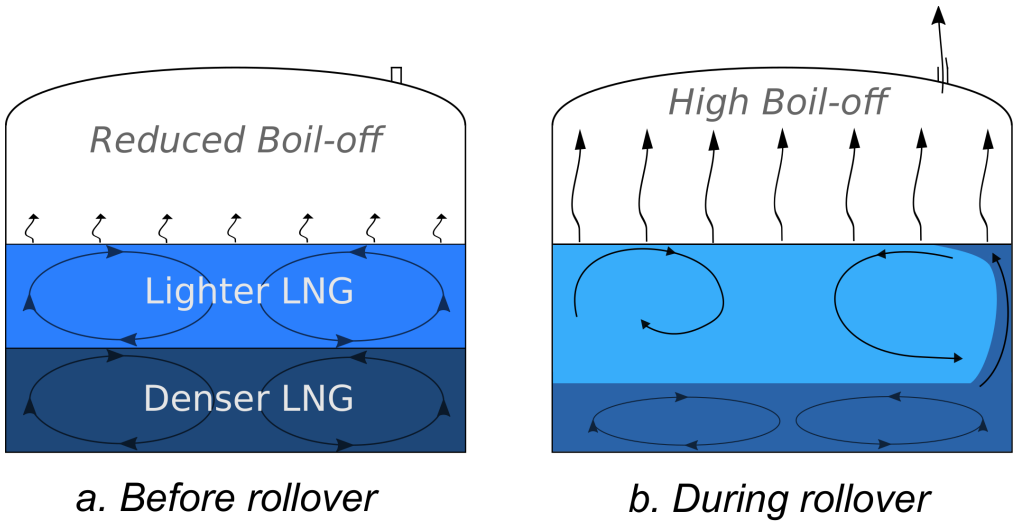

Figure 2.3: Stratified liquid before rollover (a) and during rollover (b) [22]

2.3.3 Rollover Scenario

As for rollovers, they always start from an initially stably-stratified liquid which is, as explained in Section 2.3.2, obtained either after loading a cargo or less frequently following an auto-stratification owing to a high nitrogen concentration in LNG.

In a stratified LNG and similarly to the flow in a homogeneous LNG described in Section 2.2, because of the heat ingress through the walls, the liquid rises in their vicinity and convection cells rapidly form in both layers. This phenomenon is illustrated in Figure 2.3(a).

On the one hand, the liquid in the lower layer is heated faster than in the top layer since it is heated by the side walls but also, mostly by the bottom wall. Besides, the heat transfer between the two layers is also limited due to the density difference between the layers which prevents the lower layer to release this extra energy. This accumulation of energy in the bottom layer — commonly called "superheating" among the gas industry — causes the temperature to rise within the layer, consequently decreasing its density. Moreover, because the energy from the lower layer cannot be released, the boil-off rate is also reduced when the liquid is stratified.

On the other hand, the density in the top layer increases as a result of the evaporation which densifies the top layer mainly through its cooling effect and also less significantly, when the concentration in nitrogen is negligible, through the preferential boil-off of methane.

Besides, the mass diffusion through the interface, although limited, also contributes to decreasing the density difference between two adjacent layers. As mentioned earlier, LNG is a mixture of methane and some heavier hydrocarbons. The mass diffusion at the interface between the two layers contributes to the slow homogenisation of the layers.

Moreover, the higher the density difference between two adjacent layers, the weaker the heat and mass transfers through the interface. This explains that while the density difference progressively decreases, the heat and mass transfers are intensified between the strata. Later, when the densities almost equalise, an intense and sudden mixing as illustrated in Figure 2.3(b) occurs while releasing the energy accumulated in the lower layer as large amounts of vapour. If the pressure inside the tank resulting from this incidental release exceeds a critical pressure, LNG vapours are vented out. The physical mechanisms driving rollover are sources of different interpretations which will be explained later in this chapter.

2.3.4 Historical rollover incidents

Assessing the frequency of the rollover occurrences is complex due to the significant number of actors in the LNG industry but also due to confidentiality issues. While 24 rollover incidents having occurred between 1965 until 2008 were reported to the GIIGNL group [24], Acton and van Meerbeeke [4] stated that only between 1970 and 1982 more than 41 rollover incidents occurred in 22 plants. Besides, according to Kulitsa and Wood [5] "rollover is a routine occurence"onboard FSRU where it has happened more than 20 times. Combining all these data to-

gether, it can be estimated that more than 70 rollover incidents have actually occurred. The latest reported incident to the GIIGNL group was from 2008 which emphasises that despite almost 50 years of research and significant resulting improvements in tank design and LNG handling processes, rollover events are still occurring. It is also likely that with the recent and significant development of the LNG industry, especially offshore, LNG rollovers become a topical issue.

Among the 24 incidents reported to the GIIGNL group, the three incidents in La Spezia in 1971, in Partington in 1993, and one aboard a Moss-Rosenberg type LNG carrier in 2008 have been documented and published in the public domain. These incidents are detailed hereafter to give the readers a more practical approach of the rollover phenomenon.

2.3.4.1 La Spezia incident, 1971 [6]

On the 21st of August 1971, in the SNAM LNG Terminal in La Spezia, Italy, 10 000 m^3 of LNG was already stored in the tank S-1 for more than a month and had time to weather when the Esso Brega cargo started to bottom-fill around 35 000 m^3 of heavier LNG. 18 hours after completed the loading, the pressure inside the tank suddenly rose to 710 mm of H_2O which is 200 mm above the nominal pressure. This overpressure forced the safety valves to lift. As a result, during the next 16 hours, around 185 tons of LNG vapours were vented out before the pressure inside the tank went back to normal.

After analysing the LNG compositions and densities depicted in Table 2.2, it turned out that the cargo was heavier than the heel initially present, and that the mixing during injection was minimal. As a result, the fluid became stratified and a rollover occurred justifying the pressure rise due to a significant LNG evaporation.

Following this incident, the tank roof suffered minor damages and some vapour drifted towards a public road nearby which had to be closed to prevent explosions. However, luckily, no injuries were declared. Moreover, in addition

	Cargo	***Heel***
Layer Height $[m]$	17.86	5
Composition $[\%mol]$		
Methane	62.26	63.62
Ethane	21.85	24.16
Propane	12.66	9.36
Butane	3.14	2.35
Pentane	0.07	0.16
Nitrogen	0.02	0.35
Density $[kg/m^3]$	544.6	528.6

Table 2.2: Composition and properties of the cargo and the heel before La Spezia rollover [6]

to being hazardous and to the potential cost of repairing the damaged tanks, LNG releases during rollovers are a loss of incomes for the terminal operating companies. Between 2008 up to now, the Henry Hub Natural Gas spot price, which corresponds approximatively to the Natural Gas price in North America, has ranged between 1.96 and 13 $/MMBtu. At the current Henry Hub Natural Gas spot price (on 01/05/2019) of 2.58 $/MMBtu [25] and considering a higher heating value of 52 MJ/kg [26], the loss of 185 tons of LNG vapour being vented out is estimated to worth approximatively $23,000.

La Spezia rollover incident was the first reported incident occurring in an LNG terminal and it raised the interest of many researchers involved in the LNG industry. It also paved the way for the development of predictive tools, and, for significant tank design improvements necessary to prevent and mitigate the effects of rollovers.

2.3.4.2 Partington rollover incident, 1993 [18]

The tank in Partington was initially filled with 17266 tons of LNG. Over a period of 11 days, 1533 tons of a denser liquid was top-filled which eased the mixing with the heel. Over the next 13 days, a lighter LNG less concentrated in heavy hydrocarbons and nitrogen was top filled. 68 days after the filling stopped, the tank pressure rose rapidly, lifting the relief valves and approximatively 150

tons of LNG vapour were released into the atmosphere.

2.3.4.3 Moss type carrier incident, 2008 [27]

Before that event was reported, it used to be thought that rollover could not occur in Moss type LNG tanks such as the one depicted in Figure 2.1 because of the natural mixing caused by the sea motion but also because of its spherical shape which promotes the convective motions within the liquid and its resulting mixing.

In 2008, a Moss type 125,000 m^3 LNG carrier discharged a cargo coming from Trinidad in the Far East while keeping 8,500 m^3 of LNG in two tanks to load later in the Mediterranean. The density of the heel was around 434 kg/m^3. Eight days later, while the vessel was on its way to the Mediterranean, it had to change its route for a port in Japan where it was loaded with a denser LNG with a density of 454 kg/m^3. The loading was more than twice longer than usual and was also interrupted during the process to make sure the cargo tanks were cooled sufficiently. This exceptionally slow loading process may have promoted the formation of a stratified LNG in the two tanks containing the LNG from Trinidad. Six days later, in these two tanks, the pressure rose and the LNG level decreased as a result of the sudden boil-off following the rollover. However, this was not a serious rollover especially because unlike during La Spezia or Partington incidents, the tank pressure did not exceed the design pressure and no vapour was vented out.

2.3.5 Rollover Management

In order to prevent rollovers and assess the risk of rollover occurrences, LNG tanks are equipped with real-time monitoring devices able to measure with accuracy the evaporation rate, the liquid level, the level of the interface between the strata as well as the vertical temperature and density profiles. These measuring

devices are used to detect the presence of stratification but also to monitor the efficiency of the methods adopted to prevent, eliminate or mitigate the stratification. Finally, the instrumentation also aims at collecting data which would be valuable especially in the event of a rollover.

Several methods are used to control rollovers by preventing the stratification during the filling process or if, despite the precautions taken during the filling, the LNG has stratified.

2.3.5.1 Prevention and elimination of the stratification

Stratification can first be avoided by storing, whenever it is possible, LNG with different compositions and significant density differences in distinct tanks. Also, avoiding the use of LNG with a concentration of nitrogen higher than 1% would reduce the risk of auto-stratification.

Then, when loading a cargo in a tank already filled with a heel but with a different composition, it is necessary to process by taking advantage of the natural mixing. Indeed, by processing with a bottom-filling if the cargo is lighter or with a top-filling if it is denser, it will promote mixing. In most of the cases, this operation will prevent the stratification.

However, it has been observed and simulated numerically by Koyama et al. [28] that bottom-filling a tank with a lighter LNG does not always prevent stratification. Utmost care must be taken when loading LNG with different densities in the same tank.

Some other devices like multi-hole tubes placed vertically or nozzle jets [3] can also promote the mixing of the liquids during the loading.

As soon as a stratification is observed, the tank pumps can also be used to recirculate the LNG and ensure its mixing. However, a weaker rollover may still occur during this process.

2.3.5.2 Intentional stratification

The loading process usually generates vapours which are sent to the energy consuming compressors for liquefaction. Since top-filling generates more vapour than bottom-filling, a growing trend is to load denser cargos below lighter heels [13] intentionally. In such a scenario, the heel is moved upwards, and the cargo sets at the bottom forming a stable stratification. However, because of the density difference and the overhead pressure of the top layer, the energy from the bottom layer is not released as vapours and the boil-off rate decreases saving a significant amount of energy by reducing the use of the highly consuming boil-off gas compressors. Such operations require high-accuracy monitoring devices as well as efficient mixing system to break up the stratification [3].
Rollovers, which occurred at least more than 24 times, are well-identified phenomena among the LNG industry. It has also been the topic of several experimental and numerical studies. On the one hand, several experimentalists have conducted rollover experiments with different liquids, both at small and large scales, in order to get some insights into this type of incident. On the other hand, some numericians have developed lumped-parameter models able to predict rollovers and widely used nowadays in the LNG industry [3]. Some researchers have also developed CFD models to visualise numerically the behaviour of the liquid. All these studies have helped to gain some insights into the physics underpinning the incident and will be detailed hereafter.

2.4 Double-diffusive convection

Similarly to natural convection, double-diffusive convections are fluid motions driven by buoyancy. While the latter, in the case of thermal convection is only affected by temperature differences, when dealing with double-diffusive convections, buoyancy is affected by the gradients of two diffusive properties with different diffusion rates.

The first historical studies on double-diffusive convections are focused on the thermosolutal convections observed in the sea where the two diffusive properties of interest are temperature and salt concentration. In this particular case, the thermal diffusion rate is larger than the salt diffusion rate. Depending on the vertical temperature and salt distributions in the sea, a salt finger regime and a diffusive regime have been observed by Turner [29].

However, it turns out that double-diffusive phenomena are not limited to oceanography but are also available in astrophysics, geophysics, and, in the context of this thesis, to the storage of Liquefied Natural Gas [30]. Besides, the two regimes observed in salt water, the finger and the diffusive regimes are also available in other liquids with a buoyancy affected by two physical properties with different diffusivities. The properties of interest herein are the temperature and the concentration of one or more species diluted in a solvent. It is important to mention that, from now on, the solutal expansion coefficients used in this thesis are always positive since for the different considered solutes, the more solute is available in the liquid, the denser the liquid is. Similarly, the thermal diffusivities are always greater than the considered solutal diffusivities.

For the sake of simplicity, in the following explanations about the two different regimes, it is considered that the liquid is a binary mixture and that the density of the liquid varies only with its temperature and concentration in solute.

2.4.1 Finger regime

The finger regime occurs when a layer of warmer and more concentrated in solute stands above a layer of colder liquid and less concentrated in solute. This regime is obtained when the destabilising parameter is the element with the weakest diffusivity such as the concentration in solute. It is easily observable in a continuously stratified liquid at rest. As depicted in Figure 2.4, a particle moved downwards from its equilibrium position will rapidly diffuse its heat inside

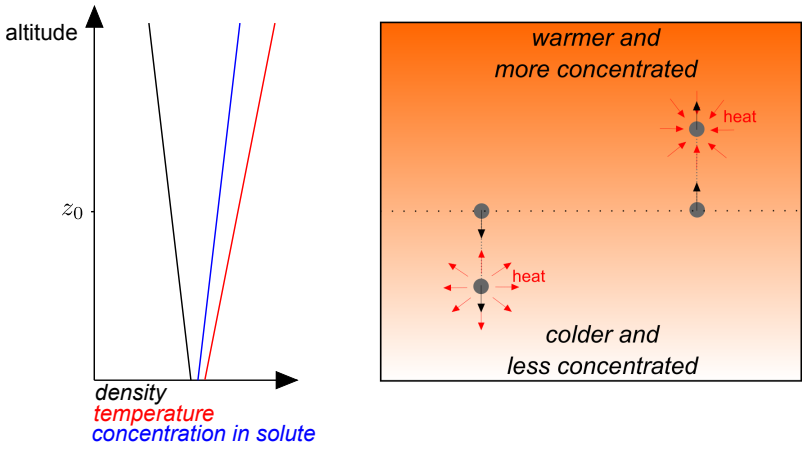

Figure 2.4: Explanatory diagram of the finger regime

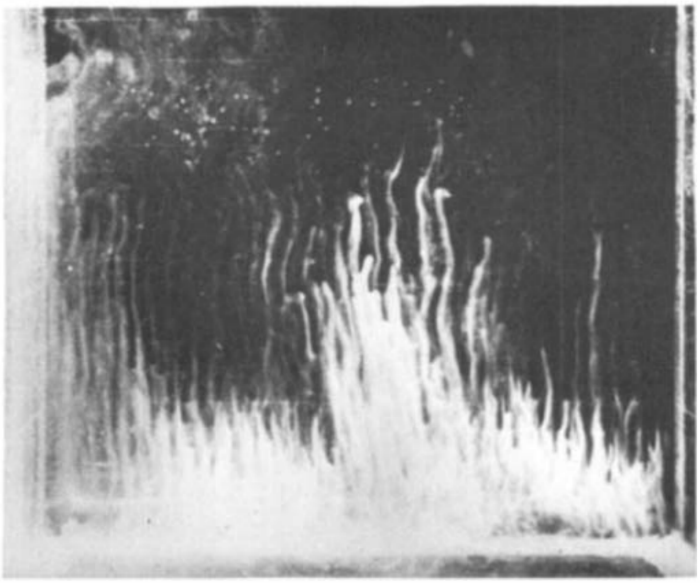

Figure 2.5: Experimentation of salt fingers conducted by Turner [31]

the colder liquid and adapt its temperature to the surrounding liquid. However, because it is more concentrated and so denser than the surrounding liquid, it will continue to move further from its initial position forming filaments called fingers as shown in Figure 2.5. A similar pattern can be observed by moving a particle in equilibrium upwards. The surrounding liquid will heat the particle making it lighter compared to the surrounding liquid, and due to buoyancy, it will continue to rise further away from its initial position.

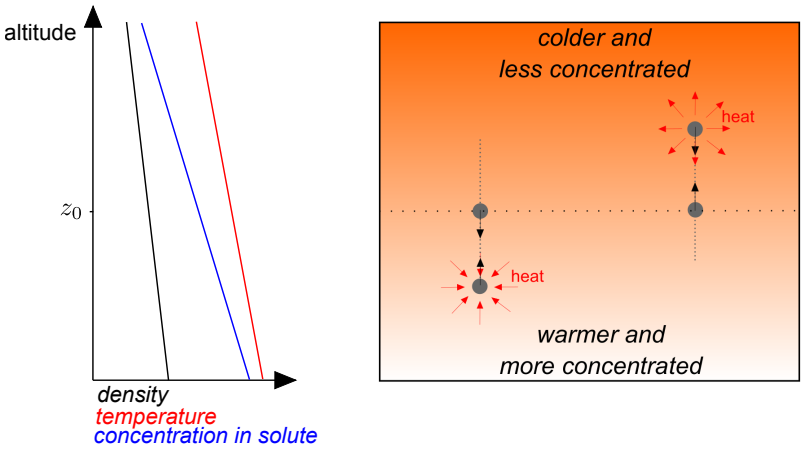

Figure 2.6: Explanatory diagram of the diffusive regime

2.4.2 Diffusive regime

On the opposite, the diffusive regime is obtained when a layer of colder and less concentrated in solute liquid lays above a layer of warmer and more concentrated liquid. It occurs when the destabilising parameter is the fast diffuser which is the temperature in this case, and which decreases with the altitude. In the case of a continuously stratified liquid and at rest, as shown in Figure 2.6, a particle moved downwards from its equilibrium position will rapidly gain heat from the surrounding liquid. As a result, it will become lighter than the surrounding liquid since it is less concentrated and warmer, and, due to buoyancy, it will start rising. The particle will even reach its initial position but, because it is warmer than the surrounding liquid, it will continue rising. Once the parcel has adjusted its temperature to the colder surrounding liquid, it becomes denser than the latter since density increases with concentration. As a result, it will start moving downwards overshooting once again its initial position. Because of the energy gained during the process and if not dampened by viscosity, the pattern is repeated growing in amplitude and forming unstable oscillations. Figure 2.7 shows the visualisation of a diffusive interface and convective plumes obtained by Turner [32] with a shadowgraph.

Double diffusion phenomena are also available in LNG which are liquids mainly made of methane, but which contains some other components in smaller

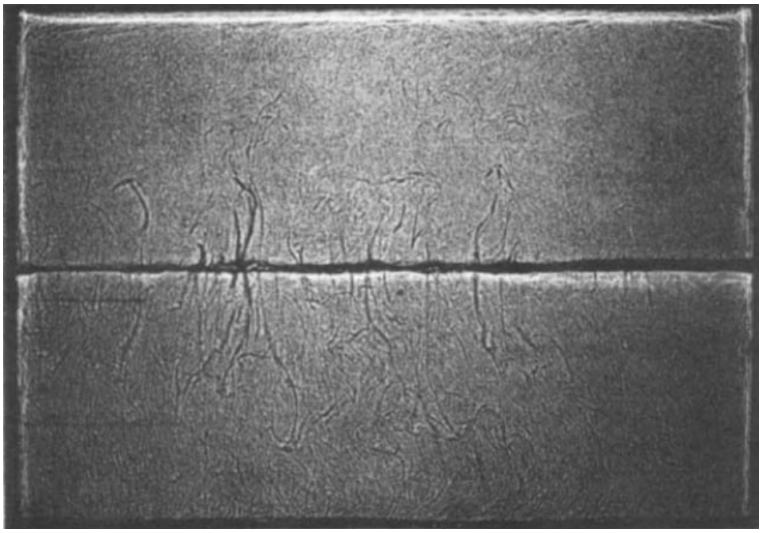

Figure 2.7: Experimentation of the diffusive interface conducted by Turner [32] with a solution of salt and sugar. Thanks to the shadowgraph, the convective plumes are highlighted near the interface.

extent. In the case of rollover, this can occur once the stratification is formed. The lower layer is initially more concentrated in solutes hence the stratification. Besides, because of the superheating, the layer rapidly becomes warmer while being more concentrated in solute. As a consequence, the diffusive regime is governing the heat and mass transfers through the interface separating the layers during the stage preceding the occurrence of rollover.

2.4.3 Turner's pioneering study

In 1967, Turner experimented with salt water the heat and mass transfers through the interface of a horizontally stratified liquid placed in a cylindrical container. The stably stratified liquid was made of two layers initially at the same temperature, and with the denser layer, richer in salt, located below the lighter layer. Besides, the lower layer was heated gently at the bottom while the interface was maintained sharp during all the experiment thanks to a mechanical stirring.

Turner identified that the stability of the stratification could be characterised by a parameter R, the stability parameter. The latter, which for consistency with

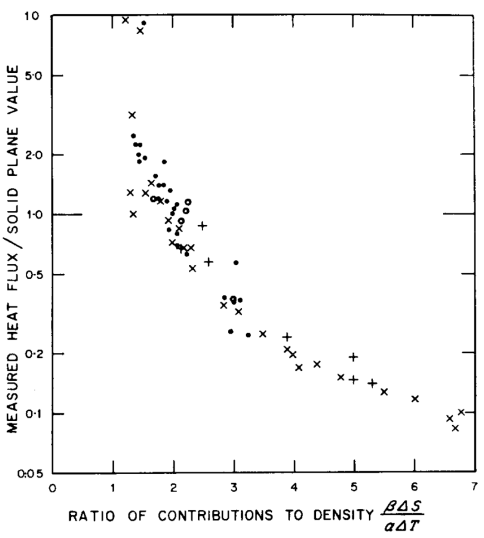

Figure 2.8: Ratio of the measured heat flux through the diffusive interface to its corresponding solid plane value as a function of the stability parameter for several heating rates (from [7])

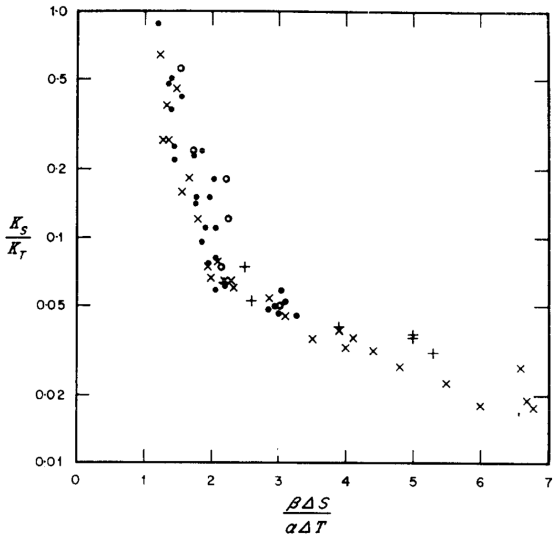

Figure 2.9: Ratio of the salt transfer coefficient to the heat transfer coefficient through the diffusive interface as a function of the stability parameter R for several heating rates (from [7])

the notations employed in this thesis, is defined as:

$$R = \frac{\beta_C \Delta C}{\beta_T \Delta T} \tag{2.1}$$

where ΔT is the difference between the temperature in the lower layer and the one in the upper layer. Similarly, ΔC is the difference between the concentration in the lower layer and the upper one. β_T and β_C are respectively the solutal and thermal expansion coefficients. The stability parameter reflects two trends:

- The more concentrated in salt the lower layer is compared to the upper layer, the more stable the layers are and the higher the stability parameter is.

- Inversely, the higher the temperature in the lower layer is compared to the temperature in the upper layer, the less stable the layers are and the lower the stability parameter is.

At first, while heating the lower layer, Turner compared the heat flux through

the interface supplied by the lower layer with the heat flux supplied by a solid plane at the same temperature. The experiment was repeated for several heating rates. The results provided in Figure 2.8 shows that the more stable the stratification is, the less significant the heat flux through the interface is compared the heat flux above a solid plane at the same temperature as the lower layer. The experiments have also highlighted than for small stability parameters ($R < 2$), the heat flux measured during the experiment through is higher than the heat flux transmitted by a solid plane at the same temperature as the lower layer in the experiment. This was explained by Turner as being the result of the wavy structure of the flow located at the interface as well as the breaking of the interface which were increasing the surface of contact between the layers promoting the heat transfer. Inversely, for high stability parameters ($R > 2$), the heat flux provided by a solid plane at the same temperature as the lower layer is greater than the one through the interface. Turner explained that it was due to the lifting of salt which was inhibiting the heat transfer.

The ratio of the effective salt transfer coefficient K_S to the effective heat transfer coefficient K_T was also monitored during the experiment. The results are depicted in Figure 2.9. For small stabilities ($R \approx 1$), the ratio is observed to be equal to 1 corresponding to the mixing of the layers when the same turbulent eddies are transporting the heat and the salt. Besides, the ratio K_S/K_T is observed to decrease while the stability grows. For high stabilities, the ratio becomes close to the ratio of the molecular diffusivity of salt to the molecular diffusivity of heat k_S/k_T. This implies that for high stabilities, the turbulence effects being suppressed, the molecular diffusions are governing the heat and mass transfers.

Correlations were derived from Turner's experimental results based on the idea that knowing the stability parameter and the temperature difference between two layers, the heat transfer could be derived following Figure 2.8 and consequently the effective heat and salt transfer coefficients following Figure 2.9.

Some years later, these correlations have served as a basis to several lumped-parameter rollover predictive models.

2.5 Evaporation at the free surface

Cryogenic liquids which are kept at low temperatures in storage tanks are sensitive to the residual heat leaks coming through the walls. In homogeneous liquids, including LNG, this energy in excess is released via evaporation or the so-called boiling-off.

Actually, the term "boiling-off" is not appropriate for LNG since the heat ingress through the walls — usually of the order of 10-15 $\mathrm{W{\cdot}m^{-2}}$ — is insufficient to permit the nucleations which would require a minimum heat flux of the order of 10 $\mathrm{kW{\cdot}m^{-2}}$ as suggested by Scurlock [21]. Besides, the saturation temperature growing with increasing pressure, it is even more difficult for the liquid to nucleate at the bottom of the liquid due to the head pressure (the latter providing an extra ~ 0.4 bar at the bottom of a 10-meter high liquid). As a matter of fact, Hashemi and Wesson [33] mentioned the absence of nucleation in LNG.

In 1971, these two researchers assimilated the flow near the evaporative free surface of a liquid, made of either salt water or LNG, to the flow between a heating plate and a cooling one. Thus, the following empirical relation, linking the Nusselt number Nu to the Rayleight number Ra and demonstrated for the flow a liquid placed between two rigid walls is also valid:

$$Nu = C_{m_0} Ra^{1/3} \tag{2.2}$$

with C_{m_0} a constant taken equal to 0.13.

In terms of heat flux, Equation 2.2 yields to:

$$q = C_{m_0} \lambda \left(\frac{\beta_T g}{\alpha \nu} \right)^{1/3} (\Delta T)^{4/3} \tag{2.3}$$

where ΔT is the difference between the temperature at the cooling plane and the temperature at the heating plane.λ, β_T, α and ν are respectively the liquid thermal conductivity, thermal expansion coefficient, thermal diffusivity and kinematic viscosity. From equation 2.3, they derived the so-called Hashemi-Wesson relation which links the evaporative heat flux q to the difference between the temperature at the free surface $T_{surface}$ and the bulk temperature T_{bulk}, defined as the superheat temperature:

$$q = C_m \lambda \left(\frac{\beta_T g}{\alpha \nu} \right)^{1/3} (T_{bulk} - T_{surface})^{4/3} \tag{2.4}$$

where C_m is equal to 0.328.

Given that the liquid is assumed in equilibrium with the surrounding vapour, the temperature of the liquid in contact with the vapour is equal to the saturation temperature T_{sat}. As a consequence, Equation 2.4 becomes:

$$q = C_m \lambda \left(\frac{\beta_T g}{\alpha \nu} \right)^{1/3} (T_{bulk} - T_{sat})^{4/3} \tag{2.5}$$

Finally, knowing that $q = \dot{m} L$ with $\dot{m}$ and L, respectively, the boil-off rate and the latent heat of vaporisation, the boil-off rate can then be derived from Equation 2.5 as follows:

$$\dot{m} = C_m \frac{\lambda}{L} \left(\frac{\beta_T g}{\alpha \nu} \right)^{1/3} (T_{bulk} - T_{sat})^{4/3} \tag{2.6}$$

An interesting characteristic of this relation is that it is also valid for pressure changes inside the tank. In the case where the pressure increases following a sudden rise in boil-off rate, the saturation temperature will increase, and, as a consequence, the evaporation will decrease. Similarly, if the pressure decreases following the valve opening, for example, the saturation temperature will decrease, and the evaporation rate will increase.

Doyer et al. [34] validated with experiments this relation by monitoring the evaporation in an LNG tank as well as the generated superheat. Clegg and

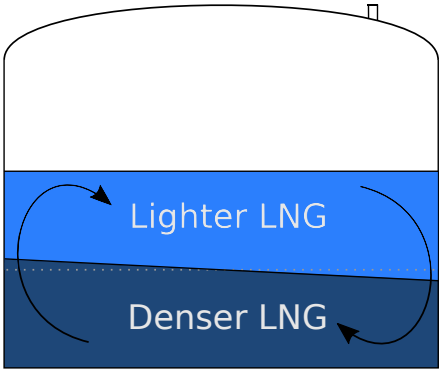

Figure 2.10: Initial representation of the rollover phenomenon

Papadakis [35] found out that the equation was still valid for a solution of Freon provided that the constant C_m is taken equal to 0.27.

Lemembre [16] considered an alternative version of Hashemi-Wesson equation by assuming that the evaporation was controlled by a thin layer below the free surface. As a result, Lemembre considered equation 2.3 valid locally and the best results were obtained considering a layer equal to 1/100 of the total height located right below the free surface.

2.6 Rollover experiments

The term "rollover" was initially used to name the LNG behaviour causing the large release of boil-off gases. Indeed, it used to be thought that, due to the combined actions of the heat and mass transfers through the diffusive interface, of the cooling free surface and of the heat losses near the walls, the densities in the upper layer and in the lower layer equalising, the two layers were swapping their position by "rolling over" each other as represented in Figure 2.10.

In order to understand better the complex physics underpinning rollovers, several experiments have been conducted. Because LNG is not easy to handle and requires extremely well-insulated tanks to be maintained into its liquid state, other liquids are generally used to experiment the rollover phenomenon. Hence,

mixtures of liquid oxygen and liquid nitrogen [36], salt water [7, 37], aqueous solutions of ethanol [38] and mixtures of Freon 11/113 [39] were used. Their main advantage is that they are all in their liquid state at standard temperature and pressure and Freon was used because it is a cryogenic liquid evaporating at room temperature. Besides, for the sake of simplicity and convenience, researchers have generally chosen to use small-scale experiments with dimensions typically smaller than a meter. Nonetheless, two studies [40, 41] have been conducted using LNG, the first one with a real tank and the second one with a experimental 8-meter diameter tank which is smaller than standard tanks but large enough to experiment large-scale phenomena.

During all these experiments, different conditions have been tested (heating, initial density differences, stratifications) and will be detailed hereafter.

2.6.1 The effects of bottom wall heating only

Bergman [42], Turner [29], Kazmierczak [43] and Crapper [44] studied the effect of heating below a stably-stratified fluid made of salt water. In all these experiments, the growth of the bottom layer was observed as well as the formation of intermediary layers. Bergman [42] noticed that the stratified fluid was behaving similarly to experiments where convective motions were formed driven externally after applying a shear stress [45] or stirring using an oscillating grid [46] at one of the boundaries. In such a case of asymmetrical stirring, the interface moves away from the region of more intense stirring until the entrainment rates in both layers balance. On the contrary, if the stirring is symmetrical in both layers, the interface is kept sharp and maintained in its position. Also, the turbulence is observed to be strongly damped at the interface. In his pioneering study regarding the study of the heat and mass transfer through the diffusive interface [7], Turner used mechanical stirring at the top of the stratified liquid to compensate the entrainment rate of the bottom layer generated due to the

heating as well as to sharpen the interface.

In 1983, Nakano et al. [8] conducted several rollover experiments with a stratified liquid of Freon 11/113 including one where the liquid was only heated from below. In the first part of the experiment, the interface between the two layers started to move upwards as expected from Turner's observations. After some time, the upward motion of the interface stopped and, later, a sudden mixing was observed. It is likely that the evaporation at the free surface, and more significantly, its cooling have contributed to the compensation of the entrainment of the heated lower layer by entraining the upper layer and then stopping the upward motion of the interface. Later on, the sudden mixing occurred when the densities in both layers almost equalised.

2.6.2 The effects of side wall heating only

When heating only the side walls, Morioka and Enya [37], Nakano et al. [8] and Arita [38] observed in rectangular tanks, respectively, with salt water, a mixture of Freon and an aqueous solution of ethanol that the mixing was due to a "boundary layer pattern penetration" as illustrated in Figure 2.11. Morioka and Enya [37] described the rollover of a stratified liquid heated on its side, as being the result of the diffusion of heat and mass through the interface between the two layers, progressively reducing the density difference between the two layers. These three groups of researchers all agreed on the fact that when the density difference becomes relatively close, a superheated thin layer from the lower layer penetrates inside the top layer breaking the interface near the wall forming small channels. However, in the upper layer, the liquid further from the wall does not have enough energy to break the interface. The liquid from the bottom layer is then drained through these "improvised" channels and contributes to the downward motion of the interface until its disappearance.

Morioka and Enya [37] demonstrated the influence of the initial relative den-

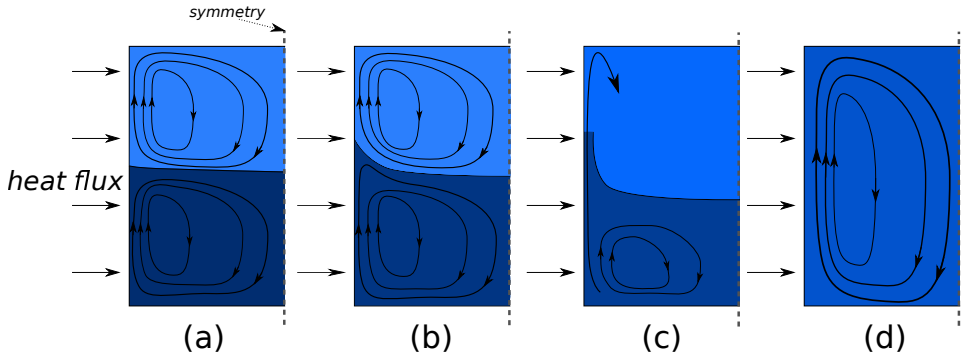

Figure 2.11: Scheme illustrating one side of the liquid during the different stages of the rollover phenomenon as observed by Arita et al. [38]: (a) initial stratification (b) fully-developed convection (c) penetration of a superheated layer (d) homogenised liquid

sity difference and the heating intensity on the rollover incubation time which is the time before the mixing starts as well as on the mixing time (or duration of mixing). They observed that the higher the relative density difference is, the longer the incubation time is, and so is the mixing time. On the contrary, the higher the sidewall heat flux is, the shorter the incubation time and so is the mixing time.

However, Agbabi [36] and Shi [14] observed a different pattern while heating on the side only, respectively, a mixture of liquid nitrogen and liquid oxygen, and, a mixture of Freon 11 and Freon 113. As illustrated in Figure 2.12, it was clear in their experiments that the mixing was due to the entrainment caused by the convective motions in the top layer contributing to move the interface downwards. Whereas Agbabi only observed this downward motion, Shi noticed that eventually, the core flow from the top layer had penetrated inside the bottom layer breaking the interface and homogenising the liquid.

2.6.3 The effects of combining side and bottom wall heating

In 1981, Morioka and Enya [37] demonstrated that combining side heating and bottom heating makes the motion of the interface more sudden than when

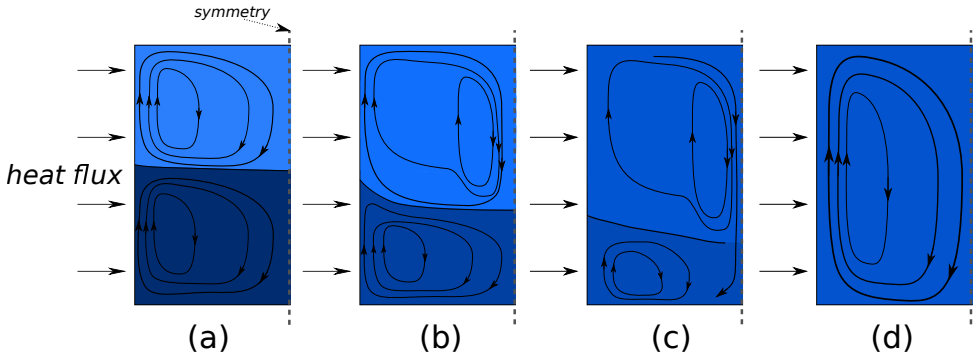

Figure 2.12: Scheme illustrating one side of the liquid during the different stages of the rollover phenomenon as observed by Shi et al. [39]: (a) initial stratification (b) fully-developed convection (c) the core flow breaks the interface (d) homogenised liquid

heating on the side only and defined the notion of mixing distance which is the depth at which the interface disappears. It turned out that at a constant heating intensity at the side walls, increasing the heating at the bottom shortens the mixing time. Unlike for the case of side heating only, their interpretation of the physics is not clear. Later, in 1993, Shi [39] highlighted that combining bottom heating to side heating results in sharpening the interface between the layers. Also, he observed a similar mixing to the one obtained with side heating only but he noticed that bottom heating was accelerating and increasing the superheating of the bottom layer and, as a consequence, quickens the occurrence of rollover. Finally, similarly to Morioka's observation, heating below promoted the acceleratation of the interface downward motion. By comparing Morioka and Enya's results with Shi's, it turns out that combining bottom heating to side heating promotes the rapid descent of the interface.

Besides, earlier, in 1983, Nakano et al. [8] studied the influence of different heatings on rollovers including the combination of bottom and side heating. In this case, they observed two types of mixing depending on the intensity of heating below the tank. The first type of rollover observed was a sudden mixing and the second type was due to the penetration of a boundary layer from the bottom layer inside the top layer.

Experiments with LNG are less frequent due to its low boiling point and the

difficulty to conduct experiments with the corresponding insulated reservoirs in a laboratory. However, some data are available in the literature coming mainly from the aforementioned La Spezia [6] and Partington [18] incidents. There were also some experiments conducted in collaboration between several main actors of the oil and gas sector [41] in a medium-scale cylindrical tank (8-meter-high and 8-meter-wide) but very few results are publicly available except the rollover experiment used as a reference in Bates and Morrison's study [84]. Sugawara et al. [40], in 1983, also studied LNG rollovers in a standard (large-scale) tank. Among the different test cases, they noticed that the entrainment was the dominant phenomenon driving the rollover.

2.6.4 Intermediary layer

It is very common that an intermediary layer is formed either during the injection of a denser LNG below a lighter one or of a lighter one at the top of a denser one. This intermediary layer is due to the mixing obtained during the injection of LNG. This phenomenon has been observed by Sugawara et al. [40] during their rollover experiments with LNG.

They remarked without going into details that this intermediary layer was affecting the heat and mass transfer between the layers. During the period prior to mixing, the intermediary layer depth was decreasing progressively as a consequence of the convective motion both in the top and in the lower layers resulting in a sharper interface. It was until then known that the boil-off rate was increasing during the final mixing of the layers. However, Sugawara et al. have also demonstrated that the boil-off rate may also increase briefly when the intermediary layer disappears, probably because of its slight superheat.

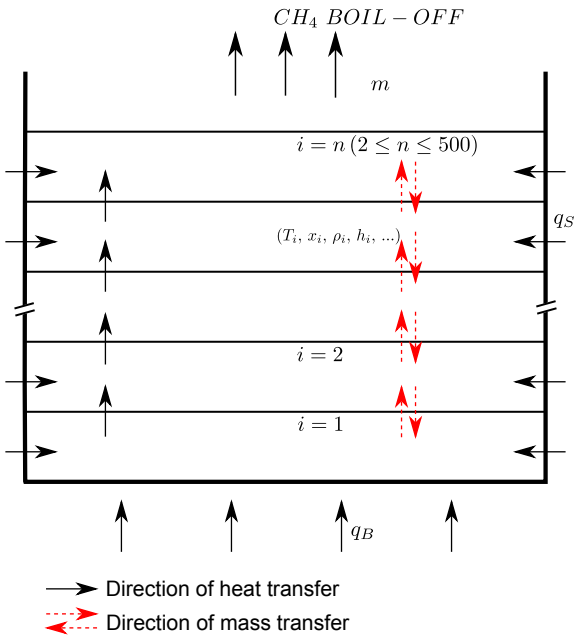

Figure 2.13: Model of an initially stratified liquid used by Chatterjee and Geist (adapted from [9])

2.7 Numerical models

La Spezia incident which has been well documented by Sarsten [6] not only motivated many researchers to develop mathematical models capable of modelling rollovers reliably, but also provided data for validation purposes. The GIIGNL group [3] has recently counted seven different codes currently used in the industry to predict rollovers and which are all mainly based on the same principles as the early models developed by Chatterjee and Geist, Germeles and Heedstand et al. These models are presented hereafter.

2.7.1 Chatterjee and Geist, 1973 [9]

In order to predict rollover, Chatterjee and Geist [9] developed a lumped-parameter model. In their model, they assumed that LNG is a binary mixture made of methane and another non-volatile component. They also considered that, following the loading process, the liquid is composed of n homogeneous layers of LNG where concentration in methane and temperature are constant over the layer. The layers are considered separated from each other by a sharp

interface. Besides, the interfaces between the layers are located at fixed locations.

The numerical model is based on the heat and material balance (molar fraction in methane) equations for each layer as follows:

$$\left.\begin{aligned} h_i\rho_i c_{p_i}\tfrac{\partial T_i}{\partial t} &= q^B + \tfrac{4}{D}q^s h_i + q_i^H(T_{i+1}-T_i) \\ h_i\rho_i \tfrac{M}{M_i}\tfrac{\partial x_i}{\partial t} &= -q_{i+1}^M(x_{i+1}-x_i) \end{aligned}\right\} i=1 \tag{2.7}$$

$$\left.\begin{aligned} h_i\rho_i c_{p_i}\tfrac{\partial T_i}{\partial t} &= \tfrac{4}{D}q^s h_i + q_{i-1}^H(T_{i-1}-T_i) - q_i^H(T_i-T_{i+1}) \\ h_i\rho_i \tfrac{M}{M_i}\tfrac{\partial x_i}{\partial t} &= q_{i+1}^M(x_{i+1}-x_i) - q_i^M(x_i-x_{i-1}) \end{aligned}\right\} i=2\ to\ n-1 \tag{2.8}$$

$$\left.\begin{aligned} \dot{m}L &= \tfrac{4}{D}q^s h_i + q_{n-1}^H(T_{i-1}-T_i) \\ h_i\rho_i \tfrac{M}{M_i}\tfrac{\partial x_i}{\partial t} &= -\dot{m} - q_i^M(x_i-x_{i-1}) \end{aligned}\right\} i=n \tag{2.9}$$

where q_{i+1}^H and q_{i+1}^M are respectively the heat and mass transfer coefficients between the layer i and the layer $i+1$. These coefficients are calculated by adapting the results obtained by Turner [7] with salt water to LNG. Density in each layer depends on the composition and the temperature, but the relation is not explicitly given. There is also no information given about the way the boil-off rate $\dot{m}$ is calculated by the authors but the temperature in the top layer is assumed equal to the saturation temperature. Regarding the mass transfer between the layers, it is assumed to be equimolar, so the number of moles is constant in each layer except in the top and the bottom ones.

An important aspect of their work is the definition of mixing between two adjacent layers adopted by Chatterjee and Geist. When the temperature difference becomes small enough ($\Delta T < 0.05$F) as well as a the difference in concentration in methane ($\Delta x < 0.002\%$), then the interface between two adjacent layers breaks and a single layer is formed. Rollover occurs once the last two layers are mixed.

In 1977, Chatterjee and Geist [23] considered LNG as a mixture of methane, ethane and nitrogen. The evaporative condition was also modified and modelled

using the standard equation for flash calculations.

2.7.2 Germeles, 1975 [10]

The model used by Germeles [10] and developed within Cabot Corporation by Heestand is similar in many points to the one previously developed by Chatterjee and Geist [9]. Indeed, the heat and material balance equations are similar and the heat and mass transfer coefficients are also obtained from the adapted version of Turner's correlations [7]. However, some major differences exist:

- LNG is assumed to be a binary mixture composed of methane and another fictitious component representing the effects of all the other components of LNG. Besides, unlike Chatterjee and Geist [9] who studied the transport of methane through the interfaces, Germeles focused on the transport of the fictitious solute.
- Density is calculated from Boyle's table [47].
- The boil-off rate is calculated from Hashemi-Wesson [33] relation and the saturation temperature considered in the equation is calculated from Clapeyron equation.
- Germeles' criterion for mixing is also different than Chatterjee and Geist's one. Indeed, instead of considering the equalisation of both temperature and concentration in methane in two adjacent layers, he considered the density equalisation between two adjacent layers as the criterion for mixing. Rollover occurs when the last two layers mixes. Germeles' mixing criterion is less restrictive than Chatterjee and Geist's one. Indeed, temperature and concentration equalisations would lead to density equalisation but, the latter can also be obtained when the stability parameter tends to 1.

2.7.3 Heestand et al., 1983 [11]

The model developed by Heedstand et al. [11] (the HSM model) is an extension of their previous approach reported by Germeles [10] and includes several components of LNG which are methane, ethane, propane, butane and nitrogen. They adopted the same mixing criterion as Germeles, namely the density equalisation between two adjacent layers. Similarly to the previous models, the method is based on the heat and material balance equation. However, the heat and mass transfer coefficients are not calculated using Turner's correlations [7] which according to the authors tend to underestimate the mass transfer between the strata. Instead, they assumed that the transfer between two layers is fully turbulent. The heat transfer coefficients are calculated from Globe and Dropkin [48] and McAdams [49] correlations, and, then, the mass transfer coefficient is derived using the Reynolds analogy.

Regarding the evaporation, it is modelled using a modified version of Hashemi-Wesson [33] relation taking into account the density difference instead of the temperature difference.

2.7.3.1 Other research studies

The main interest of Bates and Morrison's work [84], published in 1997, is the identification of two phases during the transition of a stratified liquid to the rollover occurrence. The first part is dominated by double-diffusive convections contributing to lower the density difference between the layers. They simulated this phase using a model similar to the HSM model but with the heat and mass transfer coefficients derived from Turner's correlations. Later on, once a stability parameter becomes small enough and reaches a critical stability parameter, they consider that the interface becomes more unstable and is from then on entrained driven by penetrative convections. This second phase is modelled using an approximate method requiring the experimental entrainment rate and the rate

of change of interfacial density difference. Their results highlighted the importance of entrainment mixing which homogenises the liquid more efficiently than double-diffusive convection alone.

Nakano et al. [8] and Sugawara [40] also extended the earlier model reported by Germeles [10] to take into account the motion of the interface resulting from the entrainment rate via empirical laws. Although the numerical results overpredict the rollover time when compared to Nakano et al. experiments with Freon, they seem to show relatively good agreement with La Spezia incident data [6].

Lukaszewski et al. [50] and Deshpande et al. [51] developed a model based on the HSM model [11]. However, in order to avoid the use of existing empirical correlations to calculate the heat and mass transfer coefficients, these parameters are calculated from real-time Level Temperature Density (LTD) profiles and inverse methods which are either optimisation methods or a normal equation algorithms.

2.7.4 Parametric studies

An interest in using numerical models is the relative easiness to handle the main parameters ruling the phenomenon without having to change the whole set-up. Chatterjee and Geist [9] and some years later, Germeles [10] exploited this aspect to assess the influence of several parameters on rollover. In particular, they noticed that:

- increasing the initial density differences delays the rollover occurrence and increases the peak of boil-off rate.
- increasing the bottom layer and/or decreasing the height of the top layer delays the rollover occurrence and increases the peak of boil-off rate.
- increasing the heat leaks accelerates the rollover occurrence while decreasing the peak of boil-off rate.

As a result, these results confirm the influence of both the relative density

difference and the heating on the rollover time and mixing time as experimented by Morioka and Enya [37].

2.8 Computational Fluid Dynamics (CFD)

In 1993, Shi [14] developed a code based on a finite volume method able to model the spatial behaviour of the rollover phenomenon. His code was using the Boussinesq approximation, and density was varying linearly with temperature and solutal concentration. The numerical instabilities mainly coming from the computer round-off errors and the absence of turbulence modelling limited his study to cases where the Rayleigh number remains lower than 10^8. As a result, he could not model rollovers in LNG tanks where typical Rayleigh number are several orders of magnitude higher. However, while simulating rollovers in mixtures of liquid oxygen and liquid nitrogen, he observed with 2D numerical models the same physical patterns as in his experiment with a mixture of Freon 11/Freon 113 [39]. Indeed, he noticed that there are two parts in the rollover process. Firstly, it starts with a migration of the interface and then a rapid mixing of the layers occurs. According to Shi, the rollover phenomenon is obtained as a result of different entrainment rates in both layers. The convective cells and the downward core flow in the top layer when impinging on the interface between the two layers promote the entrainment of the heavy particles from the bottom layer into the top layer. As a result, the decrease in density difference and the growing convective cells in the top layer cause the interface to migrate downwards until complete mixing.

Munakata et al. [15], in 1995, as well as Lemembre [16] in 1999 used a similar numerical approach to the one developed by Shi but based on finite differences. The fluid in Munakata et al.'s study is a mixture of water and ethanol while in Lemembre's study it was either salt water or LNG. However, they both assumed that the heating from below was secondary so they only considered side heating

to simplify the study. Unlike Shi's foundings [14], they both observed from their 2D or axisymmetric simulations that the simulated rollovers are obtained after a buoyant layer of liquid from the bottom layer penetrates into the top layer. Besides, Munakata et al. [15] observed numerically that increasing the initial concentration difference is stabilising the interface and delays the onset of rollover time. On the opposite, increasing the heat flux on the side walls shortens the onset of rollover time.

As a result, Munakata et al. confirmed qualitatively with the experiments conducted by Arita [38] that the rollover is the result of the penetration of a buoyant layer from the lower strata into the upper one. This process illustrated in Figure 2.11 contradicts both Shi's experimental and numerical foundings [39] which identified the entrainment mixing as the cause of rollover contributing to the downward motion of the interface. It turns out that two distinct phenomena are responsible for the occurrence of rollover.

In addition, regarding the modelling of the evaporative boundary condition, Shi assumed that the temperature at the surface is equal to the saturation temperature which is considered as constant during the simulation. Munakata et al. [15] considered an adiabatic boundary condition at the interface liquid-vapour. As for Lemembre [16], he used a local adaptation of Hashemi-Wesson relation as defined earlier. However, none of these researchers did observe any peak of boil-off release possibly because by neglecting the heating below, they were underestimating its actual influence on the superheating of the bottom layer.

2.9 Summary and challenges

Rollover predictive software programs used in the industry are based on lumped-parameter models. To model the heat and mass transfers at the interface, they require empirical correlations. However, it turns out that the results are very dependent on the correlations whether it is Turner's [7], Globe and Drop-

kin's [48] or McAdams' [49]. To limit this sensitivity, Lukaszewski et al. [50] and Desphande et al. [51] haved developed inverse methods to predict accurately the heat and mass transfer coefficients thanks to real-time data obtained via probes placed in the studied tank. Although these studies show good results, it limits the study to tanks fitted with this type of equipment.

Besides, as it has been observed experimentally by Sugawara et al. [40] in an LNG tank, entrainment mixing plays an important role in the density equalisation preceding LNG rollovers. A consequence resulting from the difference of entrainment mixing in both layers is the vertical motion of the interface. This phenonemenon has also been observed experimentally and numerically by several researchers [7, 14, 84]. While the initial models which are widely used in the industry do not take into account this migration stage, Nakano et al. [8] and Sugawara et al. [40] have included it in Germeles' model [10]. Although this improvement is important, it is based on empirical laws which relates the entrainement rate to the overall Richardson number.

As a conclusion, lumped-parameter models can give realistic predictions, but the results are very sensitive to the empirical laws employed. Besides, their results can not give a spatial representation of the rollover phenomenon which would help to gain physical insights into the mechanims driving the rollover instability.

In order to overcome these issues, it has been thought, thanks to the recent increase of computational resources, to develop a CFD model to simulate rollovers. This method has the advantage to decrease the number of uncertainties mainly involved in the heat and mass transfers through the diffusive interface but also regarding the vertical motion of the interface.
While the initial idea of two layers "rolling over" each other and swapping position has been abandoned early, it is still not clearly understood which phenomenon is driving the rollover. Several phenomena have been previously identified by researchers:

- the entrainment through the diffusive interface via penetrative convections,
- the vertical motion of the interface resulting from the difference in entrainment mixing between two adjacent layers,
- the penetration of a supersaturated layer from the bottom layer near the wall breaking the interface.

CFD would then be also very useful to understand the physics underpinning the rollover instability.

Small-scale rollover experiments are interesting from a physical point of view but can not reflect the influence of the large scales. The modified Rayleigh number defined as $Ra^* = \frac{g\beta_T q L^4}{\nu\alpha\lambda}$ which characterises natural convective flows shows that increasing the heat flux would compensate the small scales of the experiment. However, given the power four applied to the characteristic length scale, it would require a drastic increase in heat flux which would potentially cause the liquid to nucleate and which is not representative of the physics involved during rollover.

As a consequence, only large-scale rollover experiments would be able to reflect the influence of the large scales and turbulence. However, there is an important lack of data publicly available in this field which is also one of the difficulties of this study. An other interest of employing CFD methods for this type of studies is that once settled, it is relatively easy to change the characteristic parameters and the tank geometry without taking into account all the safety-related and cost issues involved with large-scale experiments. These simulations would help to gain some substantial knowledge about the rollover mechanisms.

Several CFD studies [16, 14, 15] have been conducted but due to the restrictions in computational power, they were limited to symmetric 2D or axisymmetric models. Moreover, these models were assuming a laminar flow which does not reflect the influence of turbulence in real tank.

Some of these CFD models have shown good qualitative agreements [14, 15]

with experimental data but no quantitative comparisons have been conducted preventing these researchers from using these models for prediction purposes. The challenge in this thesis is to develop a predictive CFD code which would also give good agreements with experimental data. Besides, this code will also be extended to take into account the influence of turbulence and the properties of LNG will be implemented to ensure best accuracy.

Finally, developing a predictive CFD code will also be useful to deal with more complex geometries than onshore storage tanks and will be able to simulate rollovers in FLNG storage tanks such as in Moss type carriers.

Chapter 3

Governing equations

The following chapter aims at describing the equations used in the proposed method for the predictive modelling of rollovers. To this aim, the assumptions and equations governing the physics involved during rollovers will be explained in a first part. In a second part, the numerical models selected to simulate the turbulence and the surface evaporation will be justified.

3.1 Mathematical formulations

Fluid dynamics can be described mathematically by using a mass conservation equation, the so-called continuity equation, and a momentum equation. In order to reliably model the physics involved during rollover, it is also necessary to consider the internal energy equation which governs the heat tranfer, and transport equations to model the diffusion of the species present in the liquid of interest.

3.1.1 Continuity equation

The conservation of the mass of fluid is described by the continuity equation as follows:

$$\frac{\partial \rho}{\partial t} + \nabla.(\rho \boldsymbol{u}) = 0 \tag{3.1}$$

with ρ the liquid density and $\boldsymbol{u}$ its velocity.

As far as incompressible fluids are concerned, the continuity equation can be simplified as:

$$\nabla.\boldsymbol{u} = 0 \tag{3.2}$$

which in Einstein's notations, can be written as:

$$\frac{\partial u_i}{\partial x_i} = 0 \tag{3.3}$$

3.1.2 Momentum equation

The momentum equation is derived from Newton's second law and ensures that the rate of change of momentum is equal to the sum of the forces acting on the fluid. The momentum equation for an incompressible fluid can be written as follows:

$$\rho\left(\frac{\partial \boldsymbol{u}}{\partial t} + (\boldsymbol{u}.\nabla)\boldsymbol{u}\right) = -\nabla p + \nabla.\bar{\bar{\boldsymbol{\tau}}} + \boldsymbol{S_M} \tag{3.4}$$

where $\boldsymbol{S_M}$ stands for the momentum source and includes the effects of body forces only (for example gravity, centrifugal or Coriolis forces), $\bar{\bar{\boldsymbol{\tau}}}$ is the deviatoric stress tensor accounting for the effect of viscosity and p is the pressure. Because the body forces acting on the fluid involved, before and during rollover, are solely gravity forces, Equation 3.4 can be reduced to:

$$\rho\left(\frac{\partial \boldsymbol{u}}{\partial t} + (\boldsymbol{u}.\nabla)\boldsymbol{u}\right) = -\nabla p + \nabla.\bar{\bar{\boldsymbol{\tau}}} + \rho\boldsymbol{g} \tag{3.5}$$

As far as the frame of reference is concerned, in all the thesis hereafter, it is chosen such as the gravity vector $\boldsymbol{g}$ is aligned with the Z-axis and $\boldsymbol{g} = (0, 0, -g)$. The X and Y-axis are horizontal and selected so that the frame of reference is direct.

In Einstein's notations, Equation 3.5 becomes for i=1,2 or 3:

$$\rho\left(\frac{\partial u_i}{\partial t} + u_j\frac{\partial u_i}{\partial x_j}\right) = -\frac{\partial p}{\partial x_i} + \frac{\partial \tau_{ij}}{\partial x_i} + \rho g_i \tag{3.6}$$

Besides, given that the liquids considered in this thesis are newtonian, the deviatoric stress tensor can be formulated as:

$$\tau_{ij} = \mu\left(\frac{\partial u_i}{\partial x_j} + \frac{\partial u_j}{\partial x_i}\right) - \frac{2}{3}\mu\delta_{ij}\frac{\partial u_k}{\partial x_k} \tag{3.7}$$

with μ the liquid dynamic viscosity and δ_{ij} Kronecker symbol.
Since the liquids of interest are incompressible, the second term on the right-hand side is equal to nil following Equation 3.3 and yields to:

$$\tau_{ij} = \mu\left(\frac{\partial u_i}{\partial x_j} + \frac{\partial u_j}{\partial x_i}\right) \tag{3.8}$$

Finally, Equation 3.5 in vectorial notations becomes:

$$\rho\left(\frac{\partial \boldsymbol{u}}{\partial t} + (\boldsymbol{u}.\nabla)\boldsymbol{u}\right) = -\nabla p + \nabla.\mu(\nabla\boldsymbol{u} + (\nabla\boldsymbol{u})^T) + \rho\boldsymbol{g} \tag{3.9}$$

and in Einstein notations:

$$\rho_0\left(\frac{\partial u_i}{\partial t} + u_j\frac{\partial u_i}{\partial x_j}\right) = -\frac{\partial p}{\partial x_i} + \frac{\partial}{\partial x_i}\left(\mu\left(\frac{\partial u_i}{\partial x_j} + \frac{\partial u_j}{\partial x_i}\right)\right) + \rho g_i \tag{3.10}$$

3.1.2.1 Boussinesq approximation

If the variations of density can be neglected compared to the density then the latter can be written as:

$$\rho = \rho_0 + \Delta\rho \tag{3.11}$$

where ρ_0 represents a reference density and $\Delta\rho$ the small variation of density such as $\frac{\Delta\rho}{\rho_0} << 1$.

With the Boussinesq approximation [52], it is assumed that when the varia-

tions of density are negligible compared to the reference density, then they only play a role in the buoyancy term $\rho \boldsymbol{g}$ in the momentum equation. Besides, the dynamic viscosity μ is assumed to be constant for these small variations of density. As a result, the following momentum equation can be derived from Equation 3.9:

$$\rho_0 \left(\frac{\partial \boldsymbol{u}}{\partial t} + (\boldsymbol{u}.\nabla)\boldsymbol{u} \right) = -\nabla p + \mu \nabla^2 \boldsymbol{u} + \rho \boldsymbol{g} \tag{3.12}$$

and in Einstein's notations, it reads:

$$\rho \left(\frac{\partial u_i}{\partial t} + u_j \frac{\partial u_i}{\partial x_j} \right) = -\frac{\partial p}{\partial x_i} + \mu \frac{\partial^2 u_i}{\partial {x_i}^2} + \rho g_i \tag{3.13}$$

ρ_k is defined such as $\rho_k = \frac{\rho}{\rho_0}$. Since the kinematic viscosity ν is such as $\nu = \frac{\mu}{\rho}$, dividing equation 3.12 by ρ_0 leads to:

$$\frac{\partial \boldsymbol{u}}{\partial t} + (\boldsymbol{u}.\nabla)\boldsymbol{u} = -\frac{\nabla p}{\rho_0} + \nu \nabla^2 \boldsymbol{u} + \rho_k \boldsymbol{g} \tag{3.14}$$

3.1.2.2 Linear approximation

In the case where density only depends on temperature, the following Taylor's expansion can be written to express the density of a liquid at a temperature close to T_0:

$$\rho_{(T)} = \rho_0 + \frac{\partial \rho}{\partial T}(T - T_0) + o(T - T_0) \tag{3.15}$$

where $\rho_{(T_0)} = \rho_0$.

Introducing the thermal expansion coefficient β_T such as:

$$\beta_T = -\frac{1}{\rho_0} \frac{\partial \rho}{\partial T} \tag{3.16}$$

and considering only the terms of first order, Equation 3.15 becomes:

$$\rho_{(T)} = \rho_0 (1 - \beta_T (T - T_0)) \tag{3.17}$$

This formulation has the advantage to explicitely show the linear dependency of density on temperature. Also, since for most of the liquids, including the ones considered in this thesis, the thermal coefficient expansion β_T as defined in Equation 3.16 is positive, then Equation 3.16 demonstrates that the higher the temperature, the lower the density. The momentum equation (3.12) can then be expressed as:

$$\rho_0\left(\frac{\partial \boldsymbol{u}}{\partial t} + (\boldsymbol{u}.\nabla)\boldsymbol{u}\right) = -\nabla p + \mu\nabla^2\boldsymbol{u} + [1 - \beta_T(T - T_0)]\rho_0\boldsymbol{g} \tag{3.18}$$

Moreover, for binary mixtures made of a component in excess, the solvent, and a component in considerably smaller amount, the solute, the density depends both on their temperature and composition. As a result, the densities of these liquids depend both on their temperature and composition. When the variations of temperature and solutal concentration are small, then the same reasoning as above can be applied and the following Taylor expansion can be obtained for the density near the temperature T_0 and concentration C_0 and where $\rho_{(T_0,C_0)} = \rho_0$:

$$\rho_{(T,C)} = \rho_{T_0,C_0} + \frac{\partial\rho}{\partial T}(T - T_0) + \frac{\partial\rho}{\partial C}(C - C_0) + o((T - T_0), (C - C_0)) \tag{3.19}$$

where T is the temperature and C the solutal concentration.
The solutal expansion coefficient β_C is defined as:

$$\beta_C = \frac{1}{\rho_0}\frac{\partial\rho}{\partial C} \tag{3.20}$$

Unlike the thermal expansion coefficient in Equation 3.16, the right-hand side is not multiplied by -1 because the solutes considered in this thesis are always denser than the solvent. As a result, the more concentrated in solute the solution is, the denser the liquid and both β_T and β_C are positive in this thesis. Moreover, variations of solutal concentration and temperature have opposing effects: while a growing temperature will cause the density to decrease, a growing concentration

in solute will make the liquid denser. Considering once again the terms of first order only, the density expressed in Equation 3.19 can be written such as:

$$\rho_{(T,C)} = \rho_0(1 - \beta_T(T - T_0) + \beta_C(C - C_0)) \tag{3.21}$$

and the momentum equation can be derived from Equation 3.12:

$$\rho_0\left(\frac{\partial \boldsymbol{u}}{\partial t} + (\boldsymbol{u}.\nabla)\boldsymbol{u}\right) = -\nabla p + \mu\nabla^2\boldsymbol{u} + [1 - \beta_T(T - T_0) + \beta_C(C - C_0)]\rho_0\boldsymbol{g} \tag{3.22}$$

The linear approximation of density can also be extended to multicomponent mixtures in which n species have been diluted in relatively small quantities in a solvent. In this case, following the previous reasonings, the density can be expressed as follows:

$$\rho_{(T,C_i)} = \rho_0(1 - \beta_T(T - T_0) + \sum_{k=1}^{n} \beta_{C_i}(C_i - C_{i_0})) \tag{3.23}$$

where β_{C_i} is the solutal expansion coefficient for species i, C_i and C_{i_0}, respectively, the concentration and reference concentration in species i.

3.1.3 Temperature/Energy equation

Heat transfer is governed by the internal energy equation obtained after deriving the energy balance. The internal energy equation for an incompressible flow can be written as follows:

$$\rho c_p\left(\frac{\partial T}{\partial t} + (\boldsymbol{u}.\nabla)T\right) = \nabla.(\lambda\nabla T) + \chi + S_i \tag{3.24}$$

where c_p is the specific heat capacity, λ the conductivity, χ the dissipation function accounting for the effect of the viscous forces and S_i is an energy source term.

By neglecting the variation of conductivity over the small variations of tempera-

ture as well as the effects of the viscous forces, and, in the absence of any energy source, Equation 3.24 becomes:

$$\frac{\partial T}{\partial t} + (\boldsymbol{u}.\nabla)T = \alpha\nabla^2 T \tag{3.25}$$

with α, the thermal diffusivity defined as $\alpha = \frac{\lambda}{\rho c_p}$.
In heat transfer studies, the Prandtl number Pr is commonly used to characterise the flow. This dimensionless parameter, defined as the ratio of the momentum diffusivity to the thermal diffusivity, can then be written as:

$$Pr = \frac{\nu}{\alpha} \tag{3.26}$$

Equation 3.25 can then be reformulated:

$$\frac{\partial T}{\partial t} + (\boldsymbol{u}.\nabla)T = \frac{\nu}{Pr}\nabla^2 T \tag{3.27}$$

As a conclusion, the energy equation for an incompressible flow can be reduced to the temperature transport equation when the effects of the viscous forces can be neglected and in the absence of any energy source.

3.1.4 Concentration equation

The transport equation for a general variable ϕ can be written as:

$$\frac{\partial \phi}{\partial t} + (\boldsymbol{u}.\nabla)\phi = \nabla.(\lambda_\phi \nabla\phi) \tag{3.28}$$

where λ_ϕ is the diffusivity of the scalar ϕ.
The equation governing the transport of concentration can then be written as:

$$\frac{\partial C}{\partial t} + (\boldsymbol{u}.\nabla)C = \nabla.(D\nabla C) \tag{3.29}$$

where D is the solutal diffusivity which is assumed to be constant over the small variations of temperature. Equation 3.29 can then be written as:

$$\frac{\partial C}{\partial t} + (\boldsymbol{u}.\nabla)C = D\nabla^2 C \tag{3.30}$$

The equation governing the transport of concentration is similar to the previous temperature equation defined in Equation 3.27 [53]. Besides, similarly to the Prandtl number in heat transfer, the Schmidt number is a dimensionless parameter defined as the ratio of the momentum diffusivity to the mass diffusivity. It is written as:

$$Sc = \frac{\nu}{D} \tag{3.31}$$

Finally, Equation 3.30 can be reformulated as:

$$\frac{\partial C}{\partial t} + (\boldsymbol{u}.\nabla)C = \frac{\nu}{Sc}\nabla^2 C \tag{3.32}$$

3.1.4.1 Diffusion coefficient

Wilke and Chang [54] defined an empirical relation based on the Stokes-Einstein equation to calculate the diffusion coefficient of a solute a in a solvent b. This relation can be written as:

$$D_{ab} = 7.4 * 10^{-15} \frac{(\psi_b M_b)^{1/2} T}{\mu_b V_a^{0.6}} \tag{3.33}$$

with D_{ab} the diffusion coefficient in $\mathrm{m^2 \cdot s^{-1}}$, M_b the molecular weight of the solvent in $\mathrm{g \cdot mol^{-1}}$, T the temperature in K, μ_b the viscosity of the solvent in Pa·s and V_a the molar volume of solute at normal boiling point in $\mathrm{cm^3 \cdot g^{-1} \cdot mol^{-1}}$.
ψ_b the association parameter is a constant equal to 2.6 if the solvent is water or 1 for nonassociated solvents.

According to Wilke and Chang [54], the method can predict the diffusion coefficient with less than 10% error. As a result, in this thesis, the mass diffusion

coefficients will be calculated from Equation 3.33.

3.1.4.2 Dufour and Soret effects

Following Hurle and Jakeman's [55] observations, Dufour effects which correspond to the transport of temperature resulting from concentration gradients can be neglected in liquids. Similarly, the transport of concentrations resulting from temperature gradients (Soret effects) is several orders of magnitude lower than the Fick's law. As a result, these transports are neglected in the current thesis.

3.2 Turbulence modelling

Turbulence is frequently observed in engineering applications. As a consequence, numerous studies have been conducted in order to understand its effects but also to simulate it realistically. In CFD, there are three main families of methods available to model turbulence:

- Reynolds-Averaged Navier-Stokes (RANS) turbulent models: The fluid properties such as pressure and velocity are decomposed in the sum of a mean quantity and a fluctuating component. Navier-Stokes equations are time-averaged and an additionnal term appears in the equations due to the influence of the turbulence on the mean flow. Modelling this extra term is the main challenge of RANS methods. The advantage of simulating turbulent flows with RANS methods is that it requires less computational power for reasonably accurate results.
- Large Eddy Simulations (LES): This approach consists in space-filtering the Navier-Stokes equations with a low-pass filter. Large eddies are resolved while the smallest are modelled using sub-grid scale models.
- Direct Numerical Simulations (DNS): With this method, unsteady Navier-Stokes equations are solved for all scales provided that the mesh grid is

sufficiently fine as well as the time steps sufficiently small to catch the smallest eddies and the fastest fluctuations. However, this method is very demanding in terms of computational power.

Alike the Reynolds number in forced convection, the Grashof number indicates the presence of turbulence in natural convection. Indeed, the flow on a vertical plate becomes fully turbulent, when the Grashof number becomes greater than the critical value of 10^9 [56]. For a typical heat flux of 10 $\mathrm{W{\cdot}m^{-2}}$ through the walls of the LNG tanks, the modified Grashof number which is expressed as $Gr^* = \frac{\beta_T g g L^4}{\nu^2}$ is already of the order of 10^{13} when the liquid is 1-meter high. This implies that turbulence plays a significant role in the dynamics of the liquid and has to be modelled.

Among the different turbulent modelling approaches, given the large dimensions of the tanks — dozens of meters for LNG tanks — and the large time scale of the rollover phenomenon — from several hours to several days — the Reynolds-Averaged Navier-Stokes approach was selected. Indeed, even though less accurate than LES or DNS methods, it is significantly less computationaly expensive and makes it possible to model the turbulence for rollovers.

3.2.1 RANS turbulence modelling

As stated before, RANS method consists in time-averaging the Navier-Stokes equations. The physical properties are decomposed as the sum of a mean quantity and a fluctuating one [57]. As a result, the velocity vector $\boldsymbol{u}$ is decomposed as:

$$\boldsymbol{u} = \boldsymbol{U} + \boldsymbol{u'} \tag{3.34}$$

such as $\overline{\boldsymbol{u}} = \boldsymbol{U}$ and $\overline{\boldsymbol{u'}} = \boldsymbol{0}$ and its coordinates u_i for i=1,2 and 3:

$$u_i = U_i + u'_i \tag{3.35}$$

Any physical property defined by a scalar, such as pressure, temperature or concentration, can be defined as:

$$\phi = \Phi + \phi' \tag{3.36}$$

where ϕ is a scalar quantity, Φ its average quantity and ϕ' its fluctuating quantity.

By inserting the decomposed velocities and properties in the Navier-Stokes equations defined in Equation 3.13, it yields to the RANS equations for a incompressible flow under Boussinesq approximation.

The continuity equation for the mean flow becomes:

$$\frac{\partial U_i}{\partial x_i} = 0 \tag{3.37}$$

and the momentum equation for i=1,2 or 3.

$$\rho_0\left(\frac{\partial U_i}{\partial t} + U_j\frac{\partial U_i}{\partial x_j}\right) = -\frac{\partial \overline{p}}{\partial x_i} + \frac{\partial}{\partial x_i}\left(\mu\frac{\partial U_i}{\partial x_i} - \rho_0\overline{u_i' u_j'}\right) + \overline{\rho} g_i \tag{3.38}$$

It can be noticed that Equation 3.38 is similar to the Navier-Stokes equations but includes an extra term $\rho_0\overline{u_i' u_j'}$ which is known as Reynolds stresses and accounts for the fluctuations resulting from the turbulent flow.

3.2.2 Boussinesq assumption

In 1877, Boussinesq suggested that the Reynolds stresses could be formulated as:

$$-\rho_0\overline{u_i' u_j'} = \mu_t\left(\frac{\partial U_i}{\partial x_j} + \frac{\partial U_j}{\partial x_i}\right) - \frac{2}{3}k\rho_0\delta_{ij} \tag{3.39}$$

where k is the turbulent kinetic energy and is defined as $k = \frac{1}{2}(\overline{u_i'\, u_i'})$.

The first term on the right-hand side is similar to the expression of the viscous tensor in Equation 3.8. By analogy, the Reynolds stresses are then identified by

τ_{ij}^t, where $\bar{\bar{\tau}}^t$ is the stress tensor accounting for the effects of turbulence. As a result, the momentum equation can then be written in Einstein's notation as:

$$\rho_0\left(\frac{\partial U_i}{\partial t} + U_j\frac{\partial U_i}{\partial x_j}\right) = -\frac{\partial \bar{p}}{\partial x_i} + \frac{\partial}{\partial x_i}(\tau_{ij} + \tau_{ij}^t) + \overline{\rho} g_i \tag{3.40}$$

or in its vectorial form:

$$\rho_0\left(\frac{\partial \boldsymbol{U}}{\partial t} + (\boldsymbol{U}.\nabla)\boldsymbol{U}\right) = -\nabla\bar{p} + \nabla.(\bar{\bar{\boldsymbol{\tau}}} + \bar{\bar{\boldsymbol{\tau}}}^{\boldsymbol{t}}) + \overline{\rho}\boldsymbol{g} \tag{3.41}$$

This equation has the advantage to show the different contributions of the various forces applied on the fluid. Indeed, the first term on the right-hand side accounts for the effects of pressure gradients on the flow, the second for the action of stresses both viscous and turbulent and the last term for the effects of buoyancy. By dividing the equation by ρ_0, the following equation is obtained:

$$\frac{\partial \boldsymbol{U}}{\partial t} + (\boldsymbol{U}.\nabla)\boldsymbol{U} = -\frac{\nabla\bar{p}}{\rho_0} + \frac{\nabla.(\bar{\bar{\boldsymbol{\tau}}} + \bar{\bar{\boldsymbol{\tau}}}^{\boldsymbol{t}})}{\rho_0} + \overline{\rho_k}\boldsymbol{g} \tag{3.42}$$

3.2.3 Standard Gradient Diffusion Hypothesis (SGDH)

Similarly to the time-averaged momentum equation, the time-averaged transport equation for the scalar quantity ϕ can be written as follows:

$$\frac{\partial \Phi}{\partial t} + U_i\frac{\partial \Phi}{\partial x_i} = \frac{\partial}{\partial x_i}\left(\lambda\frac{\partial \Phi}{\partial x_i} - \overline{u_i'\phi'}\right) \tag{3.43}$$

where the extra term $\overline{u_i'\phi'}$ accounts for the effects of turbulence on the transport of ϕ.

The Standard Gradient Diffusion Hypothesis (SGDH) consists in assuming that the turbulent transport of a scalar quantity is proportional to the gradient of the

mean value of this same quantity. It can be expressed as:

$$\overline{u_i'\phi'} = -\frac{\nu_t}{\sigma_t}\frac{\partial \Phi}{\partial x_i} \tag{3.44}$$

where σ_t is a dimensionless parameter which is respectively the turbulent Prandtl number or turbulent Schmidt number when ϕ is the temperature or the concentration.

As a result, after applying the SGDH, the time-averaged temperature and concentration equations become:

$$\frac{\partial \bar{T}}{\partial t} + (\boldsymbol{U}.\nabla)\bar{T} = \nabla.(\alpha_{eff}\nabla\bar{T}) \tag{3.45}$$

with $\alpha_{eff} = \frac{\nu}{Pr} + \frac{\nu_t}{Pr_t}$, α_{eff} being the effective thermal diffusivity and

$$\frac{\partial \bar{C}}{\partial t} + (\boldsymbol{U}.\nabla)\bar{C} = \nabla.(D_{eff}\nabla\bar{C}) \tag{3.46}$$

with $D_{eff} = \frac{\nu}{Sc} + \frac{\nu_t}{Sc_t}$, D_{eff} being the effective mass diffusivity.

For the sake of simplicity, the bars above the temperature and the concentration, will be dropped hereafter.

3.2.4 Turbulence near the walls

The boundary layer near a smooth wall is composed of three distinct regions. These different areas are illustrated in Figure 3.1 where the dimensionless velocity profile parallel to the wall u^+ in red in Figure 3.1, is expressed as a function of the dimensionless distance from the wall y^+. u^+ and y^+ are defined as:

$$u^+ = \frac{u}{u_\tau}, y^+ = \frac{y u_\tau}{\nu} \tag{3.47}$$

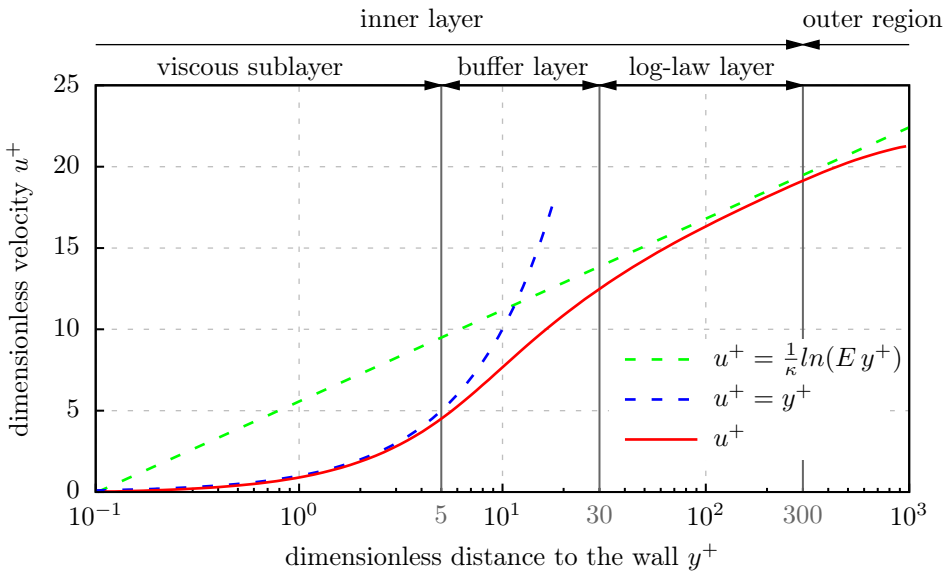

Figure 3.1: Dimensionless velocity profile parallel to the wall in the near-wall area

with u_τ the friction velocity which can be expressed as a function of the wall shear stress τ_{wall} as :

$$u_\tau = \sqrt{\frac{\tau_{wall}}{\rho}} \tag{3.48}$$

The three areas are:

- the viscous sub-layer, for values of y^+ lower than 5 and where the viscous effects dominate. In this zone, the velocity coordinate in the direction parallel to the wall u^+ verifies:

$$u^+ = y^+ \tag{3.49}$$

- the buffer layer, where y^+ is between 5 and 300 which is the transition located between the viscous and the log-law layers. There is no known relation in this area linking the dimensionless velocity u^+ to the dimensionless distance y^+.
- the log-law layer, for values of y^+ between 30 and 300. In this area, the

turbulent effects dominate and u^+ verifies:

$$u^+ = \frac{1}{\kappa}\ln(Ey^+) \tag{3.50}$$

with κ the Von Karman constant and E the wall roughness parameter, respectively equal to 0.41 and 9.8 for smooth walls [58].

In order to model the turbulence in the near-wall area, there are two existing methods. The first one, the high-Reynolds approach, consists in using wall functions to model the flow in the vicinity of the walls. As a consequence, it only requires the first cell to be located in the log-law layer which speeds up the simulations significantly by using relatively coarse meshes near the walls. The second one, the low-Reynolds approach, consists in simulating the flow in the viscous sublayer which requires a very fine grid near the wall. More accurate, it also require higher computational power.

Both methods are used in this thesis. To simulate small-scale experiments, the low-Reynolds approach was selected to improve the results accuracy. However, the second method was chosen to simulate the liquid flow within large containers and over long periods of time.

3.2.5 Standard k-ϵ model

The standard k-ϵ model, initially developed by Jones and Launder [59], is now the most widely used turbulent model. Assuming the SGDH, it is based on the two following transport equations:

$$\frac{\partial k}{\partial t} + U_j\frac{\partial k}{\partial x_j} = \frac{\partial}{\partial x_j}\left[\left(\nu + \frac{\nu_t}{\sigma_k}\right)\frac{\partial k}{\partial x_j}\right] + P_k - \epsilon \tag{3.51}$$

$$\frac{\partial \epsilon}{\partial t} + U_j\frac{\partial \epsilon}{\partial x_j} = \frac{\partial}{\partial x_j}\left[\left(\nu + \frac{\nu_t}{\sigma_\epsilon}\right)\frac{\partial \epsilon}{\partial x_j}\right] + (c_{1\epsilon}P_k - c_{2\epsilon}\epsilon)\frac{\epsilon}{k} \tag{3.52}$$

Equations 3.51 and 3.52, respectively, model the transport of the turbulent kinetic energy k and the transport of the rate of dissipation of the turbulent kinetic energy ϵ. c_μ, σ_k, σ_ϵ, $c_{1\epsilon}$, $c_{2\epsilon}$ are adjustable constants. However, default values selected from a wide range of applications are usually accepted and are as follows:

$$c_\mu = 0.09 \quad \sigma_k = 1.00 \quad \sigma_\epsilon = 1.30 \quad c_{1\epsilon} = 1.44 \quad c_{2\epsilon} = 1.92 \tag{3.53}$$

ν_t, the turbulent kinematic viscosity, is defined as:

$$\nu_t = c_\mu \frac{k^2}{\epsilon} \tag{3.54}$$

P_k, involved in Equations 3.51 and 3.52, accounts for the generation of turbulent kinetic energy due to the interaction of the Reynolds stresses and the mean velocity gradient. P_k is defined as:

$$P_k = -\overline{u_j' u_l'} \frac{\partial U_j}{\partial x_l} \tag{3.55}$$

Finally, under the Boussinesq assumption, Equation 3.55 becomes:

$$P_k = \nu_t \left[\left(\frac{\partial U_j}{\partial x_l} + \frac{\partial U_l}{\partial x_j} \right) - \frac{2}{3} \delta_{jl} k \right] \frac{\partial U_j}{\partial x_l} \tag{3.56}$$

3.2.6 Inclusion of buoyancy in the standard $k - \epsilon$ model

The turbulent model used in this thesis is the standard k-ϵ model with an extra term P_b accounting for the effects of buoyancy on the turbulence. The approach adopted regarding this extra term is similar to the one used by Henkes [60] but the novelty is that instead of being restricted to natural convection cases, it extends the applications to double-diffusive convections. The k-ϵ equations

used in this study are as follows:

$$\frac{\partial k}{\partial t} + U_j \frac{\partial k}{\partial x_j} = \frac{\partial}{\partial x_j}\left[\left(\nu + \frac{\nu_t}{\sigma_k}\right)\frac{\partial k}{\partial x_j}\right] + P_k + P_b - \epsilon \tag{3.57}$$

$$\frac{\partial \epsilon}{\partial t} + U_j \frac{\partial \epsilon}{\partial x_j} = \frac{\partial}{\partial x_j}\left[\left(\nu + \frac{\nu_t}{\sigma_\epsilon}\right)\frac{\partial \epsilon}{\partial x_j}\right] + [c_{1\epsilon}(P_k + c_{3\epsilon}P_b) - c_{2\epsilon}\epsilon]\frac{\epsilon}{k} \tag{3.58}$$

P_b, the extra term, represents the generation of turbulence due to buoyancy and can be written as:

$$P_b = \overline{u'_j \rho'_k} g_j \tag{3.59}$$

Taking into account the SGDH, defined in Section 3.2.3, it becomes:

$$P_b = -g_j \frac{\nu_t}{\sigma_{\rho_k}} \frac{\partial \bar{\rho}_k}{\partial x_j} \tag{3.60}$$

In the particular case where the density can be defined as:

$$\rho = \rho_0(1 - \beta_T(T - T_0)) \tag{3.61}$$

the expression for P_b is the same as the one used by Henkes [60]:

$$P_b = g_j \beta_T \frac{\nu_t}{\sigma_T} \frac{\partial T}{\partial x_j} \tag{3.62}$$

with $\sigma_{\rho_k} = \sigma_T$.

From Equation 3.60, one can notice that when the stratification is stable i.e. when $\frac{\partial \rho}{\partial z} > 0$, since $g_z = -g$ then the term P_b is negative, and, consequently, promotes the turbulence suppression. On the contrary, in the case of unstable stratification, the term P_b is positive and promotes the turbulence in the liquid. Rodi [61] noticed that the buoyancy term contributes to the dissipation of the turbulent kinetic energy along vertical layers where $c_{3\epsilon}$ should be equal to 1. On the opposite, the buoyancy term has no effect on the dissipation along horizontal layers where it should be close to nil. The following expression suggested by

Henkes [60] for $c_{3\epsilon}$ and which respects both limits suggested by Rodi has been adopted in this thesis:

$$c_{3\epsilon} = \tanh\left|\frac{V}{U}\right| \tag{3.63}$$

with V the velocity component in the direction of the gravity and U the velocity component perpendicular to the gravity vector.

3.2.7 Launder-Sharma k-ϵ model and inclusion of buoyancy

The Launder-Sharma k-ϵ is a low-Reynolds method developed by Launder and Sharma [62]. Unlike the standard k-ϵ presented in Section 3.2.5, the flow is also solved within the boundary layers. The equations for the transport of kinetic energy and turbulent dissipation energy are as follows:

$$\frac{\partial k}{\partial t} + U_j\frac{\partial k}{\partial x_j} = \frac{\partial}{\partial x_j}\left[\left(\nu + \frac{\nu_t}{\sigma_k}\right)\frac{\partial k}{\partial x_j}\right] + P_k - \epsilon - D \tag{3.64}$$

$$\frac{\partial \epsilon}{\partial t} + U_j\frac{\partial \epsilon}{\partial x_j} = \frac{\partial}{\partial x_j}\left[\left(\nu + \frac{\nu_t}{\sigma_\epsilon}\right)\frac{\partial \epsilon}{\partial x_j}\right] + (c_{1\epsilon}P_k - c_{2\epsilon}f_2\epsilon)\frac{\epsilon}{k} + E \tag{3.65}$$

where ν_t is calculated such as $\nu_t = C_\mu f_\mu \frac{k^2}{\epsilon}$.
D, E are extra source terms such as $D = 2\nu(\frac{\partial\sqrt{k}}{\partial y})$, $E = 2\nu\nu_t(\frac{\partial^2 \boldsymbol{U}}{\partial y^2})$. f_μ and f_2 are damping functions defined as $f_\mu = \exp\left(-\frac{3.4}{(1+\frac{Re_t}{50})^2}\right)$ and $f_2 = 1 - 0.3\exp(-Re_t^2)$ with Re_t, the turbulent Reynolds number, expressed as $Re_t = \frac{k^2}{\nu\epsilon}$.

Similarly to Section 3.2.6, the effects of buoyancy can be included in the Launder-Sharma k-ϵ. The equations can then be written as:

$$\frac{\partial k}{\partial t} + U_j\frac{\partial k}{\partial x_j} = \frac{\partial}{\partial x_j}\left[\left(\nu + \frac{\nu_t}{\sigma_k}\right)\frac{\partial k}{\partial x_j}\right] + P_k + P_b - \epsilon - D \tag{3.66}$$

$$\frac{\partial \epsilon}{\partial t} + U_j\frac{\partial \epsilon}{\partial x_j} = \frac{\partial}{\partial x_j}\left[\left(\nu + \frac{\nu_t}{\sigma_\epsilon}\right)\frac{\partial \epsilon}{\partial x_j}\right] + (c_{1\epsilon}(P_k + P_b) - c_{2\epsilon}f_2\epsilon)\frac{\epsilon}{k} + E \tag{3.67}$$

with P_b and $c_{3\epsilon}$ defined such as in Equations 3.60 and 3.63.

3.2.8 Limitations of the k-ϵ model and the SGDH assumption

The turbulent model used in this thesis has its limitations. Indeed, the standard k-ϵ, on which it is based, is known to perform poorly for flows with adverse pressure gradients, separation or recirculating regions [57].

Besides, the simulations of rollovers are very sensitive to the modelling of the turbulence near the interface separating the layers and more specifically the generated mixing. While overpredicting the mixing would accelerate the rollover occurrence, underpredicting the mixing would delay it. As far as the horizontally stably-stratified flows are concerned, Viollet [63] has shown relatively good agreements between the experiments and and his numerical results using the $k-\epsilon$ model which includes buoyancy terms expressed with the SGDH and similar to the one developed in this thesis.

However, given that McGuirk and Papadimitriou [64] noticed that the same model overpredicted significantly the mixing rate of a stably stratified flow, Launder [65] stated that the performance of the turbulent model is case dependent. Besides, regarding the modelling of the effect of buoyancy on the turbulence, Launder observed [65] that the expression of P_b employing the SGDH, as defined in Equation 3.60, tends to underestimate them for buoyant flows rising vertically. Significant improvements could be obtained using the Generalized Gradient Diffusion Hypothesis [66]. The latter, which considers the fluid anisotropy, links the turbulent transport of a scalar quantity $u_i'\phi'$ to the gradient of the mean value of the same quantity as follows:

$$\overline{u_i'\phi'} = -c_\phi \frac{\overline{u_j'u_i'}}{\epsilon} k \frac{\partial \Phi}{\partial x_j} \tag{3.68}$$

where c_ϕ is a constant approximately equal to 0.3.

Hence, following Equations 3.68 and 3.59, P_b the buoyant term would be ex-

pressed as:

$$P_b = -g_j c_\rho \frac{\overline{u_j' u_i'}}{\epsilon} k \frac{\partial \bar{\rho}_k}{\partial x_j} \tag{3.69}$$

Further improvements could be obtained by using more complex turbulent models such as Reynolds Stress equations Models (RSM) which calculate the transport of the Reynolds stresses.

Despite its known shortcomings and given the satisfying results obtained by Viollet [63], the k-ϵ approach including extra terms to take into account the buoyancy is used in this thesis to model the turbulence inside the LNG tank.

3.3 Evaporation modelling

There is usually no boiling in LNG storage tanks [33] since the heat fluxes coming in the tank as a result of heat losses are several orders of magnitude lower than the minimum heat flux required to enable boiling [21].
As presented in Section 2.5, Hashemi-Wesson [33] established a relation between the supersaturated temperature and the evaporation rate as follows:

$$\dot{m} = C_m \frac{\lambda}{L} \left(\frac{\beta_T g}{\alpha \nu} \right)^{1/3} \Delta T^{4/3} \tag{3.70}$$

This relation, validated by Doyer et al. [34], and commonly used in the LNG sector, has the advantage to focus the study on the liquid phase only. Lemembre [16], followed by Khelifi-Touhaimi [67], used a local adaptation of Hashemi-Wesson relation assuming that the evaporation is controlled by a thin layer below the free surface. As a result, the supersaturated temperature is the difference between the temperature of a layer located below the free surface and equal to $1/100^{\text{th}}$ of the total height and the temperature of the free surface assumed to be equal to the saturation temperature. However, the size was chosen arbitrarily and this adapted version of Hashemi-Wesson relation, unlike the standard version, has not been experimentally validated. For these reasons, in the present study, it is

the original Hashemi-Wesson relation which has been used. The supersaturated temperature considered is the difference between the average temperature in the stratum and the temperature at the free surface which has been observed to be close to the saturation temperature [33].

The evaporative heat flux can be derived from Equation 3.70 by multiplying the evaporation rate by the latent heat L as follows:

$$q_{ev} = \dot{m}L \tag{3.71}$$

Besides, when the saturation temperature is greater than the bulk temperature, there is no superheat, and, as a consequence, no resulting evaporation. Hence, in this case, the surface will be considered adiabatic. On the opposite, when the temperature in the bulk becomes greater than the saturation temperature, then the evaporative flux is calculated using Hashemi-Wesson relation. The evaporative flux is then calculated as:

$$q_{ev} = \begin{cases} 0, & \text{if } T_{bulk} < T_{sat} \\ C_m \, \lambda \left(\frac{\beta_T g}{\alpha \nu} \right)^{1/3} \Delta T^{4/3}, & \text{if } T_{bulk} \geq T_{sat} \end{cases} \tag{3.72}$$

where C_m is equal to 0.328 for LNG. Cleggs and Papadakis [35] have proved that this relation is also valid to study the evaporation of Freon provided that C_m equals 0.27.

The heat at the liquid/vapour interface is transferred by conduction and micro-convection [21]. Fourier's law at this interface gives:

$$\boldsymbol{q_{ev}} = -(\lambda + \lambda_{turb}) \nabla T = -\lambda_{eff} \nabla T \tag{3.73}$$

As a consequence, the following boundary condition can be derived for the tem-

perature at the free surface.

$$\nabla T.\boldsymbol{n} = \frac{q_{ev}}{\lambda_{eff}} \tag{3.74}$$

where $\lambda_{eff} = \lambda + \lambda_{turb}$.

Standard boil-off rates within onshore LNG tanks are usually less than 0.05% of the total tank content per day but it can vary between 0.02 and 0.1% [68]. Besides, even following rollovers, the height of the liquid is not significantly affected. For instance, during La Spezia incident, 185 tons of LNG vapour were released before and following the rollover occurence. This amount corresponds approximatively to 0.8% of the 23,400 tons initially contained and the height of the liquid will have decreased of less than 0.2 meter (approximatively 0.1% of the initial liquid height). As a consequence, considering the relatively small variations of volume both in standard operating mode and during rollovers, it is assumed within the frame of this study that the level of liquid is constant despite the evaporation.

Moreover, when dealing with LNG rollovers, the study hereafter is limited to rollovers with negligible amounts of nitrogen which is a reasonable assumption since most of LNG contains less than 1% of nitrogen [20]. The influence of Nitrogen on the evaporation is then limited and Methane, which is dominant in LNG is assumed to be the most volatile component.

Additionally, whether the considered solution is LNG or a mixture of Freon 11/Freon 113 and because of their lower boiling points, the most volatile species are Methane or Freon 11, which are dominant in these two solutions. As a result, it has been decided following Lemembre's idea [16], to model the evaporation of these solvents by the injection of a solute in order to model the densification of the liquid due to the evaporation of the more volatile and less dense solvent. The flux of evaporating solvent through the liquid-vapour interface can be calculated using Fick's law:

$$\boldsymbol{j}_{solvent} = -D_{eff}\nabla C \tag{3.75}$$

where $\boldsymbol{j}$ is the diffusion flux, D the diffusion coefficient and C the mass concentration.

Following Lemembre's idea [16] and as detailed in Appendix A, the equivalent flux of solute entering the liquid can be calculated as:

$$\dot{\boldsymbol{m}}_{solute} = -\left(\frac{C}{\rho - C}\right)\dot{\boldsymbol{m}}_{solvent} \tag{3.76}$$

and in a multicomponent solution as:

$$\dot{\boldsymbol{m}}_{solute_i} = -\dot{\boldsymbol{m}}_{solvent}\left(\frac{C_{solute_i}}{\rho - \sum_k C_{solute_k}}\right) \tag{3.77}$$

Taking into account Equations 3.75 and 3.77, the gradient of concentration of the solute i verifies the following condition at the free surface:

$$\nabla C_{solute_i}.\boldsymbol{n} = -\frac{\dot{\boldsymbol{m}}_{solute_i}.\boldsymbol{n}}{D_{eff_i}} = \frac{\dot{m}_{solvent}}{D_{eff_i}}\left(\frac{C_{solute_i}}{\rho - \sum_k C_{solute_k}}\right) \tag{3.78}$$

Finally, due to turbulence and to the convective motions, the flow is assumed to be quasi-homogeneous at the free surface. As a result, Marangoni effects are neglected at the liquid/vapour interface.

3.4 Boundary conditions

As described above and depicted in Figure 3.2, thanks to the use of Hashemi-Wesson relation, the study of the rollover phenomenon is focused on the liquid phase only. Whether the tank geometry is cylindrical, rectangular or even spherical, the liquid is enclosed between walls located on its sides and below it. At the walls, the velocity is nil and there is no mass tranfer since the walls are impermeable. As a result, velocities and concentrations verify:

$$\boldsymbol{U} = \boldsymbol{0} \tag{3.79}$$

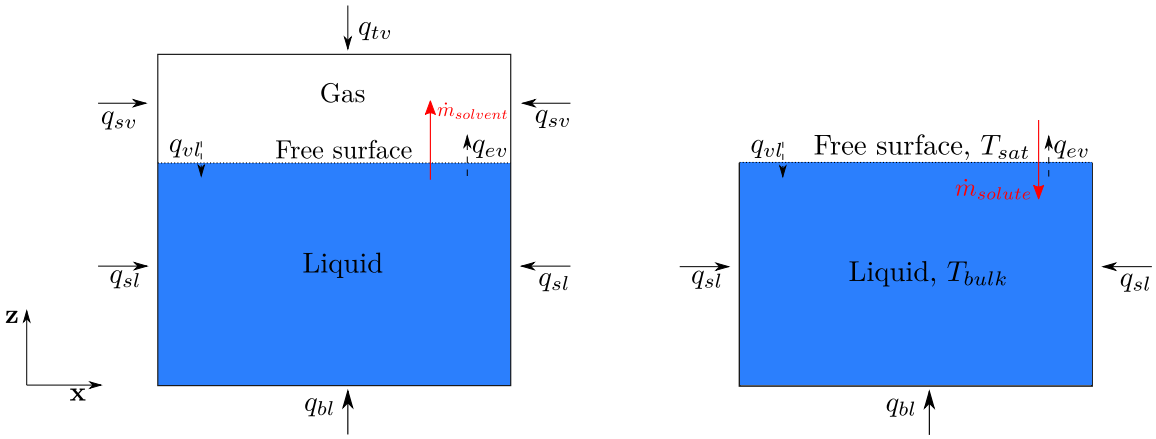

Figure 3.2: Schematic of the flow in a tank (on the left) and simplified model adopted in this study (on the right)

and

$$\nabla C.\boldsymbol{n} = 0 \tag{3.80}$$

where $\boldsymbol{n}$ is the vector normal to the wall surface. Besides, Fourier's law at the walls gives:

$$\nabla T.\boldsymbol{n} = \frac{q_{wall}}{\lambda_{eff}} \tag{3.81}$$

where q_{wall} is the heat flux through the wall.

The surface of the liquid in contact with the vapour is shear-stress free. As a result, the velocity at the surface is defined in the cartesian frame of reference as:

$$\boldsymbol{U}.\boldsymbol{n} = U_z = 0 \tag{3.82}$$

and

$$\frac{\partial U_x}{\partial z} = 0 \quad and \quad \frac{\partial U_y}{\partial z} = 0 \tag{3.83}$$

As described earlier, the evaporation of solvent is modelled by an equivalent entering flux of solute. The boundary condition at the free surface for the concentration is as detailed in the previous section:

$$\nabla C_{solute_i}.\boldsymbol{n} = -\frac{\dot{\boldsymbol{m}}_{solute_i}.\boldsymbol{n}}{D_{eff_i}} = \frac{\dot{m}_{solvent}}{D_{eff_i}}\left(\frac{C_{solute_i}}{\rho - \sum_k C_{solute_k}}\right) \tag{3.84}$$

Finally, the boundary condition for the temperature at the free surface is:

$$\nabla T.\boldsymbol{n} = \frac{q_{ev}}{\lambda_{eff}} \tag{3.85}$$

with q_{ev} calculated from Hashemi-Wesson equation.
When the vapour space promotes the warming of the liquid, the resulting heat flux is defined as:

$$q_{res} = \frac{q_{ev} - q_{vl}}{\lambda_{eff}} \tag{3.86}$$

The boundary conditions selected for the pressure field have not been mentioned in this part but will be explained in the next chapter.

3.5 Summary

In this chapter, several points have been highlighted:

- The equations modelling the physics involved during a rollover event have been presented.
- The turbulent modelling methods combining, RANS model and a low-Reynolds approach, and, RANS model and a high-Reynolds approach, have been selected to model rollovers as an acceptable trade-off between accuracy and simulation time.
- The mixture is assumed to be made of a solvent to which is added one or several solutes in small quantities. As a result, all the thermophysical properties of the mixture except the density are the same as for the solvent and are assumed to be constant over the small variations of temperatures and concentrations.
- The boundary conditions have also been presented.

Chapter 4

Methodology

In this chapter, the adopted numerical method will be presented. First, the discretisation of a scalar equation into a set of linear equations and its solving process will be adressed. Later, the author will present the discretisation process of the more challenging Navier-Stokes equations as well as its solving method via the use of pressure-velocity coupling. Moreover, due to the physics involved during rollovers and as it has been presented in Chapter 3.1, the difficulty arises in the coupling through the buoyancy term, between the Navier-Stokes equations and the transport equations of temperature and concentrations in solute. The global method employed in this thesis to face this particular difficulty will be introduced.

4.1 Finite Volume Method

Mathematicians are still investigating the solution of the non-linear Navier-Stokes equations presented in Section 3.1 and which currently constitutes one of the greatest mathematical challenges of our time.

In order to overcome this limit, Computational Fluid Dynamics (CFD) has been developed over the last few decades to solve numerically the Navier-Stokes equations. These differential equations are first discretised in space but also in

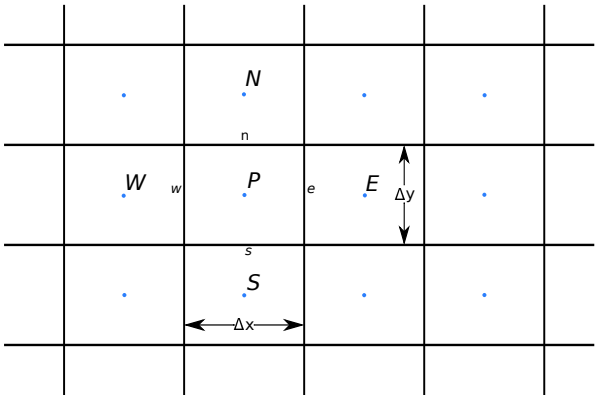

Figure 4.1: Control volumes for a 2D cartesian grid

time for transient simulations and turned into a system of algebraic equations which will be solved iteratively.

Several methods exists in CFD depending on the discretisation process such as the finite element method, the finite difference method and the finite volume method [69][57]. OpenFOAM [70], the software used in the framework of this PhD, is based on the finite volume method which consists in discretising the domain into a finite number of control volumes and where all the variables are stored at the cell centres forming a collocated grid [71]. The simple case of a cartesian 2D grid is illustrated in Figure 4.1. This method has the advantage to ensure the conservation of the considered physical quantities. Indeed, the equations are then integrated over the control volumes and by construction, the flux leaving a control volume is equal to the flux entering the adjacent one. As for the values at the surfaces of the control volumes, they are obtained after interpolating the values at the centroid of the adjacent control volumes.

4.2 Discretisation of the transport equation

As presented in Section 3.1.3, the transport equation for a given turbulent scalar ψ in an incompressible flow can be written as follows:

$$\underbrace{\frac{\partial \psi}{\partial t}}_{Time\,derivative} + \underbrace{\nabla.(\boldsymbol{U}\psi)}_{Convective\,term} = \underbrace{\nabla.(\Gamma\nabla\psi)}_{Diffusive\,term} + \underbrace{S_\psi}_{Source\,term} \tag{4.1}$$

with Γ the effective diffusion coefficient and $\boldsymbol{U}$ the fluid velocity.
It is constituted of four distinct terms: the time derivative, the convective term, the diffusive term and the source term. These four terms will be treated differently during the discretisation process. By integrating Equation 4.1 over a control volume denoted CV, it yields to:

$$\int_{CV} \frac{\partial \psi}{\partial t}\, dv + \int_{CV} \nabla.(\boldsymbol{U}\psi)\, dv = \int_{CV} \nabla.(\Gamma\nabla\psi)\, dv + \int_{CV} S_\psi\, dv \tag{4.2}$$

Regarding the discretisation of the integral form of the transport equation, two theorems, Gauss divergence theorem and the gradient theorem, are used
Gauss divergence theorem states that:

$$\int_{CV} \nabla.\boldsymbol{a}\, dv = \int_A \boldsymbol{n}.\boldsymbol{a}\, ds = \int_A \boldsymbol{a}.\boldsymbol{dS} \tag{4.3}$$

where $\boldsymbol{a}$ is a given vector, A the surface area of the control volume CV, $\boldsymbol{n}$ the normal vector to the surface element dA pointing outwards and $\boldsymbol{dS}$ its associated vector defined such as $\boldsymbol{dS} = \boldsymbol{n}ds$.
As for the gradient theorem, it gives:

$$\int_{CV} \nabla\psi\, dv = \int_A \psi\, \boldsymbol{dS} \tag{4.4}$$

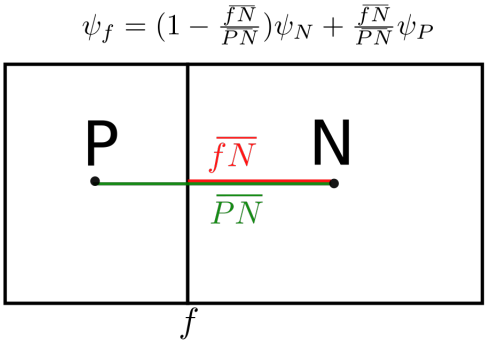

Figure 4.2: Central differencing scheme

where ψ is a given scalar.

Equations 4.3 and 4.4 can then be discretised for a control volume as follows:

$$\int_{CV} \nabla . \boldsymbol{a}\, dv = \int_{A} \boldsymbol{a}.\boldsymbol{dS} \approx \sum_{f} \boldsymbol{S}_f.\boldsymbol{a_f} \tag{4.5}$$

$$\int_{CV} \nabla \psi\, dv = \int_{A} \psi\, \boldsymbol{dS} \approx \sum_{f} \boldsymbol{S}_f \psi_f \tag{4.6}$$

with $\boldsymbol{S}_f = \int_f \boldsymbol{n} ds$, and where $\boldsymbol{a}_f$ and ψ_f are respectively the value of the field $\boldsymbol{a}$ and ψ obtained from face interpolations.

4.2.1 Face interpolations

Face interpolations has a key role in the discretisation process by enabling the calculation of a given field at the boundary between two adjacent cells. It is done by using a given scheme characterised by its order of accuracy which is based on its truncation error. The schemes used in this study are presented hereafter.

4.2.1.1 Central differencing scheme

By using the central differencing (CD) scheme [72], the value of a given scalar ψ at a given face f is calculated after interpolating linearly the values between two neighbouring cell centres as illustrated in Figure 4.2.

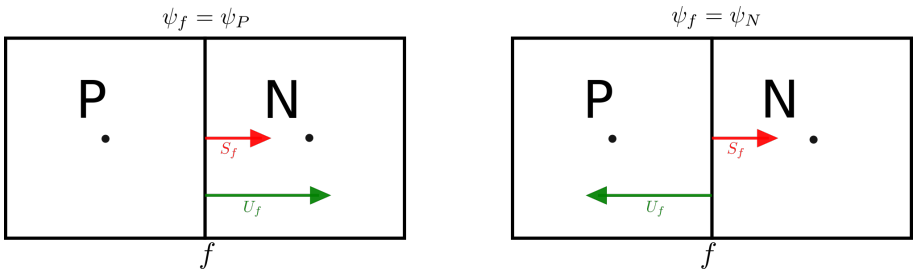

Figure 4.3: Upwind differencing scheme

δ_f defined as:

$$\delta_f = \frac{\overline{fN}}{\overline{PN}} \tag{4.7}$$

is the ratio of the distances between a face f and the cell centre P, and, the face f and the neighbour cell centre N. The interpolated value at the face f can then be expressed as:

$$\psi_f = (1 - \delta_f)\psi_N + \delta_f \psi_P \tag{4.8}$$

The CD scheme is second order accurate but can be unstable and produce non-physical oscillations.

4.2.1.2 Upwind differencing scheme

Unlike the CD scheme, the upwind differencing (UD) scheme takes into account the direction of the flow [72]. The interpolation of a scalar at the surface between two adjacent cells depends on the direction of the flow orientation as observed in Figure 4.3. ψ_f is equal to the value of ψ at the centre of its upstream and adjacent cell centre as follows:

$$\psi_f = \begin{cases} \psi_P, & \text{if } \boldsymbol{S}_f.\boldsymbol{U}_f \geq 0 \\ \psi_N, & \text{if } \boldsymbol{S}_f.\boldsymbol{U}_f < 0 \end{cases} \tag{4.9}$$

The UD scheme is only first order accurate. As a result, it is more stable than the CD scheme but it introduces some numerical diffusions especially with coarse meshes. The linear-upwind differencing scheme (LUD) [73] is similar to the UD

scheme but involves two upstream values which, compared to the UD scheme, improves its accuracy while lowering its numerical diffusivity.

4.2.2 Convective term

The convective term accounts for the transport caused by advection. After applying the gradient theorem, the integrated form of the convective term can be discretised as follows:

$$\int_{CV} \nabla.(\boldsymbol{U}\psi)\, dv = \int_{A} \boldsymbol{n}.(\boldsymbol{U}\psi)\, ds = \sum_{f} \boldsymbol{S}_f.\boldsymbol{U}_f\, \psi_f \approx \sum_{f} F\, \psi_f \tag{4.10}$$

with F the mass flux through the surface f defined as $F = \boldsymbol{S}_f.\boldsymbol{U}_f$

4.2.3 Diffusive term

The diffusive term accounts for the transport caused by the molecular and the turbulent diffusions. It can be discretised as follows:

$$\int_{CV} \nabla.(\Gamma\nabla\psi)\, dv = \int_{A} \Gamma\nabla\psi.\boldsymbol{n}\, ds = \sum_{f} \Gamma_f \boldsymbol{S}_f.\nabla\psi_f \tag{4.11}$$

For an orthogonal space grid, the product $\boldsymbol{S}_f.\nabla\psi_f$ is calculated using the CD scheme which gives:

$$\boldsymbol{S}_f.\nabla\psi_f = |\boldsymbol{S}_f|\frac{\psi_P - \psi_N}{d} \tag{4.12}$$

with ψ_P the value of ψ at the cell centre and ψ_N the value at the neighbouring cell centre. d is the distance between P and N. As far as non-orthogonal space grids are concerned, a correction term must be included [72]. $\boldsymbol{S}_f.\nabla\psi_f$ can then be decomposed into two terms accounting for the orthogonal contribution and the non-orthogonal contribution as follows:

$$\boldsymbol{S}_f.\nabla\psi_f = \underbrace{|\boldsymbol{\Delta}|\frac{\psi_P - \psi_N}{d}}_{orthogonal\, contribution} + \underbrace{\boldsymbol{k}.\nabla\psi_f}_{non-orthogonal\, contribution} \tag{4.13}$$

where $\boldsymbol{\Delta}$ and $\boldsymbol{k}$ are chosen following the over-relaxed method described by Jasak [72], and the face gradient $\nabla\psi_f$ in the non-orthogonal contribution term is calculated by interpolating its value from cell-centred gradient as described hereafter.

4.2.4 Source term

The source term S_ψ can be written under a linear form as:

$$S_\psi = S_p\psi + S_u \tag{4.14}$$

where S_p and S_u are, respectively, the coefficients of the linear part and the constant part of the source term.
The integration of the source term in Equation 4.1 gives:

$$\int_{CV} S_\psi \, dv \approx S_p\psi_P V_p + S_u V_P \tag{4.15}$$

where V_P is the volume of the control volume.

4.2.5 Time discretisation

The time derivative is discretised following Euler implicit method. As a result, the integrated time derivative can be approximated as follows:

$$\int_{CV} \frac{\partial\psi}{\partial t} \, dv \approx \frac{\psi_P^n - \psi_P^0}{\Delta t} V_P \tag{4.16}$$

with ψ_P^n the values of ψ at the cell centre P at the time $t + \Delta t$ and ψ_P^0 the values at the cell centre P at the time t.
By using this method, the integral of ψ_P between t and $t + \Delta t$ gives:

$$\int_t^{t+\Delta t} \psi_P \, dt = \psi_P^n \Delta t \tag{4.17}$$

The main advantage of the Euler implicit method is its robustness since it is unconditionnaly stable [57].
After injecting Equations 4.10, 4.11, 4.15 and 4.16 into Equation 4.2, the following equation can be obtained after integrating over a time step Δt:

$$\int_t^{t+\Delta t} \left[\frac{\psi_P^n - \psi_P^0}{\Delta t} V_P + \sum_f \boldsymbol{S}_f . \boldsymbol{U}_f \, \psi_f \right] dt = \int_t^{t+\Delta t} \left[\sum_f \Gamma_f \boldsymbol{S}_f . \nabla \psi_f + S_p \psi_P V_p + S_u V_P \right] dt \quad (4.18)$$

Finally, after considering Equation 4.17, it yields to:

$$\frac{\psi_P^n - \psi_P^0}{\Delta t} V_P + \sum_f \boldsymbol{S}_f . \boldsymbol{U}_f \, \psi_f^n = \sum_f \Gamma_f \boldsymbol{S}_f . \nabla \psi_f^n + S_p \psi_P^n V_p + S_u V_P \quad (4.19)$$

4.3 Boundary conditions

In order to calculate the different fields at the cell centres, the interpolated value of these fields at the surface between two adjacent cells must be defined. As far as the cells located next to the boundaries are concerned, the fields at the surface of the control volumes located on the boundary are defined by using boundary conditions. Most of the boundary conditions used in CFD are based on the Dirichlet boundary condition or on the Neumann boundary condition.
The Dirichlet boundary condition defines the value of a given field ψ at the boundary, while the Neumann boundary condition defines the flux of this field at the boundary. The value of the field at the surface can then be derived using:

$$\psi_f = \psi_P + d \nabla \psi_f \quad (4.20)$$

where d is the distance between the cell centre and the surface f.

4.4 Solving linear systems

After replacing the value of $\nabla\psi_f^n$ as explained in Section 4.2.3 and by substituting ψ_f^n with its interpolated value, Equation 4.19 can be expressed as:

$$a_P\psi_P^n + \sum_N a_N\psi_N^n = R_P \tag{4.21}$$

Finally, at a given time, the set of linear equations obtained after discretisating the transport equation for all the control volumes constituting the grid can be written in its matrix form as:

$$[A][\psi] = [R] \tag{4.22}$$

where $[A]$ is a sparse matrix (i.e. most of its elements are equal to zero) such as its diagonal coefficients are a_P and its off-diagonal ones a_N. $[\psi]$ is the scalar field and $[R]$ the source vector. The system of linear equations written in Equation 4.22 can be solved following direct methods such as Cramer's rule matrix inversion or Gaussian elimination, or by using iterative methods which are usually preferred to direct methods because significantly less computationally expensive. Among these iterative process, the Conjugate Gradient (CG) method was initially developed by Hestenes and Stiefel [74]. Later, a variant called the "biconjugate gradient method" (bi-CG) was proposed by Van Der Vorst [75] for solving asymmetric matrices with a faster convergence rate. Finally, in order to speed up the convergence rate of these methods, the sparse matrix $[A]$, if symmetric, is preconditioned with the incomplete-Cholesky factorisation [76] or, if asymmetric, after applying the incomplete lower-upper (LU) factorisation.

4.5 Discretisation of the Navier-Stokes equations

Fluid dynamics is governed by the Navier-Stokes equations which, for incompressible liquids subject to buoyancy, can be written as follows:

- the continuity equation:

$$\nabla.\boldsymbol{U} = 0 \tag{4.23}$$

- the momentum equation:

$$\frac{\partial \boldsymbol{U}}{\partial t} + \nabla.(\boldsymbol{U}\boldsymbol{U}) - \nu_{eff}\Delta\boldsymbol{U} = -\frac{\nabla p}{\rho_0} + \rho_k \boldsymbol{g} \tag{4.24}$$

where $\boldsymbol{U}$ and p are the Reynolds-averaged quantities for the velocity and the pressure.

By defining the modified pressure defined as $p_m = \frac{p-\rho g z}{\rho_0}$ where z is the Z-coordinate, the pressure and the buoyancy term on the right hand-side of Equation 4.24 can be rearranged. It yields to:

$$\begin{aligned} -\frac{\nabla p}{\rho_0} + \rho_k \boldsymbol{g} &= -\nabla\left(\frac{p}{\rho_0} - \rho_k g z + \rho_k g z\right) + \rho_k \boldsymbol{g} \\ &= -\nabla(p_m + \rho_k g z) + \rho_k \boldsymbol{g} \\ &= -\nabla p_m - \nabla(\rho_k g z) + \rho_k \boldsymbol{g} \\ &= -\nabla p_m - g z \nabla \rho_k - \rho_k \boldsymbol{g} + \rho_k \boldsymbol{g} \\ &= -\nabla p_m - g z \nabla \rho_k \end{aligned} \tag{4.25}$$

The momentum equation finally becomes:

$$\frac{\partial \boldsymbol{U}}{\partial t} + (\boldsymbol{U}.\nabla)\boldsymbol{U} = -\nabla p_m - g z \nabla \rho_k + \nu_{eff}\nabla^2 \boldsymbol{u} \tag{4.26}$$

As far as the discretisation of the Navier-Stokes equations is concerned, the process is more complex than for scalar transport equations because of the presence of the non-linear convective term $\nabla.(\boldsymbol{U}\boldsymbol{U})$ [57]. Besides, another difficulty is the coupling between both equations especially given the absence of any explicit equation for pressure. In order to linearise this term, the variations of velocity over a time step are assumed to be small and the transporting velocity to be equal to the velocity calculated at the previous time step. The advective term

can be reformulated as follows:

$$\nabla.(\boldsymbol{UU}) \approx \nabla.(\boldsymbol{U^0 U^n}) \tag{4.27}$$

By integrating the advective term over a given control volume, it becomes:

$$\int_{CV} \nabla.(\boldsymbol{UU})\, dv \approx \int_{CV} \nabla.(\boldsymbol{U}^0\boldsymbol{U}^n)\, dv \approx \sum_f F\boldsymbol{U}_f \tag{4.28}$$

where F is defined as $F = \boldsymbol{S}_f.\boldsymbol{U}_f^0$.

Similarly to the discretised form of the scalar equation obtained in Equation 4.21, the following semi-discretised form can be obtained for the momentum equation:

$$a_P\boldsymbol{U}_P^n + \sum_N a_N\boldsymbol{U}_N^n = \boldsymbol{R_P} - \nabla p - gz_P\nabla\rho_k \tag{4.29}$$

The coefficients a_P and a_N depend only on the velocity flux derived from the velocity calculated at the previous time step and are constant during the iterations at a given time step. After defining $\boldsymbol{H(U)}$ for a given time step such as:

$$\boldsymbol{H(U)} = \boldsymbol{R_P} - \sum_N a_N\boldsymbol{U}_N^n \tag{4.30}$$

the semi-discretised momentum equation defined in Equation 4.29 can be rewritten as:

$$a_P\boldsymbol{U}_P = \boldsymbol{H(U)} - \nabla p_m - gz_P\nabla\rho_k \tag{4.31}$$

The momentum equation is only semi-discretised at this stage in order to isolate the pressure equation later. As far as the continuity equation is concerned, its discretised form is:

$$\int_{CV} \nabla.\boldsymbol{U}\, dv \approx \sum_f \boldsymbol{S}_f\boldsymbol{U}_f = 0 \tag{4.32}$$

By dividing both side of Equation 4.31 by the coefficient a_p, $\boldsymbol{U}_P$ is derived:

$$\boldsymbol{U}_P = (a_p)^{-1}\boldsymbol{H}(\boldsymbol{U}) - (a_p)^{-1}\nabla p_m - (a_p)^{-1} g z_P \nabla \rho_k \tag{4.33}$$

The velocity on a face between two adjacent cells $\boldsymbol{U}_f$ can be derived by using the interpolated form of Equation 4.33 such as:

$$\boldsymbol{U}_f = ((a_p)^{-1}\boldsymbol{H}(\boldsymbol{U}))_f - ((a_p)^{-1}\nabla p_m)_f - ((a_p)^{-1} g z_P \nabla \rho_k)_f \tag{4.34}$$

After applying the divergence operator to Equation 4.33 and taking into account the continuity equation, the pressure equation is obtained:

$$\nabla.[(a_p)^{-1}\nabla p_m] = \nabla.[(a_p)^{-1}(\boldsymbol{H}(\boldsymbol{U}) - g z_P \nabla \rho_k] \tag{4.35}$$

As a result, the semi-discretised version of the pressure equation is:

$$\sum_f (a_p)^{-1}\boldsymbol{S}_f.(\nabla p_m)_f = \sum_f \boldsymbol{S}_f.[(a_p)^{-1}(\boldsymbol{H}(\boldsymbol{U}) - g z_P \nabla \rho_k)]_f \tag{4.36}$$

The pressure and density gradients are discretised using the CD scheme as explained in Section 4.2.1.1 are kept in this script under their gradient form for the sake of conciseness. Finally, the discretised version of the momentum equation is:

$$a_P \boldsymbol{U}_P = \boldsymbol{H}(\boldsymbol{U}) - \sum_f \boldsymbol{S}_f \left((p_m)_f - g z_P (\rho_k)_f\right) \tag{4.37}$$

and the velocity flux F can be derived from the calculated velocities $\boldsymbol{U}_f$ in Equation 4.34:

$$F' = \boldsymbol{S}_f.\boldsymbol{U}_f = \boldsymbol{S}_f.(a_p)^{-1}(\boldsymbol{H}(\boldsymbol{U}))_f - \boldsymbol{S}_f.(a_p)^{-1}(\nabla p_m)_f - \boldsymbol{S}_f (a_p)^{-1}(g z_P \nabla \rho_k)_f \tag{4.38}$$

4.6 Pressure-velocity coupling

In CFD, the most widely used algorithms to ensure the pressure-velocity coupling are the SIMPLE and PISO algorithms. SIMPLE which stands for Semi-Implicit Method for Pressure Linked Equations was originally developed by Patankar [77] and aims at solving steady-state flows. The "Pressure-Implicit with Splitting of Operators" was introduced by Issa [78] to manage the pressure-velocity coupling in the transient Navier-Stokes equations. Oliveira and Issa [79] also suggested several variants of the PISO algorithms in order to include the effects of buoyancy due to temperature gradients. Among others, they introduced a variant which consists in solving the temperature equation after the corrector loop and then to update the buoyancy term. This method is the one selected within the frame of this study. However, since modelling double diffusive phenomena requires at least solving an extra equation for the transport of concentration, the discretised equation for concentration is solved after the discretised temperature equation. The buoyancy term is then updated taking into account the calculated temperature and concentration fields. Regarding the turbulent kinetic energy and the turbulent dissipation equations, they are solved before the temperature and concentration equations. The algorithm used in this study is illustrated in Figure 4.4 and described step-by-step as follows:

Step 1: Firstly, the momentum equation is discretised isolating the parameters a_p and $\boldsymbol{H}$ such as:

$$a_P \boldsymbol{U}_P = \boldsymbol{H}(\boldsymbol{U}) - \nabla p_m - g z_P \nabla \rho_k \tag{4.39}$$

Step 2: At this stage, the pressure gradient is not known. The pressure gradient from the previous time-step is used to solve the discretised momentum equation and predict the velocity. This is the momentum predictor stage. The velocity field U^* is calculated such as:

$$\boldsymbol{U}_P^* = (a_p)^{-1} \boldsymbol{H}(\boldsymbol{U^*}) - (a_p)^{-1} \nabla p_m - (a_p)^{-1} g z_P \nabla \rho_k \tag{4.40}$$

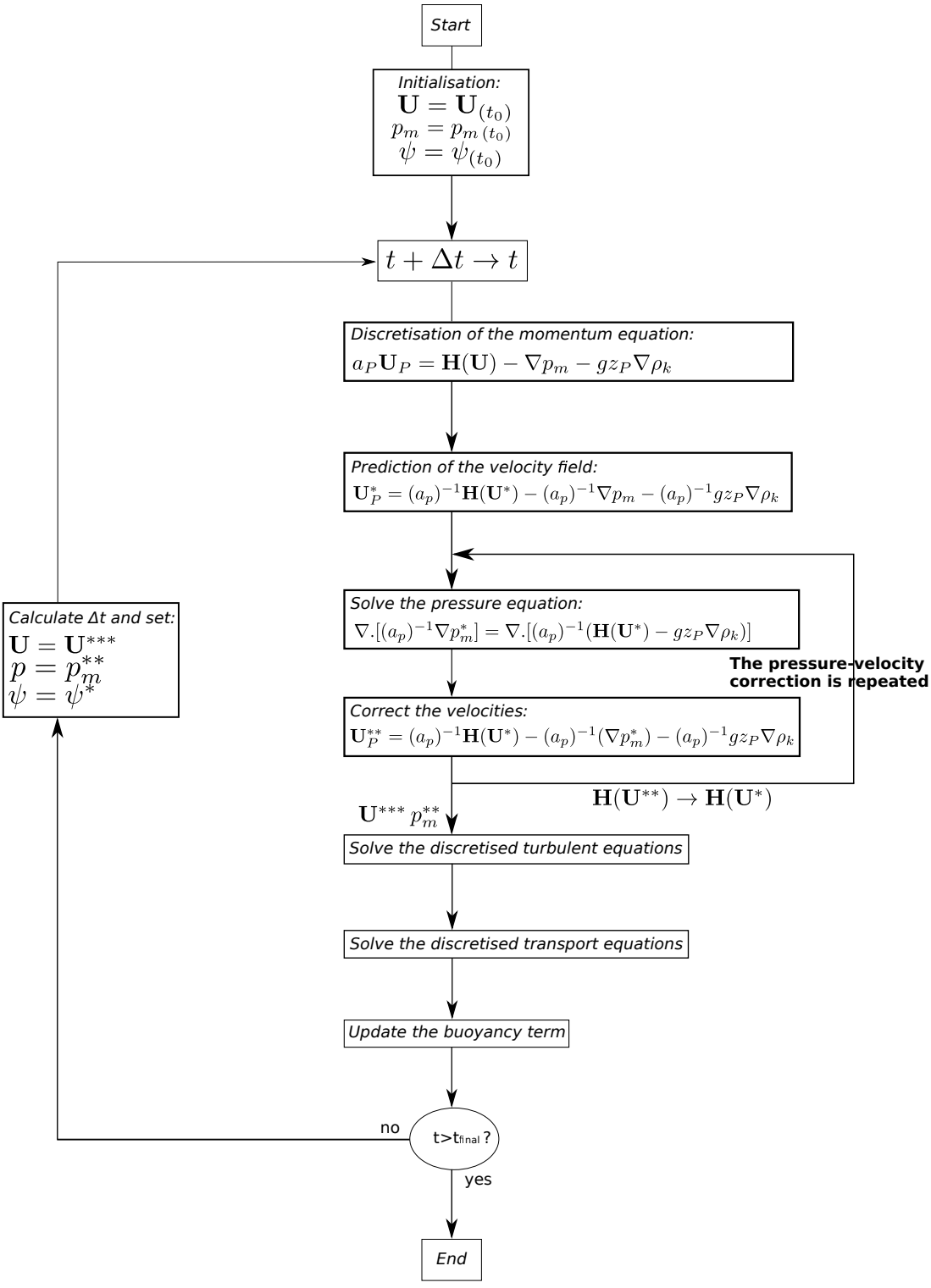

Figure 4.4: Flow chart of the developed algorithm

Step 3: The pressure equation written as:

$$\nabla.[(a_p)^{-1}\nabla p_m^*] = \nabla.[(a_p)^{-1}(\boldsymbol{H}(\boldsymbol{U^*}) - gz_P\nabla\rho_k)] \tag{4.41}$$

is then solved using the predicted velocity field.

Step 4: The velocity flux and the velocity field are corrected using the calculated pressure p_m^* such as:

$$F = \boldsymbol{S}_f.(a_p)^{-1}(\boldsymbol{H}(\boldsymbol{U}))_f - \boldsymbol{S}_f.(a_p)^{-1}(\nabla p_m^*)_f - \boldsymbol{S}_f(a_p)^{-1}(gz_P\nabla\rho_k)_f \tag{4.42}$$

and

$$\boldsymbol{U}_P^{**} = (a_p)^{-1}\boldsymbol{H}(\boldsymbol{U^*}) - (a_p)^{-1}(\nabla p_m^*) - (a_p)^{-1}gz_P\nabla\rho_k \tag{4.43}$$

Step 5-Step 6: $\boldsymbol{H}(\boldsymbol{U^*})$ is updated to the value $\boldsymbol{H}(\boldsymbol{U^{**}})$ and Steps 3 and 4 are repeated through a second pressure-velocity correction.

The steps 1 to 6 constitutes the standard PISO algorithm. The following steps are also executed in order to solve the appropriate physics:

Step 7: The turbulent equations are solved.

Step 8: The transport equations for temperature and concentration are solved.

Step 9: The buoyancy term is updated.

At the end of the iteration, the velocity and the pressure fields are updated as well as the scalar fields (temperature, concentration, density, turbulent kinetic energy and turbulent dissipation rate) denoted ψ in Figure 4.4. The procedure is repeated until the final time step is reached.

4.7 Pressure boundary condition

All the boundary conditions have been specified earlier in Section 3.4 except the pressure boundary conditions. The pressure gradient at the boundary condition is derived from the velocity flux derived from Equation 4.34. The velocity

flux can the be expressed as:

$$\boldsymbol{U}_f.\boldsymbol{S}_f = \left(\frac{\boldsymbol{H}(\boldsymbol{U})}{a_p}\right)_f.\boldsymbol{S}_f - \left(\frac{\nabla p_m}{a_p}\right)_f.\boldsymbol{S}_f - \left(\frac{gz_P\nabla\rho_k}{a_P}\right)_f.\boldsymbol{S}_f \tag{4.44}$$

After reordering Equation 4.44, it becomes:

$$\nabla p_m \cdot \boldsymbol{n} = \left(\left(\frac{\boldsymbol{H}(\boldsymbol{U})}{a_p}\right)_f.\boldsymbol{S}_f - \left(\frac{gz_P\nabla\rho_k}{a_P}\right)_f.\boldsymbol{S}_f - \boldsymbol{U}_f.\boldsymbol{S}_f\right)\frac{(a_p)_f}{||\boldsymbol{S}_f||} \tag{4.45}$$

with $\boldsymbol{S}_f = ||\boldsymbol{S}_f||\boldsymbol{n}$. The pressure gradient at the boundary is updated every PISO loop.

4.8 Courant number

The Courant number is commonly used in CFD to evaluate the accuracy of the calculations for transient simulations. It is defined in 3D as:

$$Co = \frac{U_x\Delta t}{\Delta x} + \frac{U_y\Delta t}{\Delta y} + \frac{U_z\Delta t}{\Delta z} \tag{4.46}$$

In order to limit the temporal diffusion, the Courant number must be kept to a low value, usually below 1. This ensures that the fluid particles do not cross more than a cell per time step enabling better accuracy during the transient regime. As a result, the time steps, in the simulations conducted in the framework of this thesis, were continuously updated from the calculation of the Courant number so as to maintain the latter below 1 during all the simulations.

4.9 rolloverFoam features

OpenFOAM is an opensource CFD toolbox written in C++ and initially developed by Weller and Jasak [70] within the Imperial College London in the early 90s.

OpenFOAM is currently composed of several solvers able to model different physics among which incompressible flows, buoyancy-driven flows, combustion and multiphase flows. Its main advantage is its flexibility. Indeed, via C++ coding, it is relatively easier than with other commercial software packages to modify the existing code in order to develop the available models or to implement new ones.

As a result, within the frame of this study, a predictive tool for rollover was developed based on the existing OpenFOAM library. This solver, rolloverFoam, takes into account the methodology presented in this chapter while solving numerically the equations governing the physics involved during rollover and introduced in Chapter 3. The features of the solver are the following:

- The code is based on the existing solver buoyantBoussinesqPimpleFoam which can solve the transient flow of an incompressible liquid subject to buoyancy and turbulence. This solver uses the Boussinesq approximation as well as the linear approximation of the density presented in Section 3.1.2.

- In addition to buoyantBoussinesqPimpleFoam characteristics, rolloverFoam models multicomponent mixtures where a component is in excess compared to one or several other species. Besides, it also takes into account the transport equations for the solutal concentrations which were integrated within the PISO algorithm presented in Section 4.6.

- The equation for density was improved to take into account its dependence on both the liquid temperature and composition. To this aim and to model both binary mixtures and LNG, the modified linear approximation, presented in Section 3.1.2.2, and the Klosek-McKinley method [80] were developed.

- The solver can be combined to a modified version of the k-ϵ turbulence model, also developed in this study, integrating the effects of the buoyancy

due to both the liquid temperature and compositions on the turbulence. These models were presented in Sections 3.2.6 and 3.2.7.

- Finally, a boundary condition was implemented to reflect the evaporative condition highlighted by Hashemi and Wesson [33].

4.10 Summary

In this chapter, the foundations of the numerical approach adopted in this thesis have been presented. This method based on the finite volume method requires time and space discretisation, as well as numerical schemes to turn the equations governing the physics involved during rollovers into a system of algebraic equations. The linear systems obtained after discretising the scalar transport equations such as the temperature, concentration and turbulent equations, are solved using iterative methods following preconditioning which accelerates significantly the convergence rate. As far as the pressure and velocity fields are concerned, given that they are coupled through the non-linear momentum equation, they are solved iteratively during the PISO algorithm going through several corrections. Finally, the rollover predictive code, rolloverFoam, developed in this study and based on OpenFOAM was presented.

Chapter 5

Results and discussion - model validation and applications

In this chapter, the rollover predictive code, rolloverFoam, developed within the frame of this thesis, and, presented in Section 4.9, is, at first, applied to two different cases published in the literature by Shi [14] and Munakata et al. [15]. These two cases are interesting for two reasons. They are first used to validate rolloverFoam numerically. Besides, given that the results coming from these two studies seem contradictory regarding the mechanism driving the rollover phenomenon, the idea is to investigate if both of these mechanisms are possible. In a second part, the predictive tool is applied to small-scale experiments conducted with a mixture of Freon by Nakano et al. [8]. From these experiments, some parametric studies are conducted to assess the influence of several key parameters on the rollover phenomenon. Finally, the code is applied to several LNG rollovers including a medium-scale LNG rollover experiment, La Spezia incident and a fictive rollover onboard a FLNG carrier.

	Shi	**Munakata et al.**
$\eta = \frac{R}{H}$ *or* $\frac{W}{H}$	1	1
$\frac{H_{bot}}{H}$	0.5	0.5
$Pr = \frac{\nu}{\alpha}$	2.3	30
$Sc = \frac{\nu}{D}$	71.5	5500
$Ra^* = \frac{g\beta_T \dot{q} H^4}{\alpha\nu\lambda}$	1.0×10^7	$1.64 \times 10^8 / 2.46 \times 10^9$
$Ra_C = \frac{g\beta_C \Delta C}{D\nu}$	9.25×10^7	4.42×10^9
Re[1]	122	43

Table 5.1: List of parameters used by Munakata et al. [15] and Shi [14]. [1]: the Reynolds number is calculated from the simulated flow.

5.1 Numerical validations

Shi [14] and, later, Munakata et al. [15] have developed CFD codes modelling rollovers in order to get more insights into the phenomenon. While Shi's code is based on finite volume, Munakata et al.'s employs the finite difference method. These two models are also derived from different equations than the method developed in the frame of this thesis. Indeed, the fluid dynamics is calculated from the vorticity and the stream function equations. As for the density, it is derived in these two studies after considering that density varies linearly with concentration and temperature as defined in Equation 3.21.

Besides, as explained in the literature review in Chapter 2, these two methods have highlighted two different physics leading to rollovers. In Shi's case, rollover was obtained following the downward motion of the interface while Munakata et al. found that it was due to the penetration of a thin layer from the bottom layer into the top layer. As a result, in this section, the proposed method will first be applied to the cases studied by Shi and by Munakata et al. for numerical validations but it also aims at assessing the realisability of the different physical phenomena highlighted by these researchers.

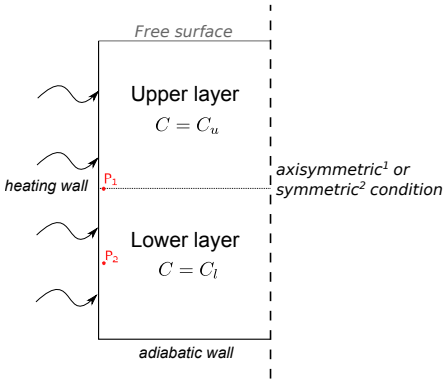

Figure 5.1: Schematic of the initial conditions and boundary conditions

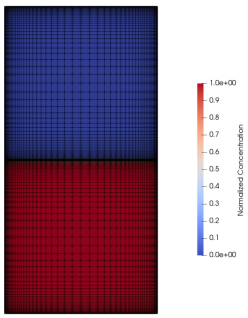

Figure 5.2: Mesh and initial concentration field

5.1.1 Numerical model

Shi [14] and, Munakata et al. [15] assumed the flow to be laminar given that the modified Rayleigh number is inferior to the critical Rayleigh number of 10^8. As a result, Shi considered that the study could be, not only limited to the study of a 2D model, but even to half of this 2D model assuming that the flow does not break the symmetry of the geometry. As for Munakata et al., they assumed that the flow in a cylindrical enclosure could be fully solved by using an axisymmetric model.

Although their models do not use the same condition of symmetry, they are similar in many points. The models used by these researchers is summarised in Figure 5.1. The liquid is bounded by an adiabatic wall below and a heating wall on its side. The heating intensity is derived from the modified Rayleigh number presented in Table 5.1. At the centre, the condition of symmetry is used. It is a symmetric boundary condition for Shi and an axisymmetric one for Munakata et al. [15]. Besides, in both cases, the width of the model is equal to half of its height. Regarding the top surface which is a free surface, it assumed to be isothermal for Shi and adiabatic for Munakata et al. [15]. Concentrations were initialised following a step profile where the highest concentrations of the heavier solute are below the interface located at half of the total height. Last but not least, the considered liquid are different in these two approaches: while Shi

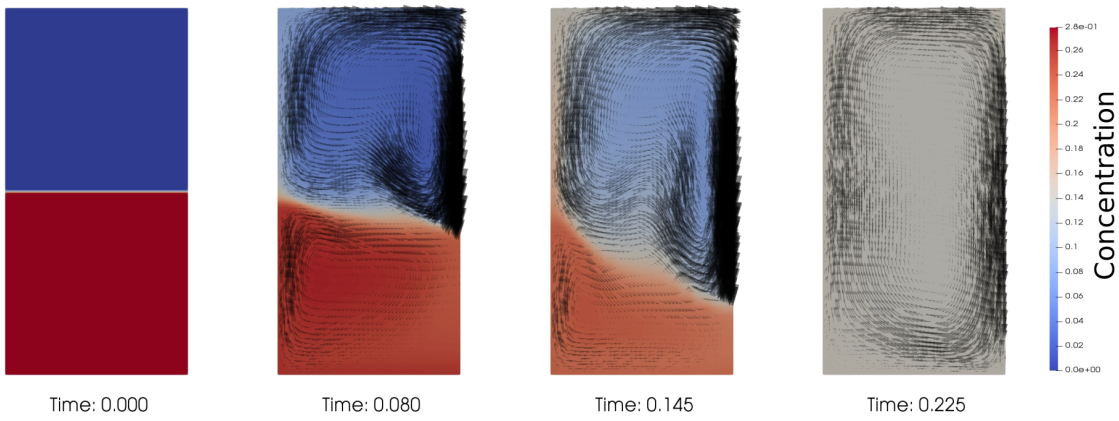

Figure 5.3: Concentration fields at different stages of rollover in Shi's test case (symmetric model)

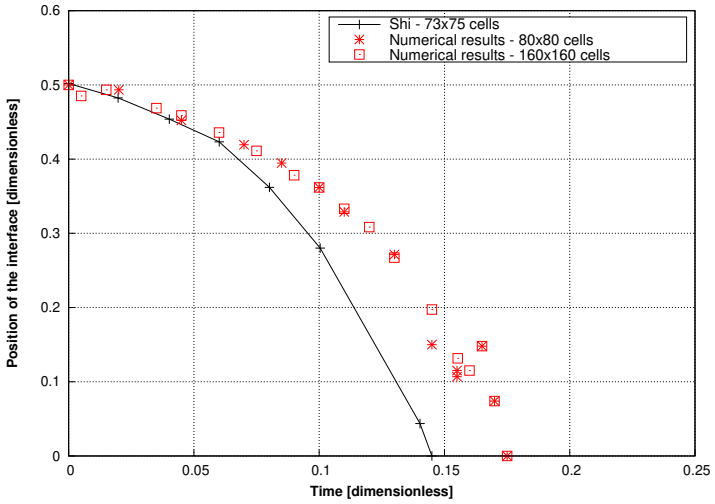

Figure 5.4: Numerical comparison of the motion of the interface

simulated rollover in a mixture of liquid nitrogen and liquid oxygen, Munakata et al. studied the phenomenon in a mixture of water and ethanol.

In both cases, the mesh used to discretise the model is made of quadrilateral cells and is refined near the interface and near the boundaries. The mesh used by Shi and Munakata et al., are respectively made of 73x75 and 60x120 cells. Similar grids are used for numerical validation such as the grid employed in this study to discretise Munakata et al.'s case depicted in Figure 5.2.

5.1.1.1 Comparison with Shi's results

Shi's case has been simulated with rolloverFoam. First, the Reynolds number is calculated from the numerical results. Its low value ($Re = 122$) corroborates the assumption stating the flow as laminar. Besides, 2D visualisations of the numerical results are depicted in Figure 5.3 as well as in Appendix B. One can see that the interface between the layers is pushed downwards caused by the intensifying convective cell in the upper layer. As a result, qualitatively, the observed phenomenon is the same as the one identified by Shi and explained in Section 2.6.2.

The interface, which is monitored during the simulation, is compared to Shi's numerical results. The results are shown in Figure 5.4 with the same conventions and dimensionless parameters as used by Shi [14]. One can see that the numerical results obtained with rolloverFoam are identical with two different mesh grid sizes as depicted with red symbols. The results are also following the same trend as the one obtained by Shi. Indeed, while the interface starts to move slowly downwards, it gains speed after a dimensionless time $\tilde{t}$ around 0.1 against 0.06 in Shi's simulation. The interface finally reaches the tank bottom at $\tilde{t} = 0.17$ against $\tilde{t} = 0.145$ in Shi's simulation. This delay ($\Delta\tilde{t} \approx 20\%$) may be due to a different initialisation or a different mesh grid.

5.1.1.2 Comparison with Munakata et al.'s results

RolloverFoam was also applied to Munakata et al.'s case [15] with a mesh made of 60x120 cells as illustrated in Figure 5.2. The numerical results, obtained for $Ra^* = 9.25 \times 10^7$ and $Ra_C = 4.42 \times 10^9$, confirm their findings and the low Reynolds number ($Re = 43$) is in agreement with the assumption of laminar flow. 2D visualisations of the phenomenon, provided in Figure 5.5, are very similar to those published in [15]. From these results, one can see that the interface is rapidly destabilised after $\tilde{t} \approx 0.01$. At that moment, a thin layer of liquid from

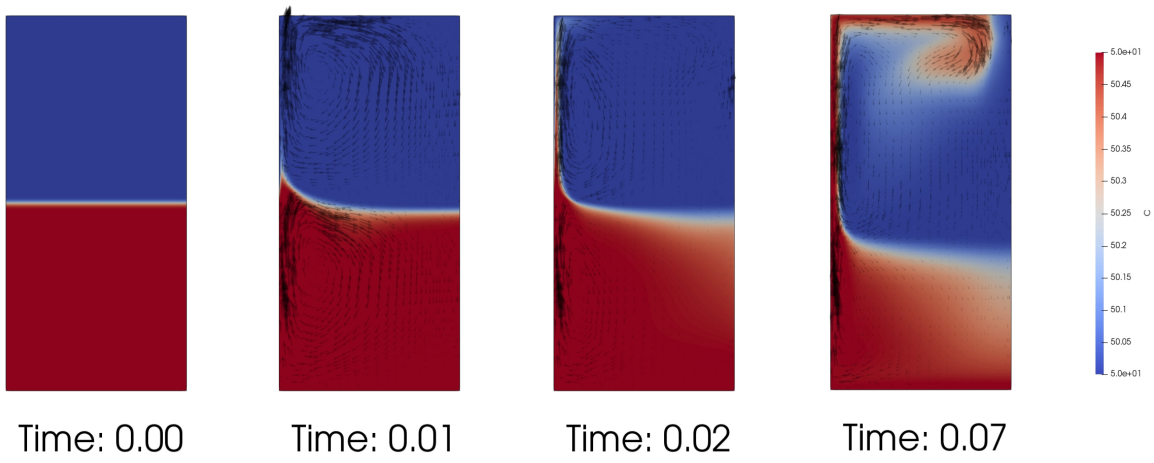

Figure 5.5: Concentration fields at different stages of rollover in Munakata et al.'s test case for $Ra^* = 9.25 \times 10^7$ and $Ra_C = 4.42 \times 10^9$ (axisymmetric model)

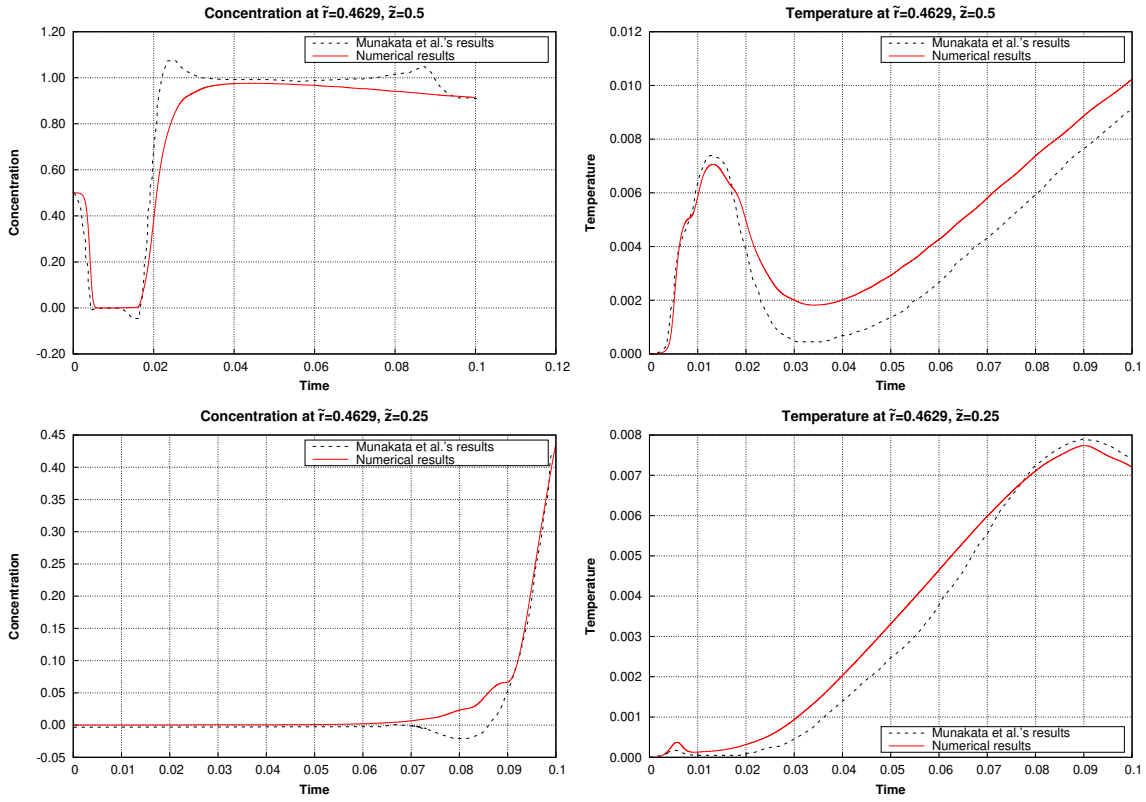

Figure 5.6: Numerical comparison of the dimensionless concentration and temperature at the points $P_1(0.4629, 0.5)$ and $P_2(0.4629, 0.25)$ for $Ra^* = 2.46 \times 10^9$ and $Ra_C = 4.42 \times 10^9$

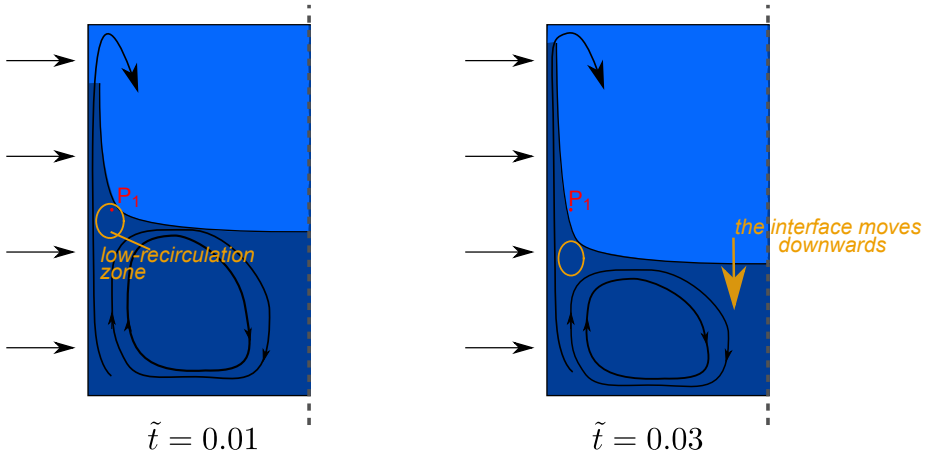

Figure 5.7: Scheme explaining the change in concentration and temperature at P_1 following the penetration of the interface

the bottom layer breaks the interface and starts penetrating into the upper layer. As a consequence, the liquid from the lower layer is drained into the upper layer contributing to the downward motion of the interface between $\tilde{t} \approx 0.02$ and $\tilde{t} \approx 0.07$.

In their paper [15], Munakata et al. also provided quantitative results for the same set-up but with a different heating rate. As a consequence, the solutal Rayleigh number Ra_C is unchanged and the Rayleigh number is increased from 9.25×10^7 to 2.46×10^9. Munakata et al. presented the values of the changes in temperature and concentration at two points P_1 and P_2 located near the lateral wall respectively near the initial position of the interface and at half the height of the lower layer as described in Figure 5.1. The changes in temperature and concentration calculated at these points with rolloverFoam are compared to the ones in their article. The results are depicted in Figure 5.6. The normalised coordinates $(\tilde{r}, \tilde{z})$ of P_1 and P_2, defined such as $\tilde{r} = \frac{r}{H}$ and $\tilde{z} = \frac{z}{H}$, are respectively (0.4629, 0.5) and (0.4629, 0.25). The same conventions as the ones employed by Munakata et al. in their paper are used for the dimensionless parameters shown in Figure 5.6. The dimensionless temperature is then defined such as $\tilde{T} = \frac{T - T_0}{qH/\lambda}$, the dimensionless concentration such as $\tilde{C} = \frac{C - C_l}{C_u - C_l}$ with C_u and C_l, the concentrations of, respectively, the upper and lower layers and the dimensionless

time such as $\tilde{t} = \frac{t}{H^2/\nu}$. Firstly, it turns out that, the results calculated with rolloverFoam for the concentration and temperature at P_1 and P_2, shown with the dotted black lines in Figure 5.6, are in good agreements with the results obtained by Munakata et al. [15] shown with the red full lines.

In parallel, the time-varying concentration and temperature fields are provided in Appendix B. P_1 is initially located at the interface between the layers, hence the initial value of $\tilde{C} = 0$. The concentration C rapidly increases due to the superheated and buoyant thin layer from the lower layer pushing the interface near the wall upwards. As a result, the concentration at P_1 increases and consequently, by definition, the dimensionless concentration $\tilde{C}$ decreases up to $\tilde{t} \approx 0.005$. In Figure 5.6, one can see that the dimensionless concentration $\tilde{C}$ rises. In the meantime, and, as illustrated in Figure 5.7, a low-recirculation zone settles near the interface between the convective cell in the lower layer and the rising liquid near the walls. In this particular zone, the velocity is relatively low compared to the neighbouring area. A direct consequence is the accumulation of energy in this area hence the initial increase in dimensionless temperature $\tilde{T}$. Rapidly, because of the liquid leaving the lower layer to enter the upper layer, the level of the interface decreased. Besides, as illustrated in Figure 5.7, the width of the "improvised channel" created by the penetration of the liquid into the upper layer narrows as one moves away from the interface level. Because of the downward motion of the interface, P_1 which was initially within the lower layer, is after $\tilde{t} = 0.017$ located in the upper layer and outside the low-recirculation zone. As a result, when the dimensionless time is comprised between 0.017 and 0.035, the dimensionless concentration $\tilde{C}$ is then increased while the temperature is decreased. Finally, given that the system accumulates heat — the upper layer being adiabatic — the temperature keeps increasing in the upper layer (cf. Appendix B), hence the rise of temperature at P_1 after $\tilde{t} = 0.035$ until $\tilde{t} = 0.1$. One can also observe that the penetration of the fluid from the lower layer into the upper one promotes the mixing of the layers which increases the concentration

at P_1 and consequently decreases the dimensionless concentration.

Besides, regarding the point P_2, the dimensionless concentration remains up to $\tilde{t} = 0.06$ equal to nil, as the mass transfer is initially limited between the layers and as the point P_2 remains in the lower layer. Then, because of the growing mass transfer through the interface due to its motion and the reduced density difference between the layers, the concentration decreases and consequently the dimensionless concentration increases at P_2. In the meantime, the whole system accumulating significant amounts of heat without releasing it and the low-recirculation area getting closer to P_2 (cf. Appendix B), the temperature $\tilde{t}$ at P_2 is increased during the simulation.

Finally, it also turns out that the method proposed in this thesis is more stable and avoids non-physical overshooting. Indeed, the dimensionless concentration $\tilde{C}$ as defined by Munakata et al. should be comprised between 0 and 1 since there is no solute entering or leaving the domain. However, one can observe on Figure 5.6 that the normalised concentration calculated by Munakata et al. overshoots the value of 1 after $\tilde{t} = 0.025$ at P_1 and the value of 0 at P_2 and after $\tilde{t} = 0.08$.

5.1.2 Conclusion

The developed method was, at first, applied to the same cases as the two main studies in the literature involving rollovers and CFD and conducted by Shi [14], and, Munakata et al. [15]. The results obtained with the developed method have shown good agreements with the numerical results presented by these researchers. Besides, on the one hand, Shi has demonstrated that rollover was the result of the downward motion of the interface. On the other hand, Munakata et al. have highlighted that it was the result of the penetration of a thin layer from the bottom layer into the top layer. The applications of rolloverFoam to these two cases have shown that these two phenomena leading to rollovers could be obtained and simulated with the proposed approach.

Finally, although these models gave some significant insights into the rollover phenomenon, the results provided by Shi and Munakata et al. were only qualitative and so were the results from Lemembre [16] and Seveleder [17]. The idea of the following sections is to illustrate that rolloverFoam can also predict rollovers reliably by applying it to the cases of small-scale experiments with Freon and to medium-scale and real-scale LNG rollovers.

5.2 Rollovers in small-scale experiments

Several researchers have conducted small-scale experiments in order to understand the physics of rollovers. Among them, Nakano et al. [8] and Shi [14] used cryogenic mixtures of Freon which has similar physical properties to LNG. Several of their experiments were reported in details in the available literature. As a result, the rollover predictive code, rolloverFoam is applied to these experiments so as to assess its validity. These results will give some first insights into rollovers.

Besides, one of the main advantages of CFD compared to experiments is its relative easiness to modify a given characteristic parameter without having to change the whole set-up. As a result, the validated method will be employed to study the influence of several characteristic parameters such as the heating rate, the bottom heating or the size of the top layer.

5.2.1 Nakano et al. experiment

Nakano et al. experimented rollovers with a rectangular enclosure which was 490 mm wide, 390 mm high and 200 mm deep as illustrated in Figure 5.8. The top, front and rear walls were made of 30 mm glass while the side and bottom walls were made of copper plates which could be heated depending on the requested configuration. Besides, the walls are impermeable to liquids and gases.

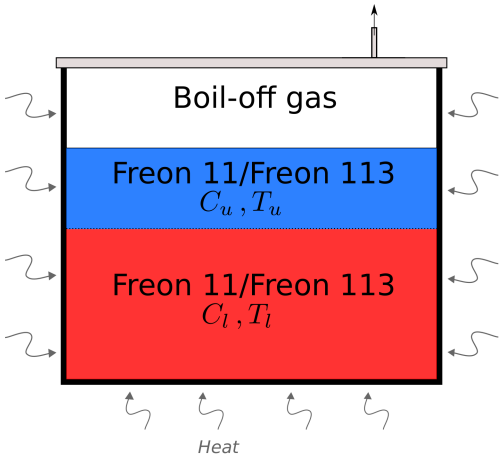

Figure 5.8: Experimental set-up used by Nakano et al. (adapted from [8])

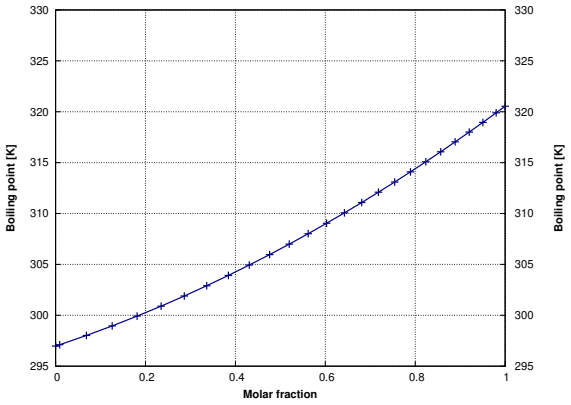

Figure 5.9: Variation of saturation temperature with molar fraction (cf. Appendix C)

As for the studied fluid, it was a binary mixture mainly made of Freon 11 but which also contains fewer amount of Freon 113. A stable stratification was obtained after injecting slowly a denser mixture more concentrated in Freon 113 below a lighter and less concentrated one.

5.2.2 Fluid Properties

The main interest of using Freon 11 is its similar behaviour to LNG but at room conditions, which avoids the use of heavily insulated enclosures. Indeed, Freon 11 is liquid at standard temperature and pressure conditions and its saturation temperature is 296.8 K. It is then possible to observe boil-off after heating the liquid slightly.

In this study, the saturation temperature is considered to vary with the composition of the binary mixture. It is expected that a liquid with low amounts of Freon 113 will tend to behave like a pure mixture of Freon 11. Inversely, for considerably high amounts of Freon 113, the liquid properties including its saturation temperature will tend to equalise those of a pure mixture of Freon 113. Between these extrema, the saturation temperature is derived after assuming the mixture to be ideal and after using both Antoine's equation and Raoult's law as developed in Appendix C. The correlation linking the saturation temperature to the molar fraction of Freon 113, denoted x, is obtained and provided in Figure 5.9. One can observe that the boiling point varies over more than 20 K depending on the molar fraction of Freon 113. The polynomial interpolation of second order of these results gives the following relation:

$$T_{sat} = 8.93916\,x^2 + 14.62764\,x + 296.97688 \tag{5.1}$$

The solutions used in these experiments are mixtures mainly made of Freon 11 in which are dissolved fewer amounts of Freon 113. It is assumed that all the thermophysical properties apart from the density remain constant over the small variations of temperature and concentration encountered during the experiments. Their values are taken equal to those of a pure mixture of Freon 11 at 296 K and are obtained from the NIST Chemistry Webbook [81]. The diffusivity of Freon 113 within a solution of Freon 11, denoted D, is calculated using the relation suggested by Wilke and Chang [54] and is also assumed constant during the experiment. The adopted values for the thermal diffusivity α, the mass diffusivity D, the kinematic viscosity ν, the thermal conductivity λ, the latent heat L, the thermal and solutal expansion coefficients, β_T and β_C are reported in Table 5.2. The derived Prandtl and Schmidt numbers are respectively equal to 4.3 and 65. Besides, the density is calculated from the modified Boussinesq approximation presented in Equation 3.21.

	Freon/Freon 113
$\alpha\,[m^2/s]$	$6.88{\cdot}10^{-8}$
$D\,[m^2/s]$	$4.55{\cdot}10^{-9}$
$\nu\,[m^2/s]$	$2.96{\cdot}10^{-7}$
$\beta_T\,[K^{-1}]$	$1.6{\cdot}10^{-3}$
$\beta_C\,[\%wt^{-1}]$	$5.5{\cdot}10^{-2}$
$\lambda\,[W/(m.K)]$	$8.7{\cdot}10^{-2}$
$L\,[kJ/kg]$	180

Table 5.2: Properties of the mixture of Freon 11/Freon 113 [81]

5.2.3 Numerical set-up

The rollovers experimented by Nakano et al. [8] are simulated numerically both with 2D and 3D models. Despite the symmetry of the enclosure geometry, and unlike previous approaches adopted by Shi [14] and Munakata et al. [15], the model is intentionally not reduced to half a domain so as to anticipate the effects of turbulence on the flow. The modified Rayleigh number in the following experiments, being of the order of to 10^{13}, witnesses the turbulence which could potentially break the symmetry of the flow.

As far as the boundary conditions for the concentration are concerned, given that the walls are impermeable, the gradients of concentration normal to the walls are equal to nil. Besides, regarding the temperature conditions, the walls made of copper are assumed to supply a constant flux and the glass walls in contact with the liquid are considered as adiabatic since the liquid temperature is approximately the same as the room temperature. Regarding the heat supplied to the vapour space, it is assumed that it does not contribute to warm up the liquid given that the order of magnitude of the supplied heat is significantly lower than the heat released by evaporation. This assumption will be verified hereafter.

Finally, the numerical boundary conditions for temperature, concentration

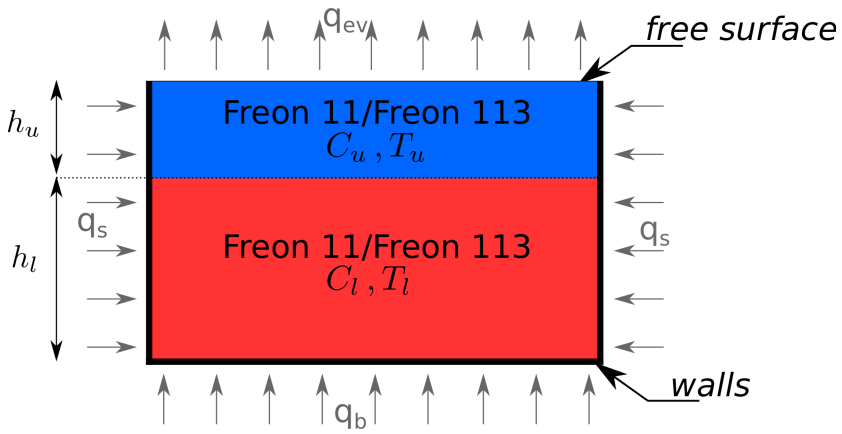

Figure 5.10: Numerical model

and velocity, developed in Section 3.4 and illustrated in Figure 5.10 can be expressed as follows:

- At the side walls:

$$\boldsymbol{U} = \boldsymbol{0} \tag{5.2}$$

$$\nabla C.\boldsymbol{n} = 0 \tag{5.3}$$

$$\nabla T.\boldsymbol{n} = \frac{q_s}{\lambda_{eff}} \tag{5.4}$$

- At the bottom wall:

$$\boldsymbol{U} = \boldsymbol{0} \tag{5.5}$$

$$\nabla C.\boldsymbol{n} = 0 \tag{5.6}$$

$$\nabla T.\boldsymbol{n} = \frac{q_b}{\lambda_{eff}} \tag{5.7}$$

- At the free surface:

$$\boldsymbol{U}.\boldsymbol{n} = U_z = 0 \tag{5.8}$$

and

$$\frac{\partial U_x}{\partial z} = 0 \quad \text{and} \quad \frac{\partial U_y}{\partial z} = 0 \tag{5.9}$$

$$\nabla C.\boldsymbol{n} = -\frac{\dot{\boldsymbol{m}}_{R113}.\boldsymbol{n}}{D_{eff_i}} = \frac{\dot{m}}{D_{eff}}\left(\frac{C}{\rho - C}\right) \tag{5.10}$$

$$\nabla T.\boldsymbol{n} = \frac{q_{ev}}{\lambda_{eff}} \tag{5.11}$$

where $\dot{m}$ is defined following the explanations given in Section 3.3 as:

$$\dot{m} = \frac{q_{ev}}{L} = \begin{cases} 0, & \text{if } T_{bulk} < T_{sat} \\ C_m \frac{\lambda}{L} \left(\frac{\beta_T g}{\alpha \nu} \right)^{1/3} (T_{bulk} - T_{sat})^{4/3}, & \text{if } T_{bulk} \geq T_{sat} \end{cases} \tag{5.12}$$

with T_{bulk} the average temperature in the upper layer and T_{sat} the saturation temperature calculated using Equation 5.1

Regarding the initialisation, a strong stratification is assumed. A step profile is adopted both for temperature and concentration such as they are respectively equal to T_l and C_l in the lower layer and to T_u and C_u in the upper layer.

The turbulence is modelled via the low-Reynolds-number k-ϵ model developed by Launder and Sharma [62] and introduced in Section 3.2.7.

As far as the schemes used to discretised the governing equations are concerned, the transient terms are discretised following the Euler implicit method, while second-order upwind schemes are used for the convective terms. Regarding the gradient terms, they are discretised with central differencing schemes.

5.2.4 Simulation of "Test 15"

Nakano et al. repeated several times the same experiment with varying heating conditions and initial stratification. The comprehensive experimental results from "Test 15" are available in their article [8]. As a result, the study hereafter focuses on comparing the numerical results obtained with the method developed in this thesis to their experimental results.

5.2.4.1 Initial conditions

Before proceeding to the rollover experiment, the fluid was initially stratified as follows:

- the heights of the lower and upper layers are respectively 211 mm and 131 mm.
- the lower layer is initially slightly hotter than the upper layer: the temperature in the bottom layer and top layer are respectively 296 K and 295.65 K.
- the lower layer is more concentrated in Freon 113 than the upper layer: the mass fraction of Freon 113 is respectively, 0.221 and 0.06 in the bottom and top layer.

However, as far as the heating power is concerned, the report is not clear. A reported "heat flux" of 30 W through the side walls and 20 W through the wall below are indicated while it actually corresponds to a power. This may imply that the electrical power converted by the heaters into heat was 30 W on the sides and 20 W below during "Test 15". As a result, this power corresponds to the heating power and may differ from the heat received by the liquid because of the lack of insulation for example. The actual heat flux transmitted to the liquid would then be equal to the effective power transmitted to the liquid divided by the wall surface area.

5.2.4.2 Mesh selection and heating conditions

A 2D and a 3D model are developed to simulate the experiment. The adopted 2D and 3D mesh grids are respectively made of quadrilateral cells and hexahedrons cells as shown in Figure 5.11. The grids are both refined at the boundaries to ensure that the y^+ value in the near-wall area remains below 6 so as to capture the physics within the boundary layer. The mesh grid size is also finer around the initial position of the interface to model realistically the heat and mass transfer between the layers.

Simulations are firstly carried out on the 2D mesh to assess appropriate values for the heating rates through the copper plates. Given that the position of the

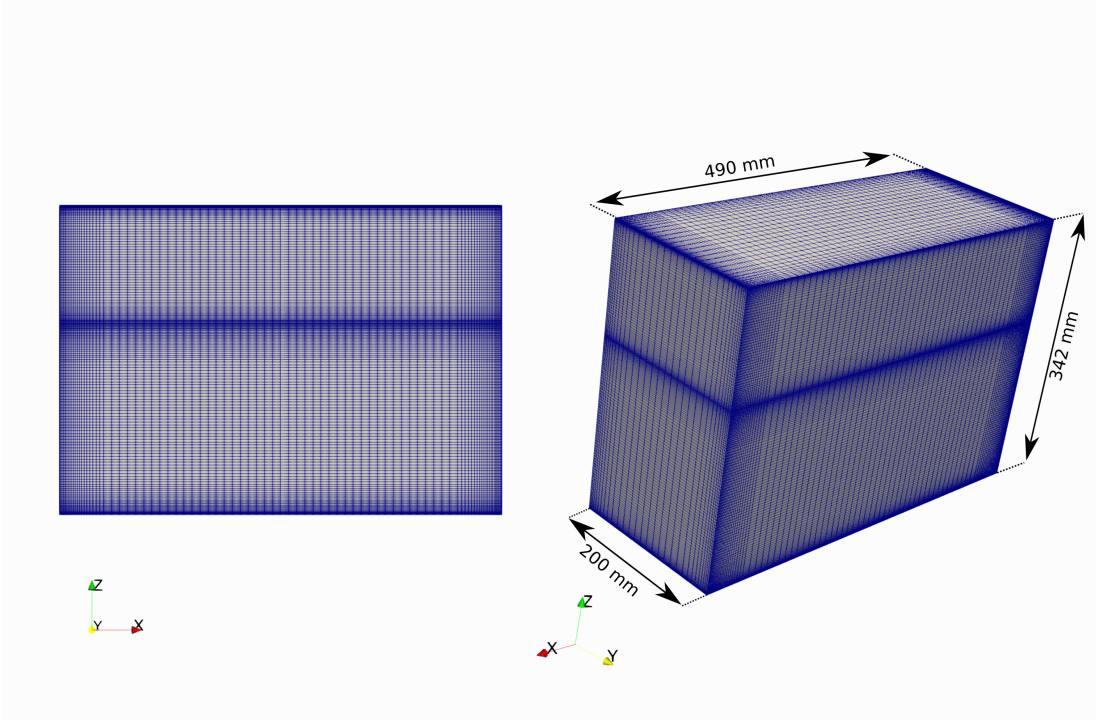

Figure 5.11: Presentation of the 2D (on the left) and 3D mesh grids (on the right)

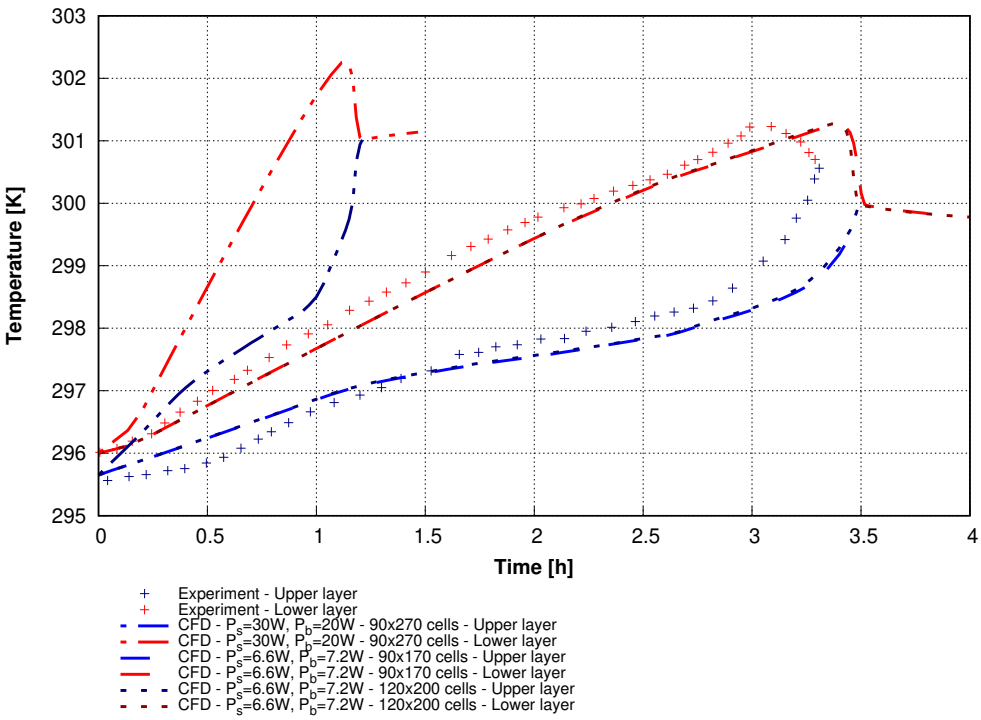

Figure 5.12: Variation of the averaged temperature in both layer during rollover for different heating rates

probes is not reported, the numerical values are averaged over the layers. It turns out that the elevations of temperature in both layers are significantly higher than the experimented one as it can be observed in Figure 5.12. In the absence of any indication from Nakano et al. [8] about the heat losses, it has been chosen, following an estimation of the heat power from the energy budgets of both layers as described in Appendix D, to consider the heating received by the liquid equal to 6.6 W through the side walls and 7.2 W through the wall below. The temperatures simulated in these conditions are closer to the experimented temperatures as shown in Figure 5.12. Besides, taking into account these values for the heat supplied to the system, and considering all the heat supplied ($\approx 1.2W$) to the vapour space is transferred to the liquid and evaporated straightaway, the boil-off rate would be approximatively 0.02 kg/h. However, the latter was observed during "Test 15" to be since the beginning of the experiment higher than 0.25 kg/h. Consequently, the heating of the liquid by the vapour can be neglected confirming the assumption raised in Section 5.2.3.

A mesh sensitivity study is carried out on the 2D model. It highlighted, as shown in Figure 5.12, that increasing the mesh size beyond 90 cells in the x-direction and 170 in the z-direction do not influence the results. The selected 2D mesh is made of 15,300 cells. The same mesh was used and expanded in the y-direction. A mesh sensitivity study determined the final 3D mesh as made respectively of 90, 30 and 170 cells in the x, y and z directions which corresponds to 459,000 cells.

5.2.4.3 Results and discussion

Temperature, concentration and density were measured experimentally with probes. The reported data hence depend on the probe location during the experiment, although, the convective motions in both layers tend to homogenise the flow on both sides of the interface. As a result, the numerical values obtained for temperature, concentration and density are averaged over the layer. These three

Table 5.3: Concentration, temperature and density fields at different stages of rollover

	Concentration	**Temperature**	**Density**
Before rollover $(t = 5,580\,s)$	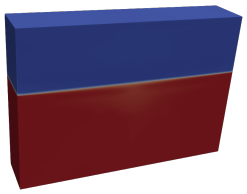	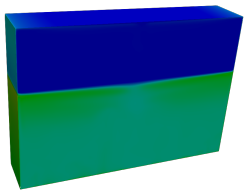	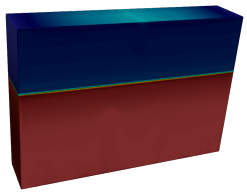
The interface starts moving downwards $(t = 12,240\,s)$	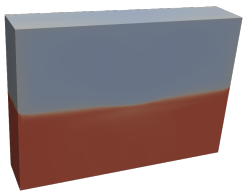	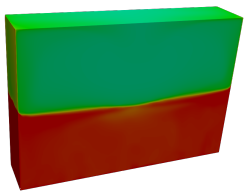	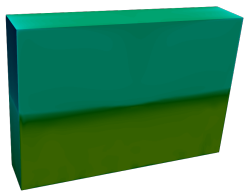
Penetration of a thin layer from the lower layer $(t = 12,780\,s)$	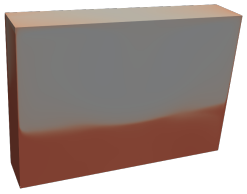	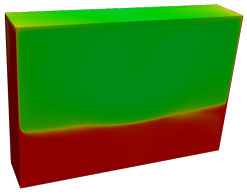	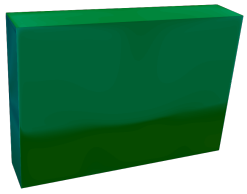
Complete mixing $(t = 13,140\,s)$	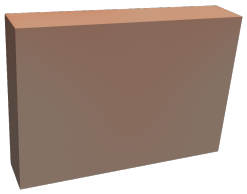	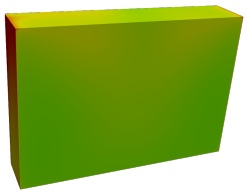	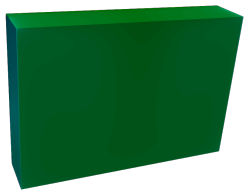
	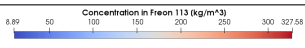	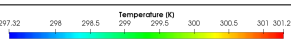	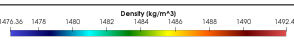

Table 5.4: Velocity streamlines and velocity magnitude field at different stages of rollover

	Streamlines	**Velocity**
Before rollover ($t = 5,580\ s$)	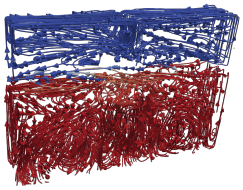	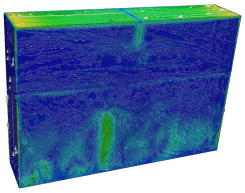
The interface starts moving downwards ($t = 12,240\ s$)	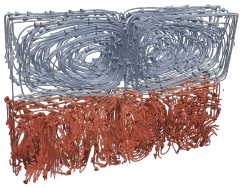	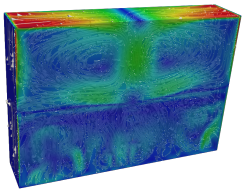
Penetration of a thin layer from the lower layer ($t = 12,780\ s$)	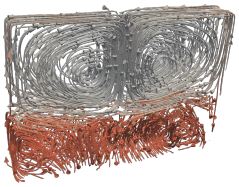	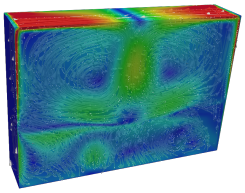
Complete mixing ($t = 13,140\ s$)		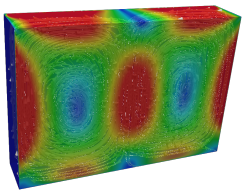
	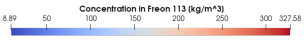	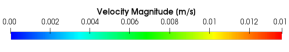

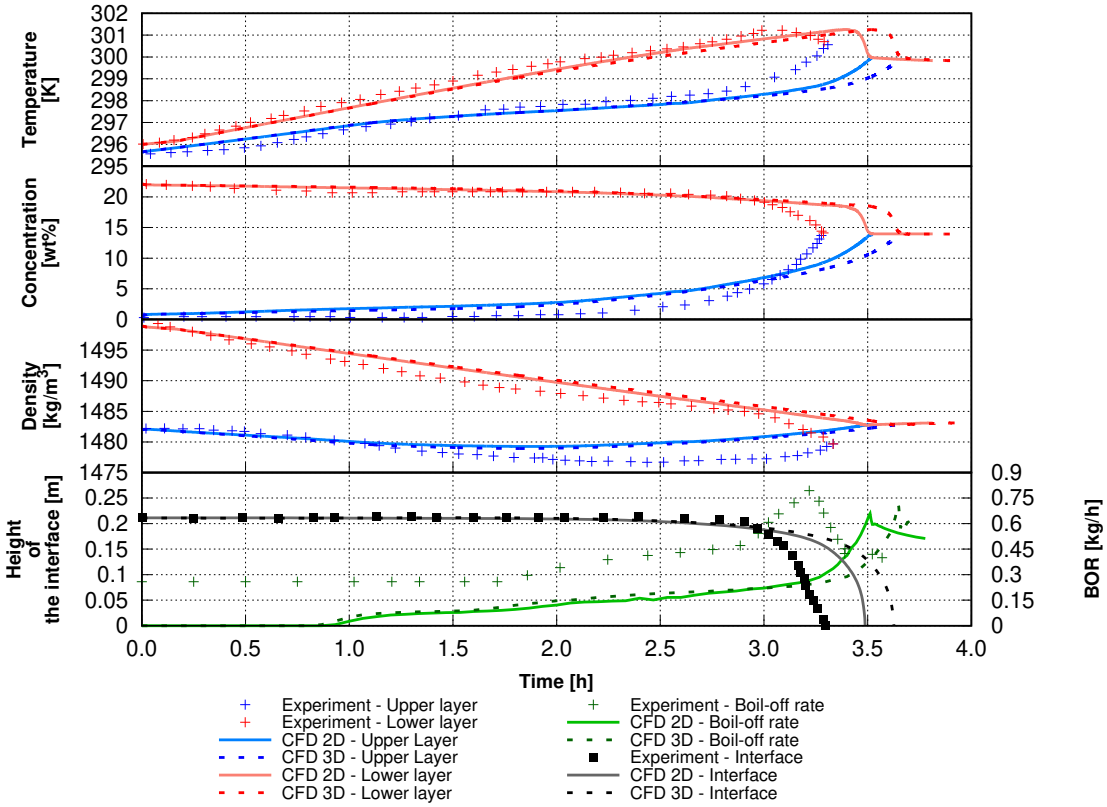

Figure 5.13: Comparison of experimental and numerical results from stratification until complete mixing

parameters, as well as the boil-off rate and the interface position are compared to the experimental data, probed in both layer, from the initial stratification until complete mixing. The results are reported in Figure 5.13. In parallel, the fields for concentration in Freon 113, temperature and density obtained from the CFD simulations at several stages of the mixing are also supplied in Tables 5.3 and 5.4 so as to give a comprehensive understanding of the rollover phenomenon to the reader.

From Figure 5.13, one can see that the numerical results obtained with the 2D and 3D meshes and the experimental results show relative good agreements for the evolution of temperature, concentration and density in both strata. The numerical evolutions of the position of the interface as well as the calculated boil-off rate follow the same trend as the experimented values. However, one can notice that the simulated boil-off rate is considerably lower than the experimented value especially at the beginning of the experiment. Whereas the temperature

of the upper layer is known from Nakano et al. to be initially cooler than the liquid saturation temperature, a boil-off rate can be observed. In the case all the heat supplied to the vapour space was transferred to the liquid and suddenly evaporated, it would only correspond to a boil-off rate of 0.023 kg/h which is significantly lower the observed rate of 0.2 kg/h. As a result, it is likely that the difference is due to the initialisation and the assumption that the layers are homogeneous. A consequence is that underestimating the boil-off rate prior to the mixing limit the densification of the upper layer due to evaporation. This justifies that the predicted rollover time is overestimated compared to the experimented one (210 min for the simulated rollover time against 190 min for the experimented one which represents 9.5% difference). The results could then be improved by knowing the initial spatial distribution of velocity, temperature and concentration in the experimented case as well as by accurately knowing the heating power supplied to the fluid through the copper walls and the temperature in the vapour space.

It is also noticeable from the CFD results depicted in Table 5.4 that the simulated flow can be assimilated to a 2D flow. However, the slight delay observed in Figure 5.13 between the 3D and 2D results, is due the convective loops in both layers which are dampened by the presence of the front and back walls restricting the heat and mass transfer through the interface in the 3D model. As a result, to a smaller extent, probably due to the small dimensions of the experiment, it turns out that the 2D simulations compared to the 3D simulations, tend to overestimate the heat and mass transfers through the interface. As a consequence, it tends to accelerate the rollover occurrence and underestimate the peak of boil-off rate.

5.2.4.4 Analysis of the rollover phenomenon

From Figure 5.13 and Tables 5.3 and 5.4, it turns out that the rollover experimented by Nakano et al. can be decomposed in 2 distinct stages:

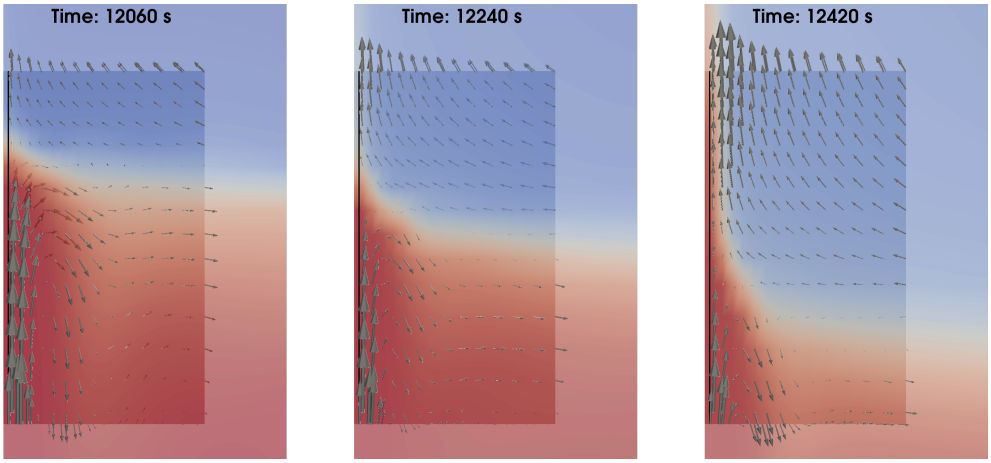

Figure 5.14: Penetration of a thin layer from the bottom layer into the upper layer (close-up in the near-wall area near the interface)

1. During the first stage called "incubation time", the interface remains in its initial position. The temperature difference between both layers grows considerably as a result of the superheating of the lower layer and contributes to the decrease in density difference between both layers. Besides, given that the lower layer is larger than the top layer, and due to the mass transfer through the interface, the concentration in the upper layer increases while the concentration in the lower layer seems unaffected. The convection cells form in both layers rising near the walls and going downwards near the centre.

2. Following the incubation time, the interface starts moving downwards slowly driven by a decreasing density difference as well as by a growing difference in entrainment rates between both layers coming from an increasing and higher temperature gradient between the heating side walls and the cooling top boundary. This can be observed in Table 5.4 where the velocity magnitude grows rapidly in the upper layer. The downward motion of the interface is accelerated until complete mixing. Meanwhile, the boil-off rate increases drastically while the temperature in the upper layer grows faster.

During the descent of the interface, the latter is pushed downwards as a result of the convective motions in the upper layer. Through this process, the interface

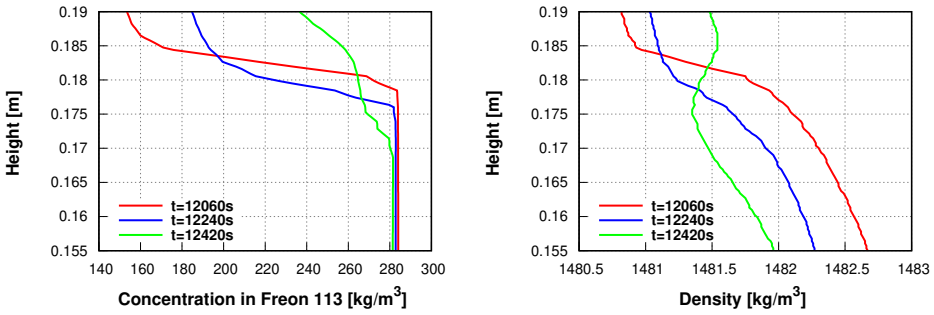

Figure 5.15: Evolution of the concentration and density profiles in the near wall area close to the interface

is distorted. A close-up of the zone right below the interface in the near-wall area shows that the liquid is almost stagnant in this area as pictured in Figure 5.14. As a result, on this side of the interface, the temperature is higher than anywhere else near the interface. In the meantime, the mass transfer between the layers through the interface also contributes to the decrease in density difference between both layers. This is illustrated in Figure 5.15, where the concentrations and density profiles are plotted along the black line in Figure 5.14. When the density difference on both side of the interface and near the walls tends to 0, the interface vanishes and convection cells from the bottom layer penetrates into the top layer. The "penetrative convection" pattern was observed 12,420 s after starting the experiment as pictured in Figures 5.14 and 5.15. At this precise moment, one can see a thin layer from the bottom layer penetrating inside the upper layer and rising near the walls due to buoyancy. This moment is captured with the density distribution near the interface in the near-wall area. Indeed, before penetration and in stable conditions, the density decreases with the height (for example at $t = 12,060s$ and $t = 12,240s$). However, one can see that at

Experimental conditions								Experimental results		CFD Results		
		Concentration in Freon 113 [wt%]		Electrical Power [W]		Initial height [mm]		Time until mixing started [min]	End of mixing time [min]	Time until the interface starts moving [min]	Time until penetration occurs [min]	End of mixing time [min]
Heating condition	*Run #*	*Upper Layer*	*Lower Layer*	*Side*	*Bottom*	*Upper Layer*	*Lower Layer*					
Side Heating	6	0.3	6.6	30	0	114	216	160	215	90	129	205
Bottom and Side Heating	8	0.6	8.4	30	12	139	206	150	170	110	133	154
	12	1.0	17.3	30	12	120	223	230	232	120	215	220
	14	1.1	17.4	30	30	128	216	125	130	120	139	149
	15	0.6	22.1	30	20	131	211	176	190	120	198	210

Table 5.5: Experimental conditions, experimental data and CFD results for "Tests 6, 8, 12, 14 and 15"

Run #	**Difference in start time**	**Difference in end time**
6	19%	4.6%
8	11%	9.4%
12	6.5%	5.2%
14	11%	15%
15	12%	11%

Table 5.6: Comparison of the simulated start and end of mixing times with the characteristic times observed by Nakano et al.[8]

the penetration time ($t = 12,420s$) because of the superheating of the lower layer, there is a location where the liquid is less dense than the layer above it generating an upward flow due to buoyancy. Finally, the penetration of the interface accelerates the heat and mass transfer between both layers and as a consequence the mixing of the layers.

5.2.5 Results of comparisons with other experimental runs

The results obtained with 2D and 3D meshes for the experiment "Test 15" were presented in Section 5.2.4 showing similar results for the evolution of temperature, concentration and density in both layers as well as for the boil-off rate and the level of the interface. The 3D results were slightly delayed (approximatively 10 min) compared to the 2D ones. However, the flow simulated in 3D turned out to be planar when considering the convective cells in the upper and lower layers as observed in Table 5.4. With the 3D mesh grid composed

of 459,000 cells, the total CPU time for the whole simulation was 2,230 hours whereas for the 2D mesh grid constituted of 15,300 cells, the total CPU time was 17 hours only. As a result, the 2D simulation has run in 130 less time than the 3D simulations while providing accurate numerical results only slightly different from the 3D results.

As a result, the numerical method with 2D mesh grids was also employed to model several other experiments conducted by Nakano et al. [8]. Experimental and numerical results are reported in Table 5.5 and comparisons of the results are provided in Table 5.6. The numerical results are in agreement with the experimental results regarding the assessed mixing time for 5 different experiments, proving to be less than 15% different from the experimented value. If the time until mixing started corresponds to the time a thin layer from the bottom layer penetrates into the top layer, the difference between the predicted time and the experimental time is also relatively small being lower than 13% for "Tests 8, 12, 14 and 15" and slightly higher for test 6 with 19% difference. The highest value of 19% is obtained for the experimental case where the enclosure is heated on the sides only so the homogenisation of the liquid is reduced compared to other cases heated both on the sides and below. As a result, the numerical results are even more sensitive to the initialisation which could be improved if more data was available.

5.2.6 Parametric studies

An interest of using CFD is the relative easiness to modify several given parameters compared to experiments. As a result, the influence of several key-parameters on the experiment "Test 15" will be investigated on 2D mesh grids and qualitative conclusions will be drawn about rollovers in general. These parameters are:

- the power of the bottom heating,

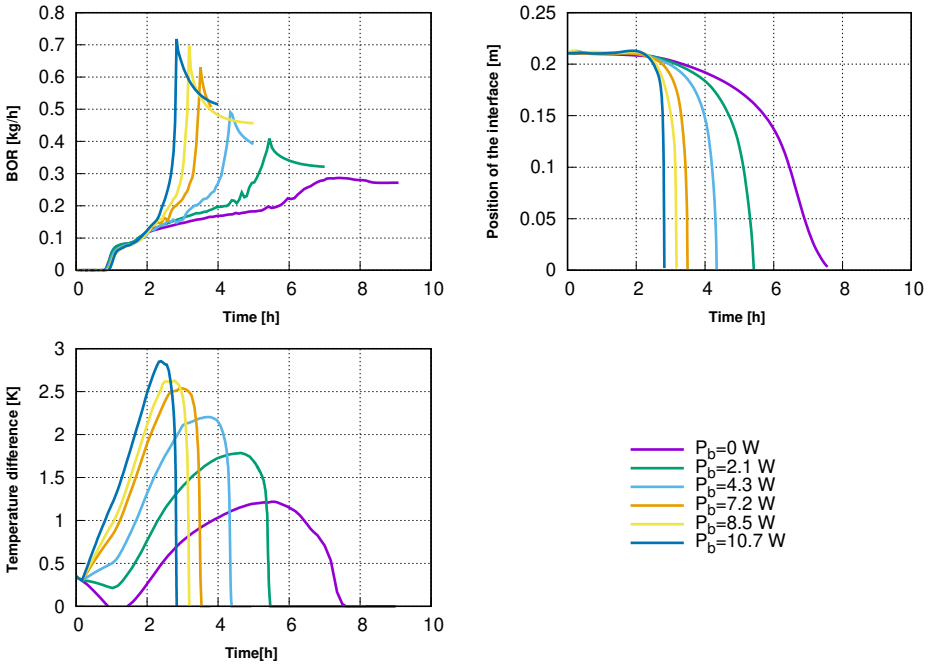

Figure 5.16: Comparisons of BOR, interface motions and temperature differences for different bottom heating rates and a constant side heating such as $P_s = 6.6$ W

- the power of the side heating,
- the initial relative layer size difference,
- the initial density difference,
- the intensity of the evaporation at the free surface.

5.2.6.1 Influence of bottom heating

In earlier studies conducted by Shi [14], Seveleder [17] or Lemembre [16], the bottom heating was considered to play a secondary role compared to the side heating. As a result, it was commonly neglected. A novelty of this work is take into account and assess the effect of the latter on rollover.

Several simulations have been carried out similarly to “Test 15” but with varying bottom heating rates in order to understand better its effects during rollover. The results are reported in Figure 5.16. One can see that the temperature difference between the lower and the upper layer grows faster and more significantly

with a more intense bottom heat flux. As a consequence, the higher the bottom heat flux is, the earlier and the more rapid the densities in both layers will tend to equalise, making the interface less stable and the penetration of a thin layer of fluid from the lower layer into the top layer near the wall more likely. Besides, with a growing bottom heat flux, the downward motion of the interface is more rapid, shortening consequently the mixing time. From the simulation results, it turns out that increasing the bottom heat flux accelerates the occurrence of the peak of boil-off rate while intensifying it. This higher maximum evaporation rate is a direct consequence of a higher supersaturated temperature defined as $T - T_{sat}$. At larger scales, such as in LNG tanks, these intensified releases would lead to potentially more hazardous scenarios if not handled carefully.

Finally, in the absence of any bottom heating (i.e. with $P_b = 0$ W), no peak of boil-off rate is observed as shown in Figure 5.16. As a consequence, it turns out that the latter cannot be neglected when studying rollover as it was done in previous studies: not only bottom heating is responsible of the superheating of the bottom layer resulting in a peak of boil-off rate but also accelerates both the rollover occurrence and the resulting mixing. These conclusions are in agreement with Morioka's observations [37].

5.2.6.2 Influence of side heating

The same set-up as in "Test 15" is used hereafter with different side heating rates in order to study their influence on rollover.

The results reported in Figure 5.17 show that increasing the side heating rate accelerates slightly the rise of the temperature difference between the lower and upper layers but their maximum value are sensibly similar. However, because increasing the side heating rate causes the average temperature of the mixture to rise, the superheated temperature is also increased and the evaporation intensified. As a consequence, after increasing the side heating rate, the interface which is driven by the difference in velocity entrainments between both layers starts

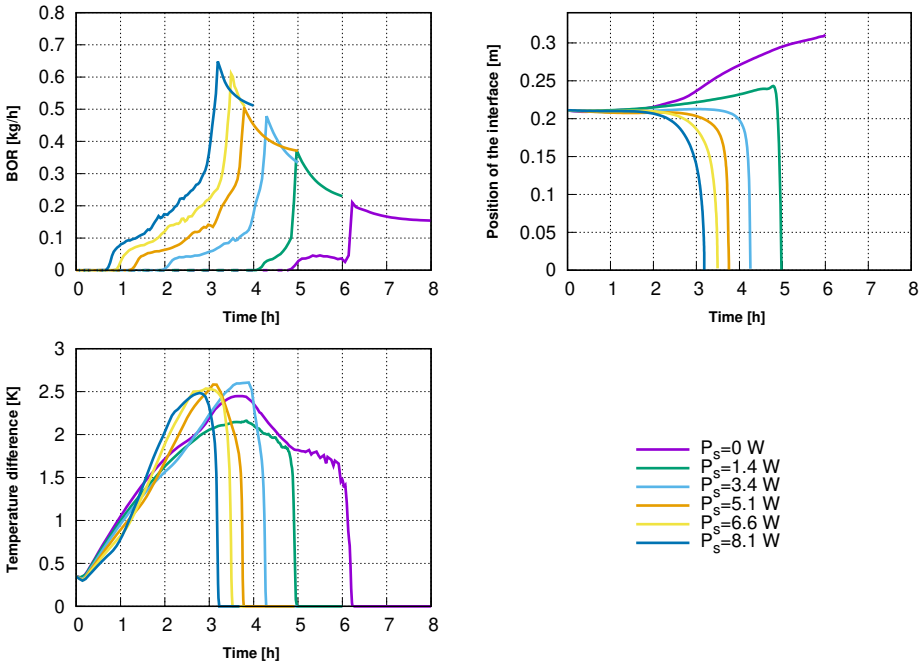

Figure 5.17: Comparisons of BOR, interface motions and temperature differences for different side heating rates and a constant bottom heating such as $P_b = 7.2$ W

migrating downwards earlier and faster as it can be seen on the same figure.

Besides, for the cases where $P_S = 0$ W, the interface was observed to move away from the heated surface similarly to what was observed by Turner [29]. The same pattern was reproduced to a lesser extent where $P_S = 1.4$ W until the entrainment velocity in the top layer started compensating the one in the lower layer finally causing the interface to move downwards.

5.2.6.3 Influence of initial relative layer size difference

The same set-up as in "Test 15" is used hereafter for the following simulations. However, different initial size are used for the upper layer while the initial size of the lower layer remains constant in order to study the influence of the initial relative layer size difference.

One can observe that increasing the initial size difference delays the penetration time as well as the end of the mixing. When the upper layer is less high than 60% of the lower layer, the higher the initial size difference, the higher the

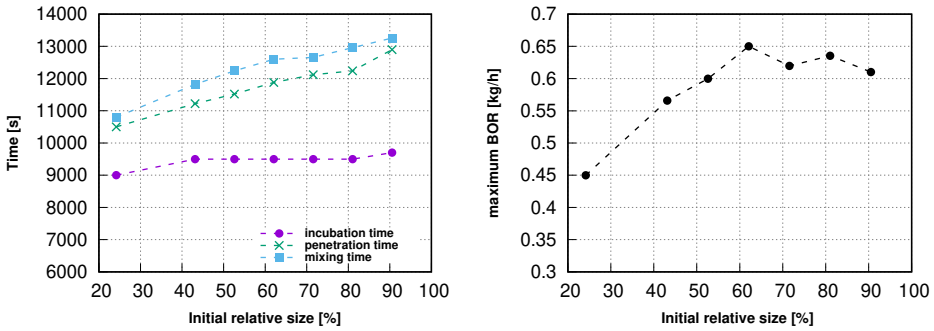

Figure 5.18: Influence of the initial relative size difference on the different characteristic times of rollover and maximum BOR

maximum boil-off rate. Above 60%, there is no clear trend. Indeed, on one hand, the saturation temperature is decreasing with an increasing upper layer since the final concentration is reduced. On the other hand, the average temperature of the upper layer is growing less rapidly since the volume of the upper layer is more significant. Although the observations are in agreement with Germeles' results [10] regarding the different characteristic times, they do not agree when concluding about the peak of boil-off rate. Germeles hence found that increasing the relative size of the upper layer tends to decrease the peak of boil-off rate. This difference may be due to the small dimensions of the experiments and the relatively high content in solute which tend to influence the saturation temperature unlike in LNG storage tanks where it can be assumed constant.

5.2.6.4 Influence of initial density difference

"Test 15" is taken as a reference for the following simulations. The initial density difference between the layers is modified from one case to another by changing the initial concentration difference. This aims at assessing the influence of the initial density difference on the rollover phenomenon.

One can observe from Figure 5.19 that increasing the initial density difference delays both the penetration time and the end of the mixing and lengthens the incubation time. Consequently, it promotes the rise of the liquid average tem-

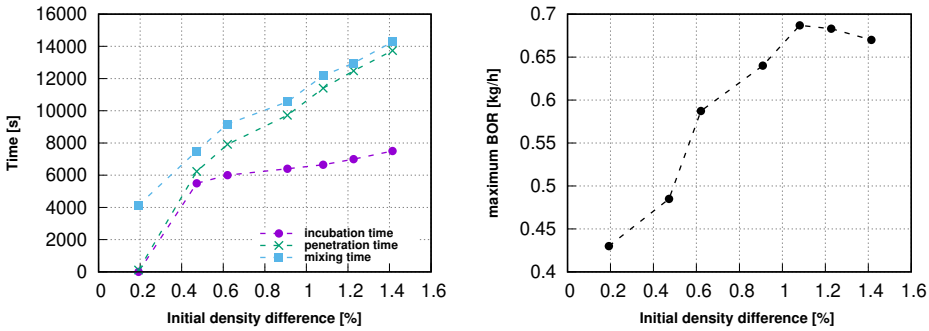

Figure 5.19: Influence of the initial density difference on the different characteristic times of rollover and maximum BOR

perature, as the liquid is heated at the same rate, but during a longer incubation time when the evaporation rate is reduced. Besides, for relatively low initial density difference (less than 1%), increasing the initial density difference tends to increase the peak of boil-off rate. Above 1%, the latter starts to decrease. This can be explained by the fact that the peak of boil-off rate is reached during the last stage of the mixing when the concentration is nearly homogeneous within the tank. By increasing the initial concentration to increase the initial density difference, the final concentration (i.e. reached after the rollover) is also increased and, as expressed in Equation 5.1, so is the saturation temperature just before the end of the mixing. As a result, beyond an initial density difference of 1% for a mixture of Freon, the increase in saturation temperature being more significant than the increase in average temperature, according to Equation 3.72, the peak of boil-off rate is then decreased when increasing the initial density difference. Moreover, it can be observed that for relatively small density differences ($\approx 0.2\%$ or less), the penetration of a lower layer inside the top layer occurs instantaneously.

5.2.6.5 Influence of the top boundary condition

In the following section, the influence of the evaporation rate is investigated. As identified in Equation 3.72, the heat flux, denoted q, can be written as:

$$q = A(T_{bulk} - T_{sat})^{4/3} \tag{5.13}$$

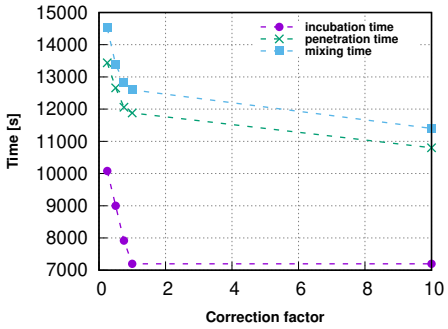

Figure 5.20: Influence of the top boundary condition on the rollover phenomenon

with $A = C\frac{\lambda}{L}\left(\frac{\beta_T g}{\alpha\nu}\right)^{1/3}$.

In this chapter, a correction factor α_{corr}, varying between 0 and 10, is introduced to take into account the influence of the evaporation rate on the rollover. This approach aims at understanding the effect of the evaporation on the rollover while assessing the sensitivity of the numerical results on the adopted boundary condition. Indeed, the boundary condition based on Hashemi-Wesson relation requires the definition of the saturation temperature which may be complex and bring some errors.

One can observe from Figure 5.20 that increasing the intensity of the evaporative boundary condition reduces the incubation time and accelerates the penetration of the fluid from the lower layer into the upper layer. This is the result of the intensified cooling due to a higher evaporation. The density of the upper layer increases faster and as a result, the density difference between the layers is also reduced faster. As a result, the penetration of a layer from the bottom layer occurs earlier and the mixing time is reduced.

5.2.7 Conclusion

Nakano et al. [8] have conducted several rollover experimental studies with a mixture of Freon 11 and Freon 113. In their article [8], “Test 15” was reported comprehensively and has served to validate the numerical method presented in

this thesis. The 2D and 3D predictions have shown relatively good agreements for the temperatures, concentrations and densities in the upper and lower layer but also the migration of the interface. The simulated boil-off rate also follows the same trend as the experimented one and the simulated peak in boil-off rate is close to the experimented one (the observed peak in BOR was 0.8 kg/h while the simulated one was approximatively 0.7 kg/h).

The CFD model gave some insights into the rollover phenomenon which, in this case, turns out to be driven by a downward motion of the interface followed by the penetration of the interface by a layer of fluid from the lower layer into the upper layer.

Besides, several other experiments, although less comprehensively reported in the article, were simulated in 2D given the significant gain in calculation time and the small difference between 3D and 2D results observed for test15. The numerical results are in acceptable agreements with the experimental data showing less than 19% difference. Finally, "Test 15" served as a basis for several parametric studies to assess the influence of several parameters on the phenomenon. From this analysis, the main results were:

- With no bottom heating as assumed by previous researchers [17, 14, 16, 15], the superheating of the lower layer is limited as well as the boil-off rate. Increasing the bottom heating accelerates the rollover occurrence and causes higher peak of boil-off rate.

- Increasing the side heating has turned out to increase the boil-off rate unlike Germeles' numerical results [10] with LNG. This result is probably due to the small dimensions of the experiment and the liquid properties. Nonetheless, similarly to Germeles' result [10], increasing the side heating accelerates the rollover occurrence.

- Increasing the size of the upper layer compared to the lower layer or the initial density difference has shown to slow the rollover process down.

- Increasing the evaporation rate significantly speeds up the rollover phenomenon which justifies that extra care is taken to model the surface evaporation.

Although, this analysis was conducted on small-scale test cases, these observations are generally also applicable to large-scale LNG rollovers except regarding the influence of the side heating on the boil-off rate as explained hereabove.

5.3 LNG rollovers

As mentioned in Chapter 2, LNG are multicomponent mixtures made principally of methane and include fewer amounts of ethane, propane, butane, pentane and nitrogen. In Chapter 3, the presented equations were presented in a way that they could be applicable to one or more solutes. In the previous sections of this chapter, the code was used to model and simulate rollovers in binary mixtures and have shown satisfactory agreements with both numerical and experimental results. In the following section, the code, rolloverFoam, is slightly modified to extend its application to multicomponent mixtures. In addition, it takes into account a transport equation for each considered solute and the LNG density is calculated with a different method. Indeed, instead of using a linear approximation as it was done previously with binary mixtures, it is based on the Klosek-McKinley method [80] which is empirical but has proven to be accurate for most LNGs. This will be the first part of this section. Further, the numerical approach will be used to model the rollover experimented by several gas companies in Nantes [82] as well as the well-known La Spezia incident [6]. The results will be presented and analysed to provide additional insights into the rollover phenomenon. Finally, given the recent rise of FLNG tanks and LNG bunkering, the code is employed to simulate a rollover in a medium-scale FLNG tank.

5.3.1 LNG properties

5.3.1.1 LNG density calculation

The LNG density is calculated using the revised Klosek-McKinley method [80]. The accuracy of this method has proven to be ± 0.1% for an LNG mixture with the following properties:

- $x_{CH_4} > 60\%$ mol
- $x_{C_4H_10} < 4\%$ mol
- $x_{C_5H_{12}} < 5\%$ mol
- $x_{N_2} < 5\%$ mol
- -180 °C $\leq T \leq$ -140°C
- $M_{LNG} < 20$ kg·kmol^{-1}

As a result, this method has the advantage to be valid for most of the LNG produced worldwide. The liquid density at a given temperature T [°C] is calculated as follows:

$$\rho_T = \frac{\Sigma x_i M_i}{\Sigma(x_i V_i) - V_C} \tag{5.14}$$

where the numerator is the LNG average molecular mass and the denominator is the volume taking into account the reduction in volume V_C obtained when mixing the components at T [°C]. The parameter V_C is calculated with the following equation:

$$V_C = \left[k_1 + (k_2 - k_1)\frac{x_2}{0.00425}\right] x_1 \tag{5.15}$$

where k_1 and k_2 are two correction factors in kmol, accounting respectively for, the presence of hydrocarbons and nitrogen. k_1 and k_2 are obtained by linear interpolation from the tables provided in Appendix E.

5.3.1.2 LNG physical properties

Since LNG is mainly made of methane, its saturation temperature is assumed to be constant over the small variations of its composition occurring during the

Parameter	Considered value	Parameter	Considered value
$\alpha\,[m^2/s]$	$1.25\,10^{-7}$	$D_{N_2}\,[m^2/s]$	$2.29\,10^{-9}$
$D_{C_2H_6}\,[m^2/s]$	$2.27\,10^{-9}$	$\nu\,[m^2/s]$	$2.75\,10^{-7}$
$D_{C_3H_8}\,[m^2/s]$	$1.92\,10^{-9}$	$\beta_T\,[K^{-1}]$	$3.12\,10^{-3}$
$D_{C_4H_10}\,[m^2/s]$	$1.67\,10^{-9}$	$\lambda\,[W/(m.s)]$	0.2
$L\,[kJ/kg]$	511		

Table 5.7: Properties of LNG

rollover phenomenon. In the following simulations, the saturation temperature is calculated from Hashemi-Wesson relation [33] considering the actual initial boil-off rate.

The viscosity as well as the thermal conductivity, thermal diffusivity and thermal expansion coefficient used to characterise LNG are assumed constant over the relatively small variations of temperature and composition of the LNG solution. These values are obtained from those of a pure solution of methane at 111 K from the NIST Chemistry Webbook [81]. Besides, regarding the mass diffusion coefficients for ethane, butane, propane and nitrogen, they are calculated from Wilke and Chang [54] presented in Section 3.1.4.1. The physical parameters considered to model LNG are summarised in Table 5.7.

5.3.2 Numerical set-up

Given the large dimensions of LNG tanks, turbulence plays an important role in the mixing process involved during rollover. This can be illustrated with the modified Rayleigh number Ra^*, which exceeds 10^{13} for liquid already higher than a meter. As a consequence, the fluid flow cannot be assimilated to a 2D flow and 3D models are needed to simulate accurately the hydrodynamics involved during the rollover phenomenon.

5.3.2.1 Boundary conditions and initialisation

Similarly to the study with Freon presented in Section 5.2, the model focuses on the liquid part. The walls of the tank containing the LNG are impermeable

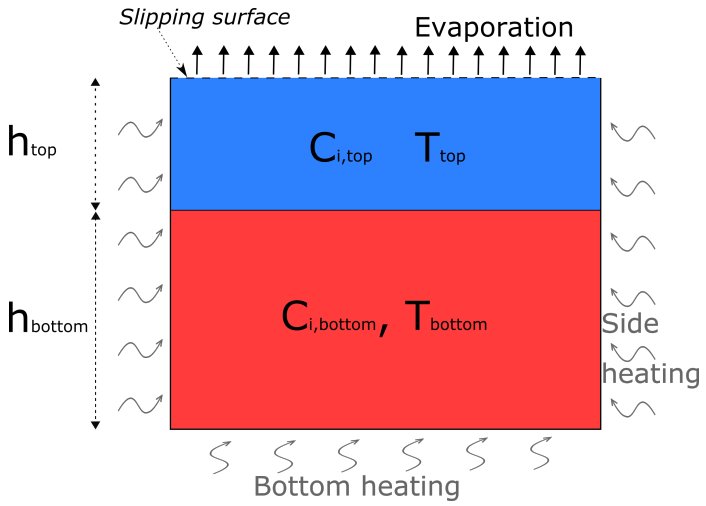

Figure 5.21: Section view of the numerical set-up [22]

and, due to the heat ingress through the walls, they provide a constant heat flux to the liquid. Besides, the surface in contact with the vapour is a free surface where evaporation takes place. The liquid warming, due to the hot vapour located above it, is neglected given that the order of magnitude is significantly lower than the evaporative heat flux. Indeed, following Hashemi-Wesson relation the LNG evaporative heat flux is such as $q_{ev} \approx 650\,(T_{bulk} - T_{sat}^{4/3})$ while, for example, in La Spezia case if all the heat transmitted to the vapour is transferred to the liquid then the resulting heat flux would be such as $q_{vl} = 18$ W·m^{-2}. This means that, once the temperature difference $T_{bulk} - T_{sat}$ exceeds 0.06 K, the warming effects are compensated by the evaporative heat flux.

The numerical boundary conditions for the temperature, the concentration of the different components of LNG as well as for velocity, developed in Section 3.4 and illustrated in Figure 5.21 can be summarised as follows:

- At the side walls:

$$\boldsymbol{U} = \boldsymbol{0} \tag{5.16}$$

$$\nabla C_i.\boldsymbol{n} = 0 \tag{5.17}$$

$$\nabla T.\boldsymbol{n} = \frac{q_s}{\lambda_{eff}} \tag{5.18}$$

- At the bottom wall:

$$\boldsymbol{U} = \boldsymbol{0} \tag{5.19}$$

$$\nabla C_i.\boldsymbol{n} = 0 \tag{5.20}$$

$$\nabla T.\boldsymbol{n} = \frac{q_b}{\lambda_{eff}} \tag{5.21}$$

- At the free surface:

$$\boldsymbol{U}.\boldsymbol{n} = U_z = 0 \tag{5.22}$$

and

$$\frac{\partial U_x}{\partial z} = 0 \quad and \quad \frac{\partial U_y}{\partial z} = 0 \tag{5.23}$$

$$\nabla C_i.\boldsymbol{n} = 0 \tag{5.24}$$

$$\nabla T.\boldsymbol{n} = \frac{q_{ev}}{\lambda_{eff}} \tag{5.25}$$

where q_{ev} is defined following the explanations given in Section 3.3 as:

$$q_{ev} = \begin{cases} 0, & \text{if } T_{bulk} < T_{sat} \\ C_m \lambda \left(\frac{\beta_T g}{\alpha \nu} \right)^{1/3} (T_{bulk} - T_{sat})^{4/3}, & \text{if } T_{bulk} \geq T_{sat} \end{cases} \tag{5.26}$$

with T_{bulk} the average temperature in the upper layer and T_{sat} the saturation temperature.

The flow in the near-wall area is modelled via wall-functions. The selected mesh grids verify that the first cells are located in the logarithmic area with y^+ values comprised between 30 and 500.

Regarding the initialisation of the cases studied hereafter, an initially strong stratification is assumed. Then, let h_{bot} be the size of the lower layer and z a given height above the tank bottom. If $z > h_{bot}$ then:

$$T = T_{top} \text{ and } C_i = C^0_{i,top} \tag{5.27}$$

Otherwise, if $0 \leq z < h_{bot}$, then:

$$T = T_{bot} \text{ and } C_i = C^0_{i,bot} \tag{5.28}$$

5.3.2.2 Numerical schemes

The transient terms in the considered equations are discretised following the Euler implicit method, while first-order upwind schemes are used for the convective terms in order to ensure stability. As for the gradient terms, they are discretised with central differencing schemes.

5.3.3 Simulation of Nantes experiment

Between 1987 and 1990, several gas companies conducted some LNG rollover in a medium-scale reservoir. Indeed, the 500 m^3 cylindrical tank (diameter x height: 8.5 m x 8 m) is smaller than standard tanks with volumes between 40,000 m^3 and 200,000 m^3. However, rollovers and turbulence — given that the latter is already important for liquid higher than a meter — can be experimented. The results obtained from this experiment were partially published by Gorieu [82], Bates and Morrison [84], Seveleder [17] and Lemembre [16].

5.3.3.1 Initial conditions and model

The measured heat leakage rate through the side and bottom walls are respectively 10 $W{\cdot}m^{-2}$ and 15 $W{\cdot}m^{-2}$ [17]. The actual stratification obtained during the experiment was constituted of two main layers — the upper and lower ones — as well as an intermediate layer, considerably smaller than the other two. The initial stratification, illustrated in Figure 5.21, is then simplified to a two-layer stratified liquid. Besides, the LNG composition was then calculated from the temperature and densities provided by Bates and Morrison [84] as well as from the methane concentration reported in Lemembre's thesis [16]. The properties of

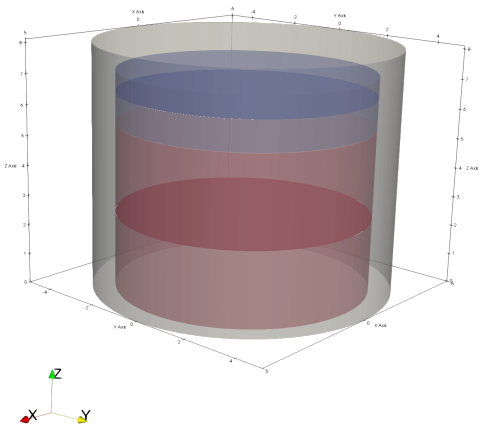

Figure 5.22: Presentation of the experimental set-up and probe locations (planes at z=2 m and z=6.5 m)

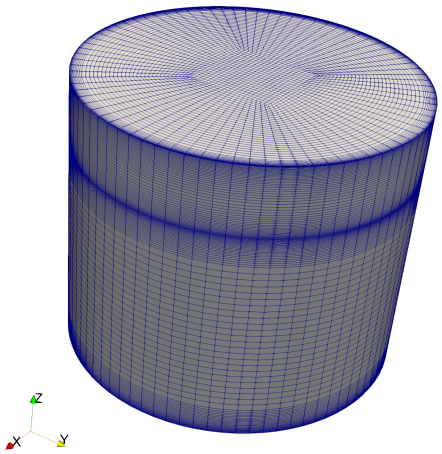

Figure 5.23: Mesh grid used to model Nantes experiment

the layers considered in the numerical model are summarised in Table 5.8.

5.3.3.2 Comparisons of the numerical results with the experimental data

During the experiment, probes, located 2 meters and 6.5 meters above the tank bottom, were monitoring the temperatures, densities and methane concentration. The exact positions of the probes is not known. As a result, it has been

	Bottom Layer	***Top Layer***
Layer Height [m]	5.5	1.7
Composition [% mol]		
Methane	85	87.75
Ethane	13.3	10.564
Propane	1.2	1.19
Nitrogen	0.5	0.496
Temperature [K]	114.5	113.65
Density [kg/m^3]	463	457

Table 5.8: Physical characteristics of the initial stratification considered in the numerical model

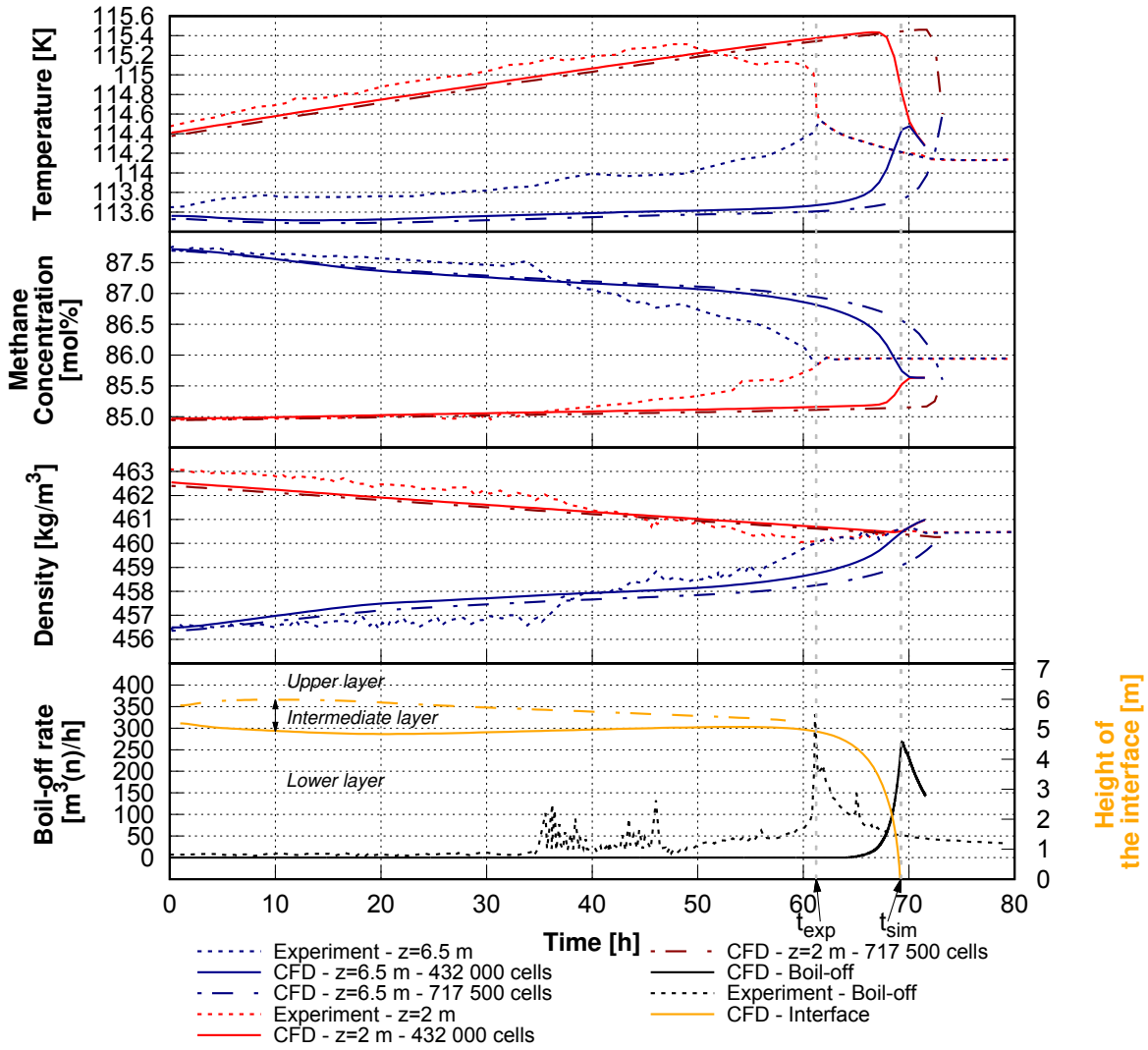

Figure 5.24: Comparison of the numerical results with the experimental data obtained during Nantes rollover experiment [22]

decided to consider the temperatures, densities and methane concentrations averaged over the planes located in the lower layer at z=2 m (highlighted in red in Figure 5.22) and in the upper layer at z=6.5 m (highlighted in blue in Figure 5.22). The experimental and numerical results are reported in Figure 5.24.

First, a mesh sensitivity study was conducted. Two meshes, a finer and a coarser grid, constituted of, respectively, 715,000 and 432,000 hexahedral cells were tested. As it can be observed in Figure 5.24, the results are close and the relative difference of predicted rollover time is less than 6%, while the simulation with the finer mesh has run twice longer than the one with the coarser mesh (the total CPU time is 12,300 hours against 5,560 hours for the coarser mesh). As a result, the coarser mesh grid was selected as an acceptable trade-off between accuracy and calculation time.

It turns out that the numerical predictions are satisfactory, predicting the sudden mixing and the resulting peak of boil-off rate only 6 hours later than in the experiment. As far as the peak in boil-off rate is concerned, the simulated one is slightly underestimated compared to the experimented peak, predicting 260 m^3(n)/h against the experimented 310 m^3(n)/h. However, quantitatively and qualitatively, the predicted temperatures, methane concentrations and densities in both layers as well as the boil-off rate are in agreement with the experimental data.

Besides, the calculated Reynolds number, being of the order of 10^5 justifies the use of a turbulent model to simulate Nantes experiment.

5.3.3.3 Analysis of the rollover phenomenon

In light of Figure 5.24, two different stages can be identified similarly to Bates and Morrison's observations [84]. Indeed, the first stage which corresponds to the "incubation stage" and starts from the beginning of the experiment lasts 62 hours. It is characterised by a stationary interface and is followed by a second stage, the "migration stage" during which the interface migrates downwards until complete

mixing of the layers.

5.3.3.3.1 Analysis of the incubation stage

From Figure 5.24, where experimental and numerical results are represented, several observations can be made regarding the phase prior to the interface migration:

- The temperature in the upper layer seems unaffected during the period prior to the interface migration. This is the result of the heat released during the evaporation process which tends to compensate the reduced heat flux from the lower layer and the heat ingress through the side walls. On the contrary, the temperature in the lower layer grows quickly as a consequence of the superheating.

- Given the large dimension of the lower layer compared to the upper one, the concentration of the upper layer is more sensible to the mass transport through the interface. As a result, although the methane molar fraction is increased slightly (from 85% initially to 85.2% after 62 hours) in the lower layer, the effects on the methane molar fraction in the upper layer are more visible since, they are reduced from 87.7% initially present to 86.6% after 62 hours.

- On the one hand, the increase in temperature in the lower layer reduces the density of the layer while on the other hand, as a result of the decrease in methane concentration in the upper layer (which is the lightest component in LNG), the density of the upper layer is increased. As a consequence, the density difference between the layers is reduced from 6 kg/m^3 initially to 2 kg/m^3 approximately after 62 hours.

- During the incubation stage, the evaporation is almost unaffected due to the temperature of the layer of fluid located below the free surface remaining constant during this same period.

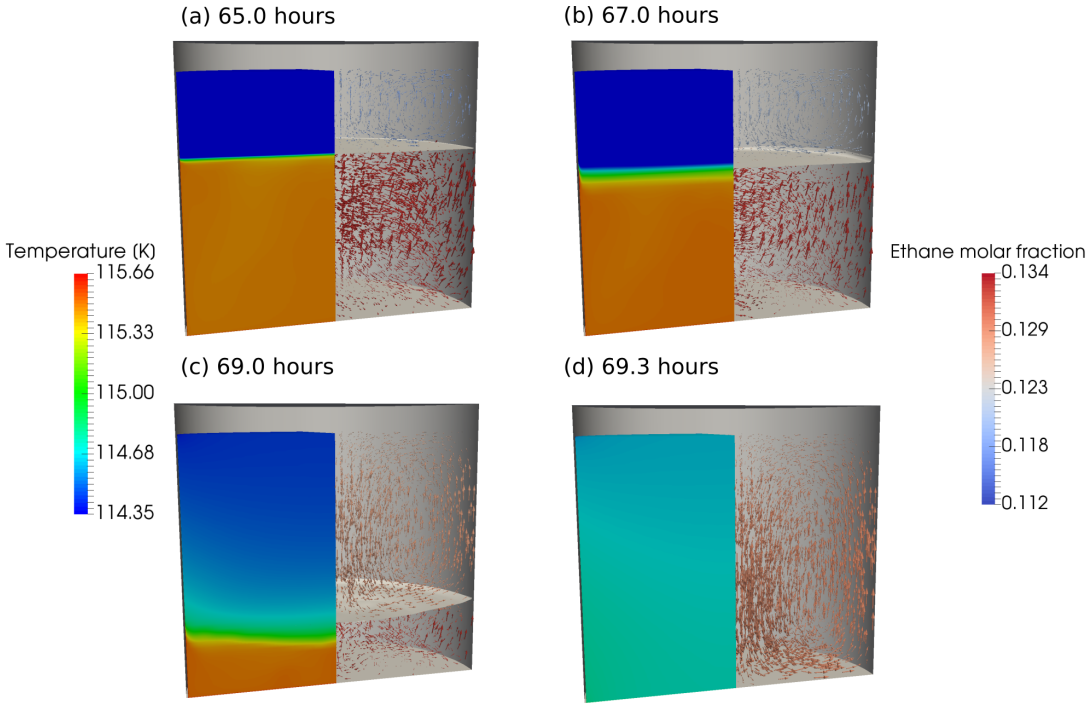

Figure 5.25: 3D representation of the simulated rollover experiment [22]. The tank is cut in half showing the temperature (on the left-hand side) and simultaneously the velocity fields and the ethane molar fractions (on the right-hand side) within the LNG tank after 65 hours (a), 67 hours (b) 68 hours (c) and 69.3 hours (d). The interface is highlighted in grey on the right-hand side.

- It can be observed that due to the initial low entrainment rate in the upper layer, an intermediary layer has rapidly formed growing during the 20 hours following the beginning of the experiment. Then, due to the growing evaporation, the convection cells are intensified in the upper layer. The latter coupled to the reducing in density difference between the layer forces the intermediary starts to shrink, finally forming after 62 hours a sharp interface between the upper and lower layer.

5.3.3.3.2 Analysis of the migration stage

The second stage of the rollover phenomenon is the interface migration which is considerably faster than the incubation stage. Indeed, from the simulations and as depicted in Figure 5.24, it has been determined that this stage last only 8 hours during the 69 hour-long simulated rollover experiment.

The 3D results obtained with CFD, giving some insights into the rollover phenomenon, are reported in Figure 5.25. For the sake of clarity, the tank and the LNG is cut in half and are shown at different times during the interface migration. On the left-hand side, one can observe the temperature field, while on the right-hand side, the velocity is represented with arrows with a size proportional to the velocity magnitude. The layers can then be visualised more conveniently thanks to the colour of the arrows which represents the ethane molar fraction as well as with the interface highlighted in grey. One can observe that after 65 hours the convection cells are rising along the walls where the fluid is heated and are plunging further near the centre due to cooling following evaporation in the upper layer or due to a colder top layer. One can also observe 3D flows in the lower layer which justifies the use of 3D models. As expected, the temperatures and concentrations are homogeneous for a given layer.

In light of Figures 5.24 and 5.25, it can be inferred that the rollover phenomenon is the result of the downward motion of the interface separating both layers . Besides, this plunging motion is accelerating as a result of the growing entrainment rate in the upper layer due to a growing evaporation rate as well as a reduced density difference between the layers. This is illustrated by the growing size of the velocity vectors in the upper layer in Figure 5.25. Finally after 6 hours of downward motion, the interface reaches the tank bottom and the liquid is homogeneous. During the descent of the interface, the upper layer becomes warmer due to the increased mixing between the layers. As a result, the temperature of the fluid located below the interface is increased from 113.7 K after 62 hours to 114.4 K and so is the boil-off rate which has risen drastically from no boil-off rate to a maximum of 262 $m^3(n)\cdot h^{-1}$ in 6 hours. Finally, once the liquid is homogenised, the extra heat coming from the lower layer is rapidly released decreasing the boil-off rate.

This stage of the rollover phenomenon is hazardous because of its rapidity and because of the sudden evaporation generated once the interface reaches the

	Bottom Layer	***Top Layer***
Layer Height [m]	17.86	5
Composition [%mol]		
Methane	62.26	63.62
Ethane	21.85	24.16
Propane	12.66	9.36
Butane	3.14	2.35
Pentane	0.07	0.16
Nitrogen	0.02	0.35
Temperature [K]	119.82	114.82
Calculated density [kg/m^3]	539.6	536.0

Table 5.9: Physical characteristics of the layers involved during La Spezia incident and considered in the simulation

tank bottom. In practical, it would actually be too late to use mechanical mixing at this stage so as to break the interface because the heat accumulated in the lower layer during the descent of the interface is negligible compared to the total heat accumulated during the entire phenomenon.

5.3.4 Simulation of La Spezia incident

5.3.4.1 Simulation conditions and model

La Spezia incident has been previously described in Chapter 2. This rollover incident, which is the most known among the LNG industry, was caused after bottom-filling a denser cargo below a lighter heel. 30 hours after the filling had started, the pressure suddenly rose in the 49-meter diameter LNG tank. As a consequence, almost 186 tons of Natural Gas were vented out in less than 16 hours.

The numerical approach developed, within the frame of this thesis, is applied to this incident. The initial temperatures of the upper and lower layers are obtained from Sarsten's report [6]. Regarding the composition, it is assumed that due to the slow loading, the heel and the cargo have not mixed and has lead to a strong stratification. The properties of the simulated layers are summarised in Table 5.9. As far as the heat leakage rate is concerned, the flux through the

bottom wall and through the side walls are respectively 20.82 W/m^2 and 6.94 W/m^2 [11].

The mesh selected for this study, after some preliminary sensitivity analyses, is made of 900,000 hexahedrons. Similarly to the mesh used to model the rollover experiment conducted in Nantes, the mesh is refined near the walls, near the interface between the layers and near the free surface. Besides, y^+ values are comprised between 30 and 300.

5.3.4.2 Comparisons of the numerical results with the experimental data

During the initial stage of rollover, the layers are widely homogenised due to the motion of the convection cells. As a result, the values given hereafter are the layer-averaged values which are representative of the flow in each layer.

The predicted temperatures, compositions, and densities averaged over the upper and lower layers during the rollover phenomenon are presented in Figure 5.26. One can also observe the position of the interface as a function of time as well as the incidental and numerical boil-off rates. Given that, during the incident, the safety valves were opened to reduce the overpressure within the tank, the peak of boil-off rate could not be monitored.

The numerical results are satisfactory given that the predicted rollover time is overestimated by only 6 hours or 12.5% and the predicted boil-off rates follow the same trend as the experimented one. Besides, the predicted peak of boil-off rate is of the same order of magnitude as the experimented one.

The time reference, in this study, is the beginning of the loading, which corresponds to the moment the boil-off rate started to be monitored. The numerical approach developed within the frame of this thesis, starts from the stratified liquid obtained once the loading finishes i.e. 12 hours after it started.

Besides, in Figure 5.27, the changes in average velocity in the upper and lower layers during the rollover phenomenon are demonstrated. The derived Reynolds

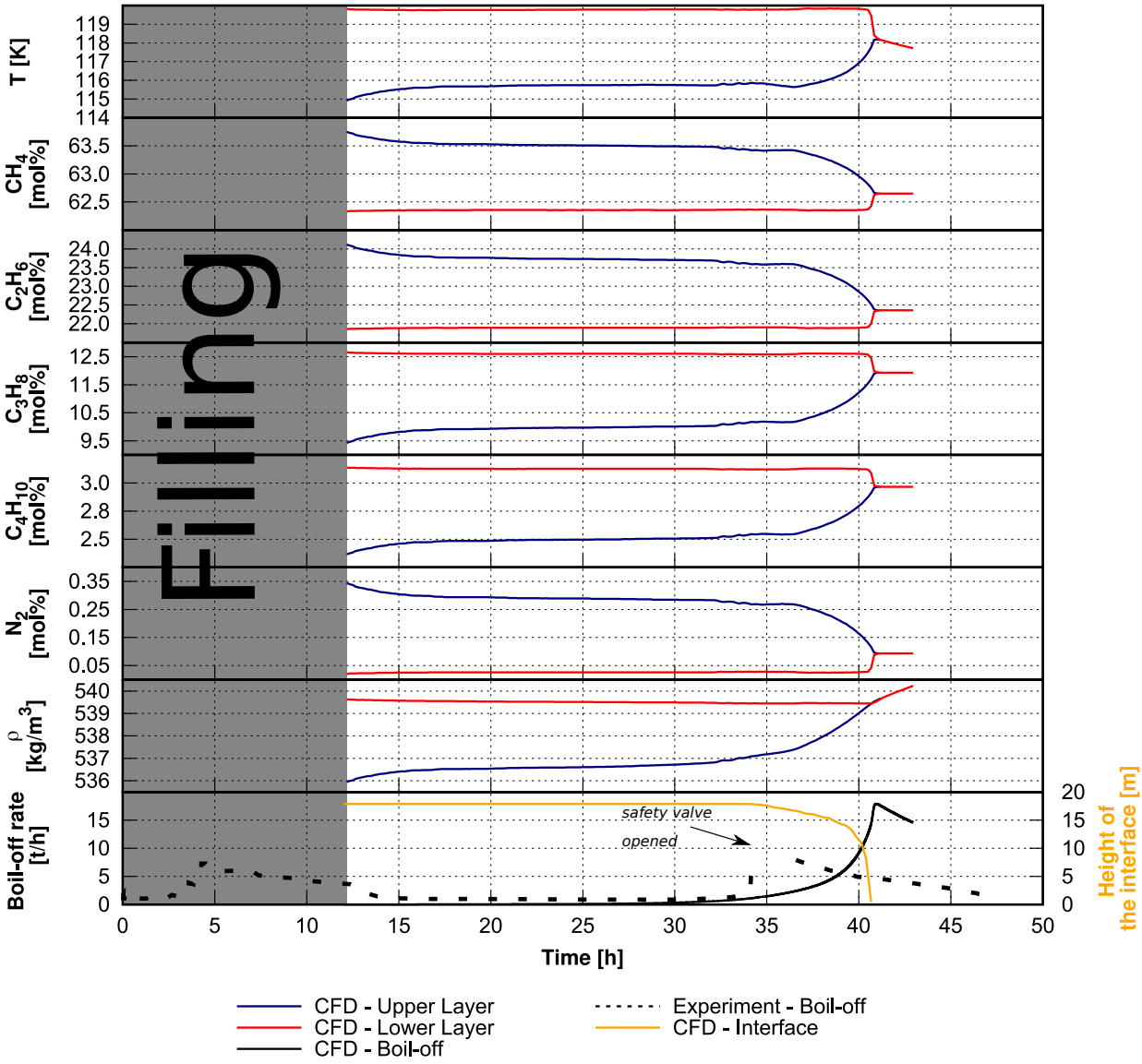

Figure 5.26: Comparison of the numerical results with the data obtained during La Spezia incident

number being of the order of 10^6 confirms the use of a turbulent model to simulate the flow.

5.3.4.3 Analysis of the rollover phenomenon

Similarly to Nantes experiment, the simulations of La Spezia incident highlights that the rollover phenomenon is composed of two stages:

- a first stage corresponding to the incubation stage, during which the interface is stationary starting from the initial stratification until 34 hours after

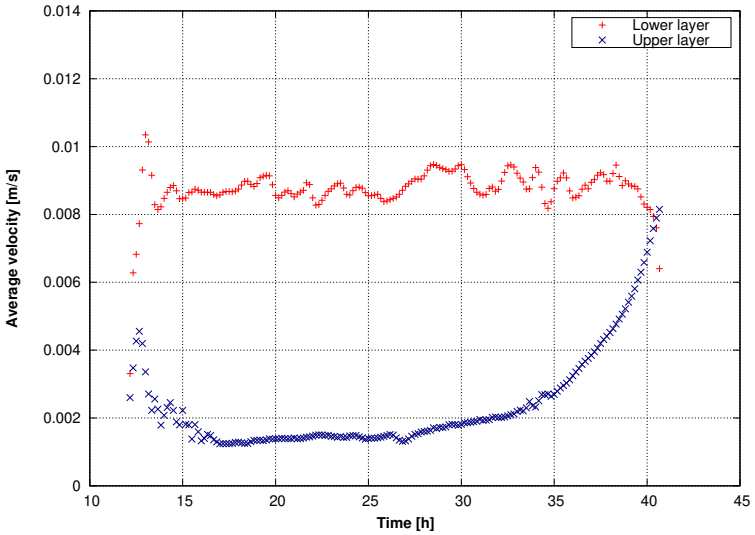

Figure 5.27: Change in average velocity in the upper and lower layers

the loading started,

- a second stage corresponding to the migration stage, during which the interface migrates downwards until complete mixing.

5.3.4.3.1 Analysis of the incubation stage

From Figure 5.26, one can observe that:

- The temperature, composition and density of the lower layer, which is considerably higher than the upper layer (17.86 m against 5 m), do not vary during this stage, although heat and mass transfer occurs through the interface.

- The temperature of the upper layer increases (from 114.82 K after 12 hours to 115.9 K after 34 hours), as well as the molar fractions of propane and butane. On the contrary, the molar fractions of ethane and nitrogen of the upper layer are reduced. The result of the overall heat and mass transfer budget is the increase of the density of the upper layer which has risen from 536 kg/m^3 after 12 hours to 537 kg/m^3 after 34 hours.

- The boil-off rate during this stage is unaffected at first since despite the increase of the temperature of the upper layer, the latter remained lower

than the saturation temperature. However, the boil-off rate is increasing during the final hours of this stage.

During this stage, the reduction of the density difference between the layers is due to the overall interfacial heat and mass transfers budget. Indeed, the increase of temperature and the reduction of nitrogen and ethane molar fractions, alone, should have cause the density of the upper layer to decrease. However, the latter increased as a result of higher contributions from the propane and butane molar fractions. Accumulations of relatively small contributions have then reduced the density difference. On the other hand, the increasing boil-off rate at the end of the incubation stage, intensifies the convection cells in the upper layer as highlighted in Figure 5.27. Consequently, the entrainment rate in the upper layer is increased partly accelerating the occurrence of the migration stage.

Besides, the superheating of the bottom layer observed during the rollover experiment conducted in Nantes and the simulation presented in Section 5.3.3 is non-existent in this case.

5.3.4.3.2 Analysis of the migration stage

During the incubation stage, the initial density difference is reduced, the relative density difference at the beginning of migration stage, being lower than 0.5%, and the entrainment rate in the upper layer is increased as a result of the increased boil-off rate. The combination of these two phenomena have contributed to trigger, after 34 hours, the interface migration which constitutes the second stage of the rollover phenomenon.

From Figures 5.26, 5.27 and 5.28, several observations can be made:

- After 34 hours, and in less than 7 hours, the interface moves downwards increasingly faster until it reaches the tank bottom as illustrated in Figure 5.28.

- The lower layer shrinks but its temperature, composition and density do

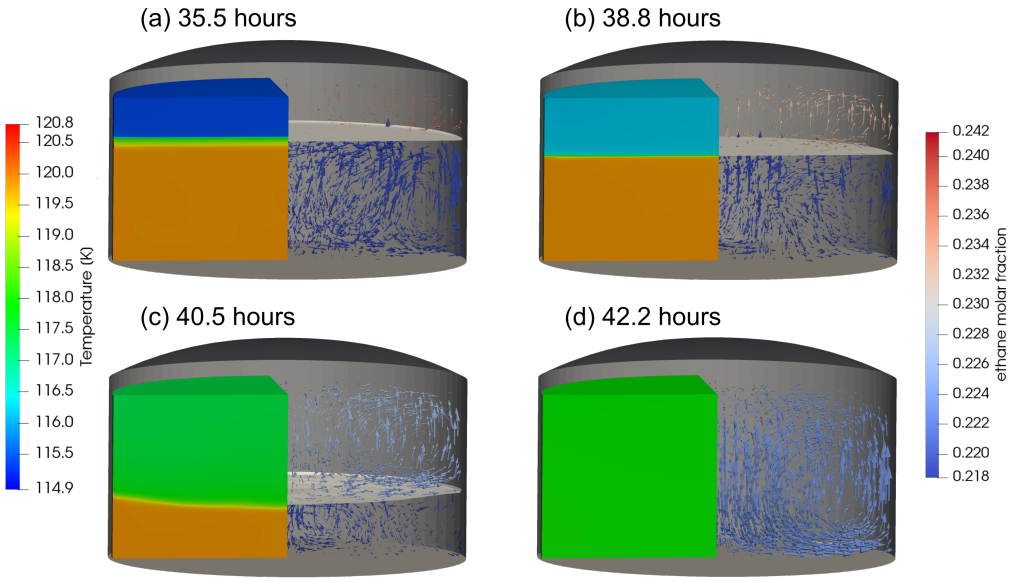

Figure 5.28: 3D representation of the simulated La Spezia incident [22]. The tank is cut in half showing the temperature (on the left-hand side) and simultaneously the velocity fields and ethane molar fraction (on the right-hand side) within the LNG tank after 35.5 hours (a), 38.8 hours (b) 40.5 hours (c) and 42.2 hours (d). The interface is highlighted on the right-hand side.

not vary until it disappears once the interface reaches the tank bottom.

- The convections cells in the upper layer are intensified during the descent of the interface. Indeed, as highlighted in Figure 5.27, the average velocity in the upper layer, which is representative of the intensity of the convective cells, is significantly increased during the migration stage from 0.0022 $m{\cdot}s^{-1}$ to 0.0082 $m{\cdot}s^{-1}$ when the liquid is completely mixed. Besides, during the descent of the interface, the convective cells in the lower layer are slighly weakened as it can be seen on Figure 5.27. One of the reason is the growing flow in the opposite direction of the other side of the interface (in the upper layer) which tends to slow down the convective cells in the lower layer.

- As depicted in Figure 5.26, the temperature of the upper layer increases significantly faster during the descent. Similarly, the mass diffusion through the interface between the layers is intensified as the interface plunges contributing to homogenise both layers. Consequently, the ethane, methane

and nitrogen molar fractions decreases in the upper layer while the butane and propane molar fractions increases. The combination of the homogenisation of the layers and the decreasing temperature difference result in the reduction of the density difference.

- In the meantime, the boil-off increases drastically from 1,000 tons/h to 17,000 tons/hour at its peak once the interface disappears, after 41 hours.

From these observations, it can be concluded that the mixing occurring during La Spezia rollover is the result of the descent of the interface caused both by a growing entrainment rate and a reduced density difference. During the descent, the heat and mass transfers though the interface are intensified, increasing the evaporation rate and consequently the entrainment rate in the upper layer while decreasing the density difference between the layers. In return, the migration is accelerated, intensifying again the heat and mass transfers through the interface, reducing the density difference. As a result, the boil-off rate grows increasing the entrainment rate, finally forming a vicious circle until the interface disappears.

5.3.5 Application to a FLNG tank

The recent trend among the LNG industry is towards the expansion of the FLNG fleet and FSRUs. However, the current loading process involved within FSRU, which consists in loading LNG in partially filled tanks, promotes stratification and, as a consequence, could lead to rollovers [5]. Besides, according to SIGTTO [27], it used to be thought that rollovers were unlikely onboard Moss type carrier because mixing would be promoted by the spherical shape and the vessel and sea motions. However, as described in Section 2.3.4.3, a rollover was finally reported in 2008 proving that the mixing phenomenon could also occur onboard FLNG vessels or FSRU. In this final part, a rollover is simulated onboard a FLNG tank. This, first, aims at illustrating the risk of rollover occurrences

onboard FLNG carriers and, secondly, to emphasise the potential of CFD-based LNG rollover predictive tools to deal with more complex geometries.

5.3.5.1 Input data

The numerical method, developed in this thesis, is employed to simulate a rollover in a 9-meter diameter Moss type reservoir on a sea at rest. The LNG initially present is composed of two stable strata with the same properties and same height as described in Table 5.8.

5.3.5.2 Results

Similarly to the two LNG rollovers previously presented in this section, the rollover phenomenon can be decomposed into the same two stages, i.e. a first stage during which the interface is stationary and a second stage when the interface migrates. At first, during the incubation stage, the density difference between the layers decreases and the temperature of the lower layer increases. The convection cells are also intensifying in the upper layer due to a growing boil-off rate.

Then, during the migration stage, as depicted in Figure 5.29 with the velocity vectors, the convection cells in the upper layer are still intensifying. In the meantime, the density difference between the layers decreases and the temperature of the liquid below the free surface increases causing the interface to sink and the boil-off rate to rise significantly.

In this simulation, the FLNG carrier is not moving. However, Zellouf and Portanier [83] have investigated the effects of sloshing on the stratification and have qualitatively highlighted that the fluid dynamics caused by the sea motion dominates the effects due to buoyancy. Two consequences are likely: either the sea motion breaks the interface between the layers straightaway which limits the superheating of the lower layer, or by promoting the mixing between the layers, the rollover occurrence is accelerated and the peak of boil-off rate reduced.

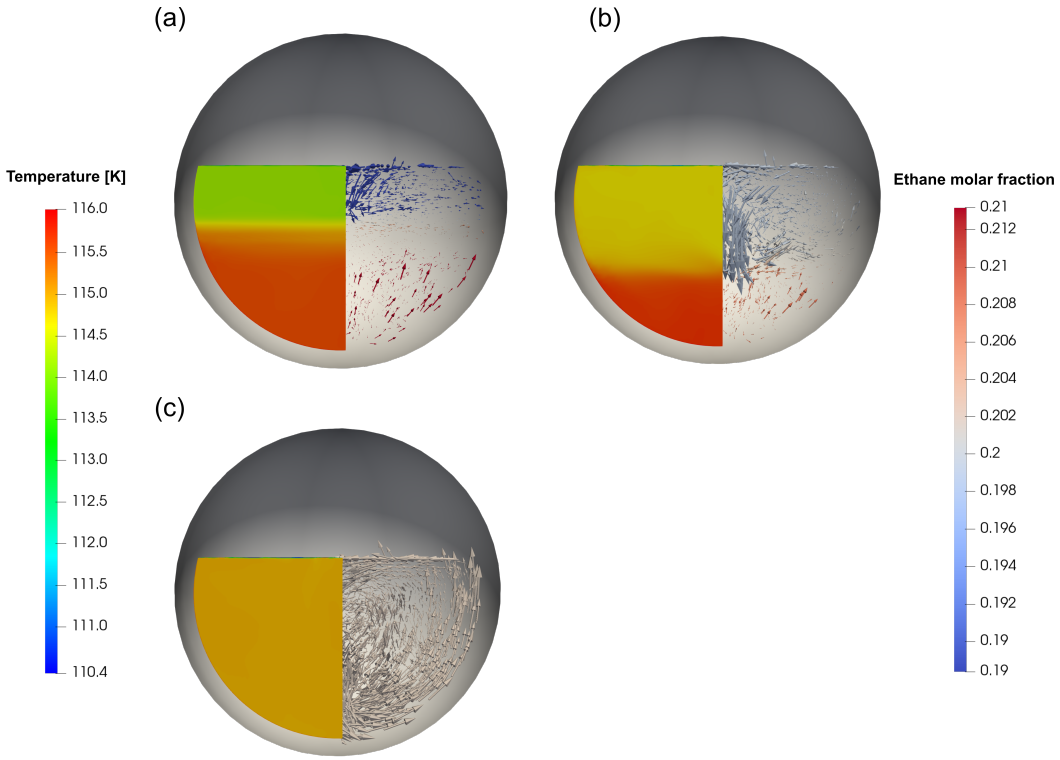

Figure 5.29: 3D representation (a-b-c) of a simulated fictive rollover within a Moss type FLNG tank. The tank is cut in half showing the temperature (on the left-hand side) and simultaneously the velocity fields and ethane molar fraction (on the right-hand side).

CFD simulations applied to motionless reservoir could then help to predict the maximum boil-off rates which is particularly useful when sizing the safety valves.

5.3.6 Conclusion

In this section, the numerical approach developed in this thesis has been applied to a medium-scale experiment conducted in Nantes [82] and to La Spezia incident [6]. In both cases, the results were satisfactory showing good agreements with the experimental and incidental data.

Besides, the results obtained with rolloverFoam, which are, to the author knowledge, the first applications of CFD to actual LNG rollover incidents and experiments, have provided some insights into the rollover phenomenon. First, the results have confirmed that it is composed of two stages [84]: the incubation during which the interface is stationary and the migration stage when the interface migrates downwards. In addition, the results have highlighted that, similarly to Shi et al.'s findings with a mixture of liquid oxygen and nitrogen [39], the migration of the interface was the consequence of the combination of the growing convection cells in the upper layer and the decreasing density difference across the interface. Moreover, unlike the results obtained for mixture of Freon in Section 5.2, the penetration of a thin layer from the lower layer into the upper layer was not observed in the simulations of Nantes experiment and La Spezia incident. However, more research would then be needed to determine if such a phenomenon can occur in a stratified LNG.

In addition, in both cases, the boil-off rate rose drastically during the descent of the interface as a consequence of the mixing of the upper layer with the warmer lower layer. Although, the superheating of the lower layer could be observed during Nantes experiment, according to the numerical results, no extra superheating has occurred during La Spezia incident and prior to the mixing. Indeed, the temperature of the lower layer has remained constant all along the incident. The

observed rise in boil-off rate was only caused by the initially warmer lower layer. The results of the simulation of La Spezia incident highlights that bottom loading a tank with a denser but initially warmer LNG may be hazardous given that it initially contains extra energy compared to the LNG already in the tank. The author recommends to load LNGs with similar temperature in order to prevent any hazardous (very) high boil-off rates in the case a rollover would occur.

The analysis of the results emphasised that the sudden mixing occurs with the migration of the interface as well as the rise of the boil-off rate. If experimentally, it may not be convenient to monitor the position of the interface, any significant change in the composition of the smaller layer — as the effects of the heat and mass being transfered through the interface are less diluted in the smaller volume — may be the sign of the start of the hazardous mixing. At that moment, it would be too late to use mixing devices which would only bring forward the occurrence of the rollover without reducing the boil-off rates, a mitigation solution might be to rapidly pump out the warmer layer. This would fastened the mixing but would limit the amount of energy released by the lower layer under the form of vapours and consequently the overpressure. Besides, the numerical results have demonstrated that a stratified liquid with a density difference inferior to 0.5% could lead to rollover. This highlights the need of accurate monitoring devices within LNG tanks.

Finally, the code rolloverFoam was applied to a Moss type tank illustrating the potential risks of rollover occurrences onboard FSRU — as well as demonstrating the potential of the method to study rollovers in more complex geometries.

5.4 Summary

In this chapter, the code rolloverFoam was first applied to two numerical cases from the literature (Shi [14] and Munakata et al. [15]) and the results were in agreement with those presented in their studies. Besides, it highlighted that the

two mechanisms presented in each of these studies could occur which corroborates the experimental observations of several researchers although seemingly different [39, 38, 15].

The code was then applied to small-scale experiments with binary mixtures of Freon [8] where it highlighted that both mechanisms were driving the mixing during rollover. Indeed, following the incubation stage, the migration starts moving downwards and when the density difference becomes close to nil, then a thin layer from the lower layer penetrates inside the top layer, accelerating the mixing. The influence of several key parameters has also been studied.

In the last section of this chapter, the code, rolloverFoam, was extended to include multicomponent mixtures and in particular LNG. rolloverFoam was then applied to model an LNG rollover experiment conducted in Nantes [41] and has shown good agreement with the experimental data. Finally, the code was also used to simulate La Spezia incident and a fictive rollover onboard a FLNG carrier. In these three cases, the mechanisms driving the mixing during rollover was the downward motion of the interface and no penetration of a thin layer of liquid from the lower layer into the top layer was observed. In any case, in light of these results, the mixing occurring during rollover is far from being the phenomenon of two layers "rolling over" each other as it was initially thought in the 60^s.

Chapter 6

Conclusion and Recommendations

6.1 Conclusion

Within the frame of this thesis, a CFD code, rolloverFoam, has been developed to model the rollover phenomenon. The main novelties of this method, based on previous works conducted by Shi [14], Munakata et al. [15], Lemembre [16] and Seveleder [17], are to include turbulence modelling, to be adapted to complex multicomponent liquids, especially LNG, and to provide 2D and 3D visualisations of the rollover phenomenon. Unlike earlier CFD models, the adopted method has shown satisfactory quantitative results when comparing with experimental data such as small-scale experimental data with mixtures of Freon, medium scale experimental data with LNG as well as data obtained during La Spezia incident. The method has also been employed to simulate a rollover within a FLNG tank.

Besides, the results have given some insights into the rollover phenomenon. For both mixtures of Freon or LNG, the rollover is composed of two stages, the incubation stage and the migration stage. The first stage is characterised by the stationary interface. During this stage, the heat and mass transfers through the interface promote the decrease in density difference between the layers as well

as the superheating of the lower layer in some cases. The second stage occurs once the initial density difference has been reduced and the entrainment rate of the upper layer has increased causing the interface to start moving downwards. During the interface migration, the heat and mass transfers through the interface are intensified, promoting the rise of the boil-off rate while decreasing the density difference. As a consequence, the migration is speeded up until the interface reaches the tank bottom.

However, another phenomenon has been observed with mixtures of Freon in Chapter 5.2. Indeed, the latter is the penetration near the wall of a thin layer of fluid from the lower layer into the upper layer. It is due to the fact that the warmest parcel of liquid in the lower layer is usually located near the wall below the interface. This parcel of fluid may become locally less dense than the parcel of liquid on the other side of the interface and as a result, when the density difference becomes close to nil, the penetration occurs. This phenomenon can be combined to the interface migration especially that during the descent, in small-scale experiments, the temperature of the lower layer increases due to a low thermal inertia. The risks of penetration are then increased. The effects of the penetration phenomenon is the increased heat and mass transfers between the layers therefore accelerating the rollover occurrence. Although this phenomenon was observed in several mixtures such as salt water [37], mixture of ethanol and water [38] or mixture of Freon [8], it is currently not known if it can occur in LNG.

In light of all the simulations conducted within the frame of this thesis, it turns out that the rollover phenomenon is not due to the motion of two layers "rolling over" each other but to the downward motion of the interface and the upper layer pushing on the lower layer. The term "push-down" would then be more suitable to define this phenomenon.

Finally, the method developed in this thesis could help to take decisions prior to LNG loading so as to cut LNG releases down by promoting stratification

while preventing rollovers [13]. Simulations of rollovers within LNG tanks with the developed approach requires high computational power compared to traditional lumped-parameter models but could be highly speeded up (while losing in accuracy) by modelling rollovers in 2D so as to get the order of magnitude of the rollover time for example. As a matter of fact, it would also be interesting, from a practical point of view, to quantify the numerical error of using 2D models instead of 3D ones as far as rollover times and peak of boil-off rates are concerned. Besides, the main difficulty the author has encountered is the lack of publicly available data particularly for LNG. More data issued either from experiments or actual incidents are then needed to validate and improve the accuracy of the developed approach as well as future models. However, in order to be exploitable, this data needs to be more comprehensive and well detailed, especially as far as the positions of the probes are concerned. It would also be interesting to monitor the temperature at the free surface and in the vapour space. Last but not least, this method, although applied to Freon and LNG in this thesis, could also be applied to different contexts such as the assesment of potential risks of rollover in volcanic crater lakes [85].

6.2 Recommendations for future works

The results obtained with rolloverFoam have shown acceptable agreements with benchmark data. However, several implementations could be integrated to improve the current model as well as to extend its use to moving FLNG tanks:

- The numerical models presented in this thesis should be combined with the simulation of the filling procedure as the one done by Koyama [28] to obtain a more realistic initialisation of the concentrations and temperatures but also of the velocity and pressure fields.

- The turbulence modelling can be improved by using Reynolds stress equa-

tion models adapted to the study of buoyant and stratified flows. The use of the Generalised Gradient Diffusion Hypothesis [66] instead of the SGDH would consider the flow anisotropy and provide more accurate results. Besides, LES and DNS models could also be used but require high computational power.

- The presented approach could also be improved by integrating Marangoni and Soret effets, which would improve, respectively, the flow dynamics near the free surface and the diffusion of concentration due to temperature gradients especially on both sides of the interface located between the layers. However, these improvements require additional experimental research to quantify these effects in LNG.

- The evaporation model used in this thesis is based on the Hashemi-Wesson relation. This model, although accurate and validated, links the bulk temperature to the saturation temperature but does not reflect that the local evaporation is driven by a thin layer below the free surface. The aim would be to obtain a more accurate boundary condition for the evaporation so as to reflect that at the free surface near the wall where the temperature is higher, the evaporation is more significant. Having a discretised boundary condition would considerably improve the results accuracy especially when dealing with rollover within moving FLNG tanks.

- The author recommends for future works to couple the current numerical method with a Volume Of Fluid (VOF) approach [86] in order to model both the liquid phase and the vapour phase similarily to the recent work done by Sha et al. [87, 88] with salt water. The interest is that, once implemented, it can relatively easily take into account the reduction of LNG due to evaporation as well as the consequent densification of the LNG near the interface. It could be also particularily useful when studying tanks onboard moving FLNG vessels and sea in motion. Besides, by combining a VOF

approach and modelling locally the evaporation, it would be possible to simulate the effect of the vapour pressure on the liquid. This is particularly of interest during the sudden release of vapour which increases the vapour pressure and reduces momentarily the boil-off releases. Similarly following the opening of the valves, when vapours are released into the atmosphere and consequently the vapour pressure within the tank is decreased, the evaporation is also promoted.

References

[1] International Energy Agency. World Energy Outlook 2016. Technical report, 2016.

[2] International Energy Agency. World Energy Outlook 2017. Technical report, 2017.

[3] GIIGNL Technical Study Group. Rollover in LNG Storage Tanks. Technical report, 2015.

[4] A Acton and R C Van Meerbeke. Rollover in LNG Storage. *Proc.LNG8*, 1986.

[5] Kulitsa Maksym and Wood David A. Floating storage and regasification units face specific LNG rollover challenges: Consideration of saturated vapor pressure provides insight and mitigation options. *Natural Gas Industry B*, 5(4):391–414, 2018.

[6] J A Sarsten. LNG stratification and rollover. *Pipeline Gas J*, 199(9):37, 1972.

[7] J S Turner. The coupled turbulent transports of salt and and heat across a sharp density interface. *International Journal of Heat and Mass Transfer*, 8(5):759–767, 1965.

[8] R Nakano, Y Sugawara, S Yamagata, and J Nakamura. An experimental study on the mixing of stratified layers using liquid freon. In *Gastech 82 LNG-LPG conference*, pages 383–391, 1982.

[9] N Chatterjee and J M Geist. Effects of stratification on boil-off rates in LNG tanks. *Pipeline and Gas Journal*, 199(11), 1972.

[10] A E Germeles. A model for LNG tank rollover. In *Advances in Cryogenic Engineering*, pages 326–336. Springer, 1975.

[11] Janet Heestand, C. W. Shipman, and J. W. Meader. A predictive model for rollover in stratified LNG tanks. *AIChE Journal*, 29(2):199–207, 1983.

[12] GIIGNL Technical Study Group. LNG Custody Transfer Handbook. Technical report, 2017.

[13] YanJun Wang and Harry West. LNG Rollover: Converting a Safety Problem to Tank Loading Operational Asset. In *AIChE Spring National Meeting, Conference Proceedings, Orlando, FL, United States*, 2006.

[14] Ji Quan Shi. *Numerical modelling and experimental study of rollover in cryogenic liquids and liquid freon.* PhD thesis, 1990.

[15] Tetsuo Munakata, Noam Lior, and Ichlro Tanasawa. A study of doubled-iffusive rollover in cylindrical enclosures. *Proceedings of the ASME Heat Transfer Division, Vol. HTD*, 317:279–291, 1995.

[16] Alain Lemembre. *Evolution par convection naturelle d'une stratification formée de deux couches liquides dans un réservoir cylindrique*. PhD thesis, 1999.

[17] Véronique Seveleder. *Convection naturelle doublement diffusive dans des fluides stratifiés: application au gaz naturel liquéfié, GNL*. PhD thesis, 1990.

[18] Nigel Baker and Malcolm Creed. Stratification and rollover in liquefied natural gas storage tanks. *Process safety and environmental protection*, 74(1):25–30, 1996.

[19] International Gas Union. 2017 World LNG Report. Technical report, 2017.

[20] GIIGNL. The LNG industry - GIIGNL Annual Report 2017. Technical report, 2017.

[21] Ralph G Scurlock. *Stratification, Rollover and Handling of LNG, LPG and Other Cryogenic Liquid Mixtures*. Springer, 2015.

[22] Antoine Hubert, Siaka Dembele, Petr Denissenko, and Jennifer Wen. Predicting Liquefied Natural Gas (LNG) rollovers using Computational Fluid Dynamics. *Journal of Loss Prevention in the Process Industries*, (Manuscript submitted for publication), 2019.

[23] N Chatterjee and J M Geist. Spontaneous stratification in LNG tanks containing nitrogen. In *MECHANICAL ENGINEERING*, volume 99, pages 106–107. ASME-AMER SOC MECHANICAL ENG 345 E 47TH ST, NEW YORK, NY 10017, 1977.

[24] GIIGNL Technical Study Group. Rollover in LNG Storage Tanks. Technical report, 2013.

[25] U.S. Energy Information Administration. Henry Hub Natural Gas Spot Price (Dollars per Million Btu).

[26] ISO. ISO 6976:2016 : Natural gas - Calculation of calorific values, density, relative density and Wobbe indices from composition Gaz naturel, 2016.

[27] Society of International Gas Tanker & Terminal Operators SIGTTO. Guidance for the Prevention of Rollover in LNG Ships. Technical report, 2012.

[28] Kazuo Koyama. CFD simulation on LNG storage tank to improve safety and reduce cost. *International Gas Union Research Conference . Paris : International Gas Union*, pages 39–43, 2008.

[29] J S Turner. *Buoyancy Effects in Fluids*. Cambridge University Press, Cambridge, 1973.

[30] Herbert E Huppert and J Stewart Turner. Double-diffusive convection. *Journal of Fluid Mechanics*, 106:299–329, 1981.

[31] J S Turner. Double-Diffusive Phenomena. *Annual Review of Fluid Mechanics*, 6(1):37–54, 1974.

[32] J S Turner. Multicomponent convection. *Annual Review of Fluid Mechanics*, 17(1):11–44, 1985.

[33] H T Hashemi and H R Wesson. Cut LNG storage costs. *Hydrocarbon Processing*, 50:117–120, 1971.

[34] H Doyer, M Gabillard, A Le Cloirec, and D Uznanski. Toward an optimized management of the operating pressure in LNG storage tanks. In *International gas research conference*, volume 2, pages 744–758. GOVERNMENT INSTTUTES INC, 1998.

[35] G T Clegg and G Papadakis. Rates of evaporation accompanying the depressurization of a pool of saturated Freon-11. *Chemical engineering science*, 41(12):3037–3043, 1986.

[36] Tom Agbabi. *Rollover and interfacial studies in LNG mixtures*. PhD thesis, 1987.

[37] M Morioka and S Enya. Natural Convection of Density-Stratified Layers in a Vessel. *Heat Transfer Japanese Research*, 12:48–69, 1984.

[38] T Arita. Fundamental study on rollover of two-density-stratified layers of liquids. *ASME HTD, 1992*, 198:67–72, 1992.

[39] J Q Shi, C Beduz, and R G Scurlock. Numerical modelling and flow visualization of mixing of stratified layers and rollover in LNG. *Institute of Cryogenics, Southampton*, 33(12):1116–1124, 1993.

[40] Y Sugawara, A Kubota, and S Muraki. Rollover test in LNG storage tank and simulation model. In *Advances in Cryogenic Engineering*, volume 29, pages 805–811, 1984.

[41] Gaz de France, Shell Research Ltd, Osaka Gas, Tokyo gas, and CFP-Total. Experimental study of stratified LNG performed at Nantes Cryogenic Testing Station, 1987 to1990. Technical report.

[42] T L Bergman, F P Incropera, and R Viskanta. A differential model for salt-stratified, double- diffusive systems heated from below. *International Journal of Heat and Mass Transfer*, 28(4):779–788, 1985.

[43] M Kazmierczak and D Poulikakos. Transient double diffusion in a stably stratified fluid layer heated from below. *International Journal of Heat and Fluid Flow*, 11(1):30–39, 1990.

[44] P F Crapper. Measurements across a diffusive interface. *Deep-Sea Research*, 22:537–545, 1975.

[45] H Kato and O M Phillips. On the penetration of a turbulent layer into stratified fluid. *Journal of Fluid Mechanics*, 37:643–655, 1969.

[46] S M Thompson and J S Turner. Mixing across an interface due to turbulence generated by an oscillating grid. *Journal of Fluid Mechanics*, 67(2):349–368, 1975.

[47] S Bates and D S Morrison. Modelling the behaviour of stratified liquid natural gas in storage tanks: a study of the rollover phenomenon. *International Journal of Heat and Mass Transfer*, 40(8):1875–1884, 1997.

[48] G J Boyle. Basic Data and Conversion Calculations for Use in the Measurement of Refrigerated Hydrocarbon Liquids. *J Inst Pet*, 58:133–137, 1972.

[49] Samuel Globe and D Dropkin. Natural-convection heat transfer in liquids confined by two horizontal plates and heated from below. *Trans.ASME*, 81:24–28, 1959.

[50] Williams H McAdams. *Heat Transmission*. 1954.

[51] M W Lukaszewski, W B J Zimmerman, M T Tennant, and M B Webster. Application of inverse methods based algorithms to Liquefied Natural Gas (LNG) storage management. *Chemical Engineering Research and Design*, 91(3):457–463, 2013.

[52] Kiran B. Deshpande, William B. Zimmerman, Malcolm T. Tennant, Marcus B. Webster, and Michal W. Lukaszewski. Optimization methods for the real-time inverse problem posed by modelling of liquefied natural gas storage. *Chemical Engineering Journal*, 170(1):44–52, 2011.

[53] Joseph Boussinesq. *Essai sur la théorie des eaux courantes*. Impr. nationale, 1877.

[54] R Byron Bird. Transport phenomena. *Applied Mechanics Reviews*, 55(1):R1—-R4, 2002.

[55] C R Wilke and Pin Chang. Correlation of diffusion coefficients in dilute solutions. *AIChE Journal*, 1(2):264–270, 1955.

[56] D. T.J. Hurle and E. Jakeman. Soret-driven thermosolutal convection. *Journal of Fluid Mechanics*, 47(4):667–687, 1971.

[57] A Bejan and J L Lage. The Prandtl number effect on the transition in natural convection along a vertical surface. *Journal of heat transfer*, 112(3):787–790, 1990.

[58] Henk Kaarle Versteeg and Weeratunge Malalasekera. *An introduction to computational fluid dynamics: the finite volume method*. Pearson Education, 2007.

[59] Hermann Schlichting and Klaus Gersten. *Boundary-layer theory*. Springer, 2016.

[60] W P Jones and B E Launder. The prediction of laminarization with a two-equation model of turbulence. *International Journal of Heat and Mass Transfer*, 15(2):301–314, 1972.

[61] RAWM Henkes, F F Van Der Vlugt, and C J Hoogendoorn. Natural-convection flow in a square cavity calculated with low-Reynolds-number turbulence models. *International Journal of Heat and Mass Transfer*, 34(2):377–388, 1991.

[62] Wolfgang Rodi. *Turbulence models and their application in hydraulics - A state-of-the-art review*. Routledge, 1984.

[63] Brian Edward B.E. Launder and B.I. I Sharma. Application of the energy-dissipation model of turbulence to the calculation of flow near a spinning disc. *Letters in heat and mass transfer*, 1(2):131–137, nov 1974.

[64] P.L. Viollet. The modelling of turbulent recirculating flows for the purpose of reactor thermal-hydraulic analysis. *Nuclear Engineering and Design*, 99:365–377, feb 1987.

[65] J J McGuirk and C Papadimitriou. Buoyant surface layers under fully entraining and internal hydraulic jump conditions. In *Proceedings of the Fifth Symposium on Turbulent Shear Flows*, 1985.

[66] B. E. Launder. RANS modelling of turbulent flows affected by buoyancy or stratification. In Geoff Hewitt and Christos Vassilicos, editors, *Prediction of Turbulent Flows*, pages 50–127. Cambridge University Press, Cambridge, 2005.

[67] Bart J Daly and Francis H Harlow. Transport equations in turbulence. *The Physics of Fluids*, 13(11):2634–2649, 1970.

[68] M S Khelifi-Touhami, A Benbrik, D Lemonnier, and D Blay. Laminar natural convection flow in a cylindrical cavity application to the storage of LNG. *Journal of Petroleum Science and Engineering*, 71(3):126–132, 2010.

[69] Đ Dobrota, B Lalić, I Komar Transactions on maritime Science, and Undefined 2013. Problem of boil-off in LNG supply chain. *Transactions on maritime science*, (2(02)):91–100, 2013.

[70] Joel H Ferziger and Milovan Peric. *Computational methods for fluid dynamics*. Springer Science & Business Media, 2012.

[71] Henry G Weller, G Tabor, Hrvoje Jasak, and C Fureby. A tensorial approach to computational continuum mechanics using object-oriented techniques. *Computers in physics*, 12(6):620–631, 1998.

[72] C M Rhie and W Li Chow. Numerical study of the turbulent flow past an airfoil with trailing edge separation. *AIAA journal*, 21(11):1525–1532, 1983.

[73] Hrvoje Jasak. Error analysis and estimation for finite volume method with applications to fluid flow. 1996.

[74] R F Warming and Richard M Beam. Upwind Second-Order Difference Schemes and Applications in Aerodynamic Flows. *AIAA Journal*, 14(9):1241–1249, sep 1976.

[75] Magnus Rudolph Hestenes and Eduard Stiefel. *Methods of conjugate gradients for solving linear systems*, volume 49. NBS Washington, DC, 1952.

[76] Henk A Van der Vorst. Bi-CGSTAB: A fast and smoothly converging variant of Bi-CG for the solution of nonsymmetric linear systems. *SIAM Journal on scientific and Statistical Computing*, 13(2):631–644, 1992.

[77] David A H Jacobs. A generalization of the conjugate-gradient method to solve complex systems. *IMA journal of numerical analysis*, 6(4):447–452, 1986.

[78] Suhas V Patankar and D Brian Spalding. A calculation procedure for heat, mass and momentum transfer in three-dimensional parabolic flows. In *Numerical Prediction of Flow, Heat Transfer, Turbulence and Combustion*, pages 54–73. Elsevier, 1983.

[79] Raad I. Issa. Solution of the implicitly discretised fluid flow equations by operator-splitting. *Journal of computational physics*, 62(1):40–65, 1986.

[80] Paulo J. Oliveira and Raad I. Issa. An improved PISO algorithm for the computation of buoyancy-driven flows. *Numerical Heat Transfer: Part B: Fundamentals*, 40(6):473–493, 2001.

[81] J Klosek and C McKinley. Densities of liquefied natural gas and of low molecular weight hydrocarbons. In *First International Conference on LNG. Chicago*, 1968.

[82] Peter J Linstrom and W G Mallard. NIST Chemistry webbook; NIST standard reference database No. 69. 2001.

[83] O. Gorieu, D. Uznanski, and P. DuPont. How to operate LNG terminals with flexibility/safety despite the diversification of unloaded LNG qualities. *14th International Conference and Exhibition on Liquefied Natural Gas*, pages 1–10, 2004.

[84] Yacine Zellouf and Benoît Portannier. First step in optimizing LNG storages for offshore terminals. In *International Gas Union Research Conference 2011*, page 19. Elsevier, 2011.

[85] A Rice. Rollover in volcanic crater lakes: a possible cause for Lake Nyos type disasters. *Journal of Volcanology and Geothermal Research*, 97(1):233–239, 2000.

[86] C W Hirt and B D Nichols. Volume of fluid (VOF) method for the dynamics of free boundaries. *Journal of Computational Physics*, 39(1):201–225, 1981.

[87] Wei Sha, Jingjie Ren, Cheng Wang, Mingshu Bi, and Yaofen Bo. Dynamic characteristics of the initial interface in stratified multi-composition liquid tanks during rollover. *Applied Thermal Engineering*, 145(September):396–406, 2018.

[88] Wei Sha, Jingjie Ren, Han Zhang, Yaofen Bo, and Mingshu Bi. Analysis of the interfacial instability and the patterns of rollover in multi-component layered system. *International Journal of Heat and Mass Transfer*, 126:235–242, 2018.

[89] ISO. ISO 6578:2017 : Refrigerated hydrocarbon liquids - Static measurement - Calculation procedure, 2017.

List of publications

Hubert, A., Dembele, S., Denissenko, P. and Wen, J. Predicting Liquefied Natural Gas (LNG) rollovers using Computational Fluid Dynamics. *Journal of Loss Prevention in the Process Industries*. Manuscript submitted for publication in March 2019.

Hubert, A., Dembele, S., Denissenko, P. and Wen, J. (2018). Numerical predictions of rollovers in LNG storage tanks using CFD. 72$^{\text{nd}}$ FABIG Newsletter.

Hubert, A., Dadonau, M., Dembele, S., Denissenko, P. and Wen, J. (2017). Comparison of the key mechanisms leading to rollovers in Liquefied Natural Gas using Computational Fluid Dynamics. 70th Annual Meeting of the American Physical Society Division of Fluid Dynamics, Denver, Colorado, US.

Hubert, A., Dembele S. and Wen, J. (2017). Predicting LNG Rollover. FABIG 92$^{\text{th}}$ Technical meeting, Aberdeen-London.

Hubert, A., Dembele, S., Denissenko, P. and Wen, J. (2017). Numerical predictions of the rollover phenomenon using Computational Fluid Dynamics. Hazards27 Conference, Birmingham, UK. IchemE.

Appendix A

Concentration

A.1 Conversions

The mass fraction ω_i defined such as $\omega_i = \frac{C_i}{\rho}$ can be derived from the molar fraction as follows:

$$\omega_i = x_i \frac{M_i}{M} \tag{A.1}$$

where x_i is the molar fraction, M the average molar mass of the mixture and M_i the average molar mass of the component i.

A.2 Fick's Law

Fick's law can be written with the mass concentration as:

$$\boldsymbol{j_i} = -D_i \nabla C_i \tag{A.2}$$

where D_i is the diffusivity of the component i in a given solvent.

The same relation can be written with the mass fraction ω_i:

$$\boldsymbol{j_i} = -\rho D_i \nabla \omega_i \tag{A.3}$$

A.3 Derivation of the evaporative boundary condition

Following Lemembre [16], the flux of evaporating solvent is assimilated to an equivalent incoming flux of solute. In this section, the expression for the flux of solute is derived.
The mass concentration in solute is as follows:

$$C_{solute} = \frac{m_{solute}}{m_{solute} + m_{solvent}} \rho \tag{A.4}$$

which can also be written as:

$$(m_{solute} + m_{solvent})\, C_{solute} = m_{solvent}\, \rho \tag{A.5}$$

The variations of solvent or solute are small enough to consider a constant density ρ. Equation A.5 can be differenciated for relatively small time variations δ:

$$\delta(m_{solute} + m_{solvent})\, C_{solute} + (m_{solute} + m_{solvent})\, \delta C_{solute} = \delta m_{solute} \rho \tag{A.6}$$

For a constant quantity of solute m_{solute}, Equation A.6 becomes:

$$\delta m_{solvent}\, C_{solute} + (m_{solute} + m_{solvent})\, \delta C_{solute} = 0 \tag{A.7}$$

which is equivalent to:

$$\dot{m}_{solvent}\, C_{solute} + (m_{solute} + m_{solvent}) \dot{C}_{solute} = 0 \tag{A.8}$$

Finally, the variation of concentration with time is such as:

$$\dot{C}_{solute} = -\frac{\dot{m}_{solvent}\, C_{solute}}{m_{solute} + m_{solvent}} \tag{A.9}$$

In the case where $m_{solvent}$ is constant, Equation A.6 becomes:

$$\delta(m_{solute})\, C_{solute} + (m_{solute} + m_{solvent})\, \delta C_{solute} = \delta m_{solute} \rho \tag{A.10}$$

After dividing by δt, it yields to:

$$\dot{m}_{solute}\, C_{solute} + (m_{solute} + m_{solvent})\, \dot{C}_{solute} = \dot{m}_{solute} \rho \tag{A.11}$$

which can finally be written as:

$$\dot{C}_{solute} = \frac{\dot{m}_{solute}(\rho - C_{solute})}{m_{solute} + m_{solvent}} \tag{A.12}$$

As a result, the case where $m_{solvent}$ is constant is equivalent to the case where m_{solute} is constant if and only if:

$$-\frac{\dot{m}_{solvent}\, C_{solute}}{m_{solute} + m_{solvent}} = \frac{\dot{m}_{solute}(\rho - C_{solute})}{m_{solute} + m_{solvent}} \tag{A.13}$$

which can finally be rearranged as:

$$\boxed{\dot{m}_{solute} = -\dot{m}_{solvent}\left(\frac{C_{solute}}{\rho - C_{solute}}\right)} \tag{A.14}$$

The flux of solute being expressed with Fick's law, the gradient of mass concentration in solute is such as:

$$\nabla C_{solute} = \frac{1}{D}\left(\frac{C_{solute}}{C_{solute} - \rho}\right)\dot{m}_{solvent} \tag{A.15}$$

and for the gradient of molar fraction, the gradient is defined as:

$$\nabla \omega_{solute} = \frac{1}{\rho D}\left(\frac{\omega_{solute}}{\omega_{solute} - 1}\right)\dot{m}_{solvent} \tag{A.16}$$

Now, let's consider 2 solutes. After differenciation and when m_{solute_1} and

m_{solute_2} are constant, the two following equation are obtained for $solute_1$ and $solute_2$:

$$\dot{m}_{solvent}\, C_{solute_1} + (m_{solute_1} + m_{solute_2} + m_{solvent})\dot{C}_{solute_1} = 0 \tag{A.17}$$

$$\dot{m}_{solvent}\, C_{solute_2} + (m_{solute_1} + m_{solute_2} + m_{solvent})\dot{C}_{solute_2} = 0 \tag{A.18}$$

in the case where $m_{solvent}$ is constant, the two following equations are obtained:

$$(\dot{m}_{solute_1} + \dot{m}_{solute_2})\, C_{solute_1} + (m_{solute_1} + m_{solute_2} + m_{solvent})\, \dot{C}_{solute_1} = \dot{m}_{solute_1}\rho \tag{A.19}$$

$$(\dot{m}_{solute_1} + \dot{m}_{solute_2})\, C_{solute_2} + (m_{solute_1} + m_{solute_2} + m_{solvent})\, \dot{C}_{solute_2} = \dot{m}_{solute_2}\rho \tag{A.20}$$

Substracting Equations A.17 and A.18 to respectively Equations A.19 and A.20 leads to the two following equations when the cases where m_{solute_1} and m_{solute_2} being constant are equivalent to $m_{solvent}$ being constant:

$$(\dot{m}_{solute_1} + \dot{m}_{solute_2} + \dot{m}_{solvent})\, C_{solute_1} = \dot{m}_{solute_1}\rho \tag{A.21}$$

$$(\dot{m}_{solute_1} + \dot{m}_{solute_2} + \dot{m}_{solvent})\, C_{solute_2} = \dot{m}_{solute_2}\rho \tag{A.22}$$

which is equivalent to:

$$\frac{C_{solute_1}}{C_{solute_2}} = \frac{\dot{m}_{solute_1}}{\dot{m}_{solute_2}} \tag{A.23}$$

Finally, injecting Equation A.23 into Equations A.21 and A.22 gives:

$$\boxed{\dot{m}_{solute_1} = -\dot{m}_{solvent}\left(\frac{C_{solute_1}}{\rho - (C_{solute_1} + C_{solute_2})}\right)} \tag{A.24}$$

$$\boxed{\dot{m}_{solute_2} = -\dot{m}_{solvent}\left(\frac{C_{solute_2}}{\rho - (C_{solute_1} + C_{solute_2})}\right)} \tag{A.25}$$

Similarly, the previous relation can be generalised to n solutes:

$$\boxed{\dot{m}_{solute_i} = -\dot{m}_{solvent}\left(\frac{C_{solute_i}}{\rho - \sum_k C_{solute_k}}\right)} \tag{A.26}$$

Appendix B

Additional visualisations

In this appendix, additional visualisations of the rollovers simulated by Shi [14] and Munakata et al. [15] are provided.

In Tables B.1 and B.2 are respectively depicted the fields for concentration, temperature and velocity magnitude obtained after simulating the same case as Shi with $Ra^* = 1.0 \times 10^7$ and $Ra_C = 9.25 \times 10^7$ and Munakata et al.'s case with $Ra^* = 2.46 \times 10^9$ and $Ra_C = 4.42 \times 10^9$.

The fields presented are dimensionless and follow the same conventions as the one used by these authors. For Shi, the dimensionless concentration $\tilde{C}$, temperature $\tilde{T}$ and velocity $\tilde{u}$ are defined as:

$$\tilde{C} = \frac{C}{\Delta C} \tag{B.1}$$

where ΔC is the initial concentration difference between the layers,

$$\tilde{T} = \frac{T}{H^2/\alpha} \tag{B.2}$$

and

$$\tilde{u} = \frac{u}{\alpha/H} \tag{B.3}$$

where α and H stand respectively for the thermal diffusivity and the liquid height.

As for Munakata et al., the dimensionless concentration $\tilde{C}$, temperature $\tilde{T}$ and velocity $\tilde{u}$ are defined as:

$$\tilde{C} = \frac{C - C_l}{\Delta C} \tag{B.4}$$

where ΔC is the initial concentration difference between the layers and C_l the initial concentration in the lower layer.

$$\tilde{T} = \frac{T}{qH/\lambda} \tag{B.5}$$

with q the heat flux through the side wall, H the liquid height and λ its thermal conductivity.

$$\tilde{u} = \frac{u}{\nu/H} \tag{B.6}$$

with ν the liquid kinematic viscosity.

As far as the dimensionless time, Shi defined it as:

$$\tilde{t} = \frac{t}{H^2/\alpha} \tag{B.7}$$

As for Munakata et al., they defined the dimensionless time as:

$$\tilde{t} = \frac{t}{H^2/\nu} \tag{B.8}$$

Table B.1: Concentration, temperature and velocity fields at different stages of the mixing for Shi's case with $Ra^* = 1.0 \times 10^7$ and $Ra_C = 9.25 \times 10^7$

	Concentration	**Temperature**	**Velocity**
$\tilde{t} = 0$			
$\tilde{t} = 0.08$	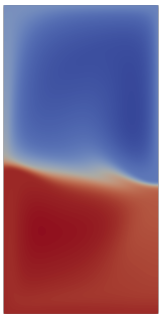	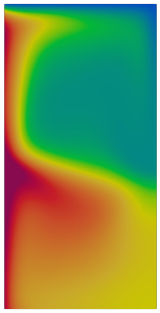	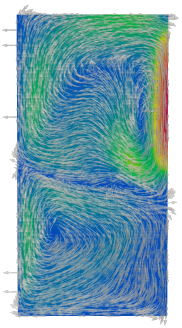
$\tilde{t} = 0.145$	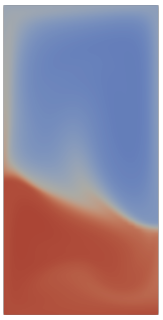	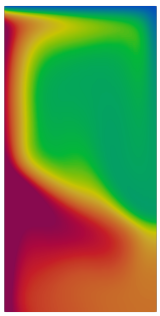	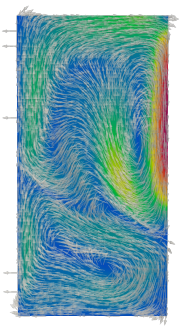
$\tilde{t} = 0.225$		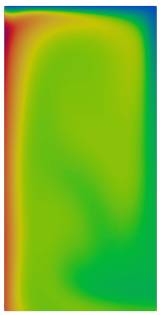	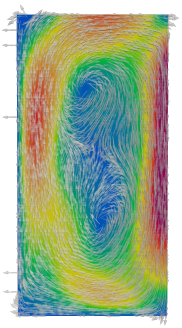
	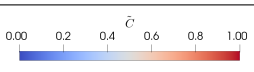	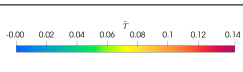	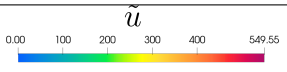

Table B.2: Concentration, temperature and velocity fields at different stages of the mixing for Munakata et al.'s case with $Ra^* = 2.46 \times 10^9$ and $Ra_C = 4.42 \times 10^9$

	Concentration	**Temperature**	**Velocity**
$\tilde{t} = 0.01$		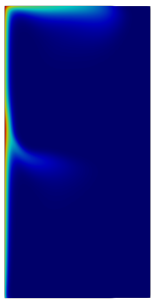	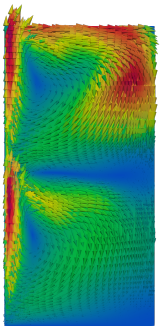
$\tilde{t} = 0.02$		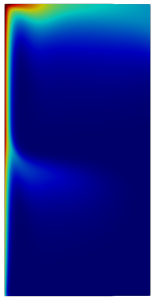	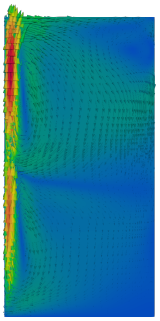
$\tilde{t} = 0.04$	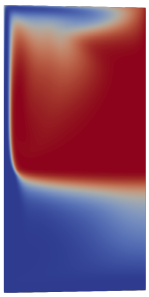	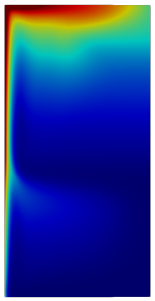	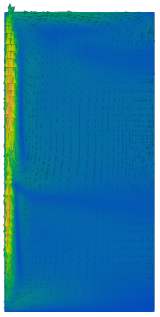
$\tilde{t} = 0.07$	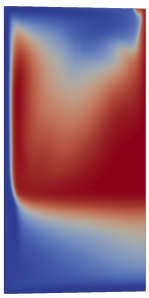	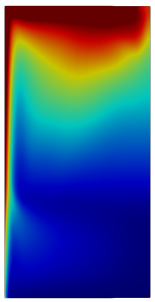	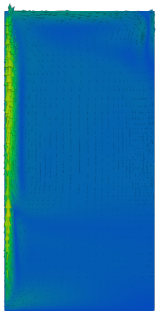
	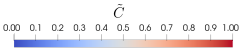	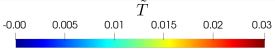	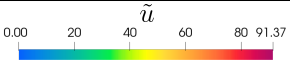

Appendix C

Vapour-Liquid Equilibrium

The mixture Freon 11/Freon 113 is assumed to be ideal and in equilibrium. Raoult's law gives for each component:

$$x_i P_i^{vp}(T) = y_i P \tag{C.1}$$

where x_i and y_i are, respectively, the molar fraction of the liquid and of the vapour of the component i at the temperature T. P_i^{vp} is the vapour pressure of the component i and P the pressure of the vapour phase. P_i^{vp} can be determined using Antoine's equation:

$$\log_{10} P_i^{vp}(T) = A_i - \frac{B_i}{T + C_i} \tag{C.2}$$

where A_i, B_i and C_i are obtained from NIST Chemistry Webbook [81] and as defined in Table C.1. The reported values are applicable for P_i^{vp} in bar and T in Kelvin.

	Freon 11	**Freon 113**
A	4.01447	4.02936
B	1043.303	1112.856
C	-36.602	-44.119

Table C.1: Definition of the parameters in Antoine's Equation

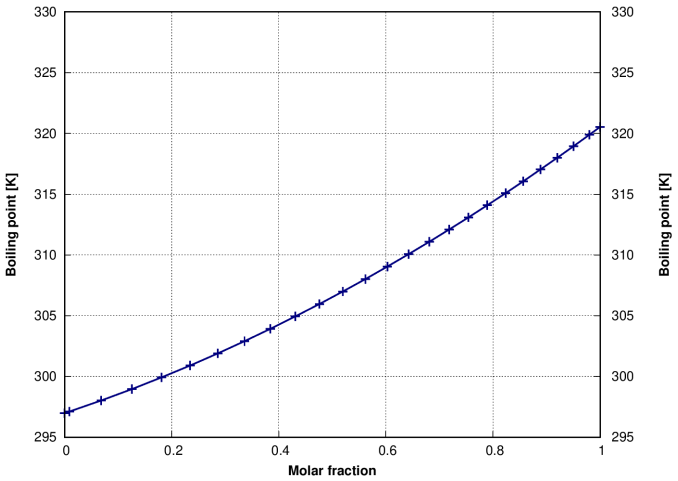

Figure C.1: Variation of saturation temperature with molar fraction

Besides, summing Equation C.1 for Freon 11 and Freon 113 yields to:

$$x_{113}P_{113}^{vp} + (1 - x_{113})P_{11}^{vp}(T) = P \tag{C.3}$$

The subscripts 11 and 113 account for Freon 11 and Freon 113.

Finally, after reiterating the process for different temperatures, the graph presented in Figure C.1 relating the saturation temperature to the molar fraction is obtained.

Appendix D

Assesment of the heat through the walls

The results in Section 5.2.4.2 have highlighted that the heat indicated by Nakano et al. [8] is significantly higher than the heat actually supplied to the liquid in the experiment. It is likely that the power provided in the paper corresponds to the electrical power transferred to the copper plates but, due to a weak insulation, part of the heat is transferred to the ambient air temperature.

In this set-up, the liquid is placed in a rectangular container (height x width x depth : 0.39 m x 0.49 m x 0.2 m) and is heated on the sides and below according to Nakano et al. [8]. The boil-off rate during the first hours of the experiment is around 0.2 kg/h.

Given that the lower the temperature difference is between the layers, the lower the heat transfer through the interface is. As a result, at the beginning of the experiment, the heat transfer through the interface is limited and small compared to the heat ingress through the walls and to the evaporative heat flux.

The following system of heat balance equations are obtained for the upper

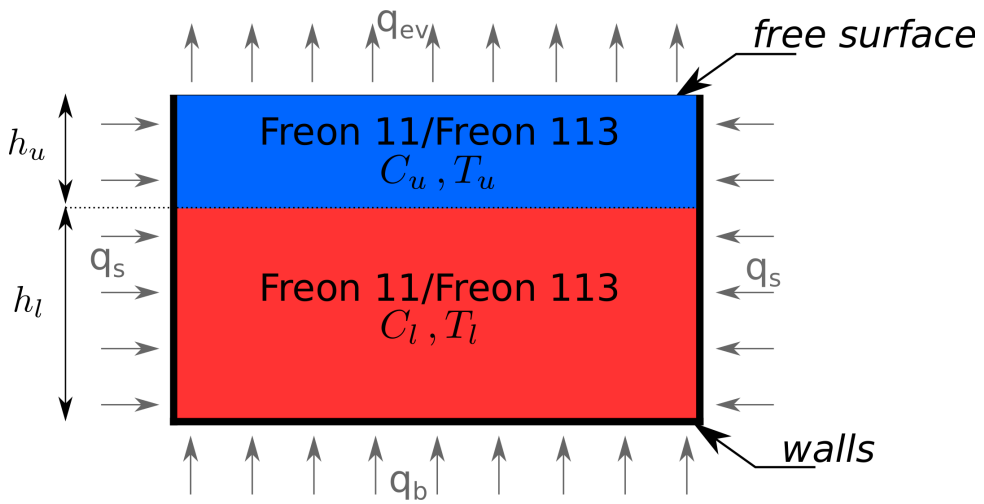

Figure D.1: Simplified model of Nakano et al. experimental set-up

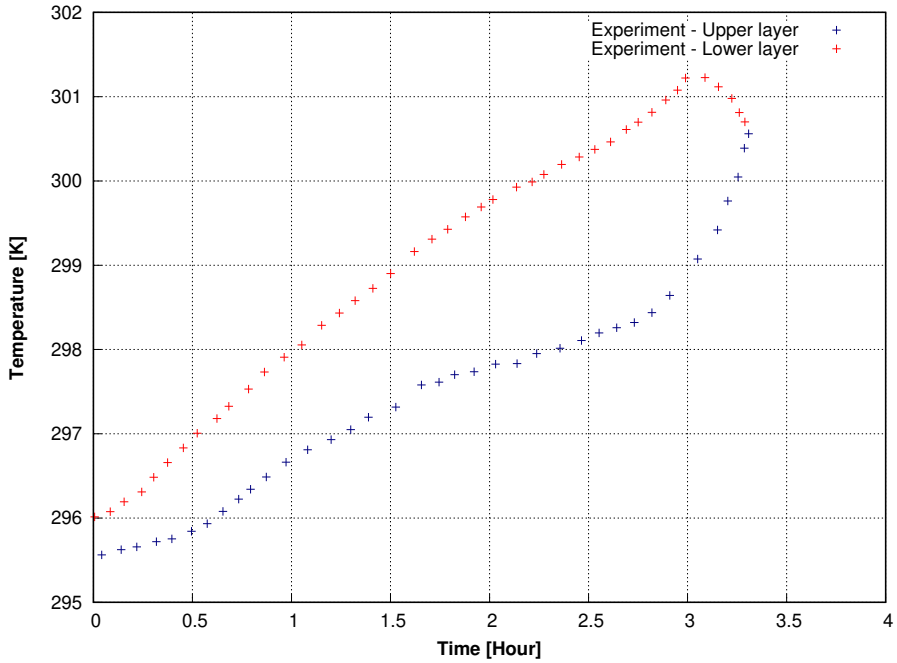

Figure D.2: Temperatures measured during Nakano et al. rollover experiment [8]

and the lower layer:

$$\left.\begin{aligned}\rho_u c_p V_u \tfrac{dT_u}{dt} &= 2q_s h_u wd + q_{ev} dw + q_{lu} dw \\ \rho_l c_p V_l \tfrac{dT_l}{dt} &= 2q_s h_l wd + q_b dw + q_{ul} dw\end{aligned}\right\} \tag{D.1}$$

where d is the depth of the container, w its width, and, q_s, q_b, q_{lu} and q_{ul} are respectively the side heat flux, the bottom heat flux, the heat flux from the lower layer towards the upper layer and the heat flux from the upper layer towards the lower layer.

To obtain a rough estimate of the heat transfer through the walls assumed constant during the experiment and uniform all along the walls, the values of q_s and q_b are interpreted during the first part of the experiment (during the 25 first minutes) when the heat transfer is limited through the interface because of the low temperature difference between the layers. It is assumed during this period that $q_{ul} = q_{lu} = 0$.

Besides, the temperatures measured during Nakano et al. experiment were provided by the authors and are shown in Figure D.2. From this graph, the values of $\frac{dT_u}{dt}$ and $\frac{dT_l}{dt}$ can be calculated. q_{ev}, being defined as $q_{ev} = \dot{m}L$, is known from the boil-off rate. q_s and q_b can then be calculated. P_s, the total heat transmitted through the side walls to the liquid, is found to oscillate between 5.03 and 8.4 W with an averaged value of 6.6 W. As far as P_b the total heat transmitted through the bottom varies during the first 25 minutes of the experiment between 4.5 and 10.2 W with an averaged value of 7.2 W. As a result, P_s and P_b are taken equal to 6.6 W and 7.2 W. This is a rough estimate but it emphasises that approximately one fifth of the heat supplied to the side walls is actually transmitted to the liquid and similarly one third of the heat from the bottom wall is transferred to the liquid.

Appendix E

LNG density calculation

The tables used to calculate the correction factors k_1 and k_2 when using the revised Klosek-McKinley method [89] are provided hereafter.

Notes:

1. The molecular mass of mixture are given in g·mol^{-1}.

2. The exact value of k_1 and k_2 are obtained by linear interpolation, assuming exact linearity between adjacent values in the table.

Molecular mass of mixture	$k_1.10^3$, $m^3 \cdot kmol^{-1}$								
$\Sigma x_i M_i$	**-180°C**	**-175°C**	**-170°C**	**-165°C**	**-160°C**	**-155°C**	**-150°C**	**-145°C**	**-140°C**
16	-0.01	-0.01	-0.01	-0.01	-0.01	-0.01	-0.01	-0.01	-0.01
17	0.13	0.15	0.16	0.18	0.21	0.24	0.28	0.33	0.38
18	0.25	0.29	0.33	0.37	0.41	0.47	0.56	0.66	0.76
19	0.37	0.41	0.45	0.51	0.58	0.67	0.76	0.87	1.01
20	0.47	0.52	0.59	0.67	0.76	0.86	0.98	1.1	1.3
21	0.55	0.62	0.7	0.79	0.89	1	1.13	1.29	1.45
22	0.64	0.72	0.81	0.9	1.01	1.17	1.32	1.52	1.71
23	0.72	0.82	0.92	1.02	1.15	1.33	1.53	1.68	1.84
24	0.81	0.92	1.04	1.16	1.3	1.47	1.66	1.87	2.13
25	0.88	1	1.12	1.25	1.41	1.58	1.78	2	2.27
26	0.95	1.07	1.19	1.33	1.5	1.68	1.89	2.13	2.41
27	1.01	1.13	1.26	1.41	1.58	1.78	1.99	2.24	2.53
28	1.06	1.18	1.32	1.47	1.64	1.84	2.06	2.32	2.62
29	1.11	1.23	1.37	1.54	1.72	1.92	2.15	2.42	2.73
30	1.16	1.29	1.43	1.6	1.79	2	2.24	2.51	2.83

Table E.1: Correction factor k_1

Molecular mass of mixture	$k_2.10^3$, $m^3 \cdot kmol^{-1}$								
$\Sigma x_i M_i$	**-180°C**	**-175°C**	**-170°C**	**-165°C**	**-160°C**	**-155°C**	**-150°C**	**-145°C**	**-140°C**
16	0	-0.01	-0.01	-0.01	-0.02	-0.03	-0.04	-0.05	-0.07
17	0.11	0.15	0.21	0.29	0.46	0.68	0.91	1.21	1.6
18	0.26	0.32	0.39	0.53	0.67	0.84	1.05	1.34	1.8
19	0.4	0.47	0.57	0.71	0.88	1.13	1.39	1.76	2.22
20	0.56	0.62	0.71	0.86	1.06	1.33	1.62	2.03	2.45
21	0.67	0.76	0.87	1.01	1.16	1.48	1.85	2.26	2.79
22	0.78	0.9	1.01	1.16	1.27	1.65	2.09	2.51	3.13
23	0.88	1.03	1.15	1.3	1.42	1.85	2.33	2.81	3.49
24	0.98	1.13	1.27	1.45	1.6	2.06	2.58	3.11	3.74
25	1.07	1.22	1.38	1.61	1.89	2.28	2.73	3.29	3.97
26	1.15	1.31	1.5	1.74	2.04	2.44	2.92	3.48	4.19
27	1.22	1.4	1.61	1.87	2.19	2.6	3.1	3.71	4.46
28	1.31	1.5	1.72	1.99	2.33	2.77	3.31	3.95	4.74
29	1.38	1.59	1.83	2.12	2.48	2.95	3.51	4.19	5.03
30	1.47	1.68	1.93	2.24	2.63	3.12	3.72	4.45	5.34

Table E.2: Correction factor k_2